Systematic Studies of Protein Immobilization by Surface Plasmon Field-Enhanced Fluorescence Spectroscopy

Dissertation zur Erlangung des Grades
“Doktor der Naturwissenschafen”

am Fachbereich Biologie
der Johannes Gutenberg-Universität
in Mainz

vorgelegt von
Jing Liu
aus Chengdu, Sichuan, V. R. China

Mainz, Februar, 2005

Die vorliegende Arbeit wurde unter Betreuung von Herrn Prof. Dr. H. Paulsen und Herrn Prof. Dr. W. Knoll im Zeitraum zwischen August 2001 bis Februar 2005 am Max-Planck-Institute für Polymerforschung, Mainz, Deutschland angefertigt.

Abstract

The research interest of this study is to investigate surface immobilization strategies for proteins and other biomolecules by the surface plasmon field-enhanced fluorescence spectroscopy (SPFS) technique.

The recrystallization features of the S-layer proteins and the possibility of combining the S-layer lattice arrays with other functional molecules make this protein a prime candidate for supramolecular architectures. The recrystallization behavior on gold or on the secondary cell wall polymer (SCWP) was recorded by SPR. The optical thicknesses and surface densities for different protein layers were calculated. In DNA hybridization tests performed in order to discriminate different mismatches, recombinant S-layer-streptavidin fusion protein matrices showed their potential for new microarrays. Moreover, SCWPs coated gold chips, covered with a controlled and oriented assembly of S-layer fusion proteins, represent an even more sensitive fluorescence testing platform. Additionally, S-layer fusion proteins as the matrix for LHCII immobilization strongly demonstrate superiority over routine approaches, proving the possibility of utilizing them as a new strategy for biomolecular coupling.

In the study of the SPFS hCG immunoassay, the biophysical and immunological characteristics of this glycoprotein hormone were presented first. After the investigation of the effect of the biotin thiol dilution on the coupling efficiently, the interfacial binding model including the appropriate binary SAM structure and the versatile streptavidin-biotin interaction was chosen as the basic supramolecular architecture for the fabrication of a SPFS-based immunoassay. Next, the affinity characteristics between different antibodies and hCG were measured via an equilibrium binding analysis, which is the first example for the titration of such a high affinity interaction by SPFS. The results agree very well with the constants derived from the literature. Finally, a sandwich assay and a competitive assay were selected as templates for SPFS-based hCG detection, and an excellent LOD of 0.15 mIU/ml was attained via the "one step" sandwich method. Such high sensitivity not only fulfills clinical requirements, but is also better than most other biosensors.

Fully understanding how LHCII complexes transfer the sunlight energy directionally and efficiently to the reaction center is potentially useful for constructing biomimetic devices as solar cells. After the introduction of the structural and the spectroscopic features of LHCII, different surface immobilization strategies of LHCII were summarized next. Among them the strategy based on the His-tag and the immobilized metal (ion) affinity chromatography (IMAC) technique were of great interest and resulted in different kinds of home-fabricated His-tag chelating chips. Their substantial protein coupling capacity, maintenance of high biological activity and a remarkably repeatable binding ability on the same chip after regeneration was demonstrated. Moreover, different parameters related to the stability of surface coupled reconstituted complexes, including sucrose, detergent, lipid, oligomerization, temperature and circulation rate, were evaluated in order to standardize the most effective immobilization conditions. In addition, partial lipid bilayers obtained from LHCII contained proteo-liposomes fusion on the surface were observed by the QCM technique. Finally, the inter-complex energy transfer between neighboring LHCIIs on a gold protected silver surface by excitation with a blue laser (λ = 473nm) was recorded for the first time, and the factors influencing the energy transfer efficiency were evaluated.

CONTENTS

1 INTRODUCTION

1.1 Biosensor

A sensor can be defined as a device that in response to a physical stimulus produces an output which can be used for measurement, interpretation or control[1]. The sensor is comprised of three essential components: the detector, which recognizes the physical stimulus; the transducer, which converts the stimulus to a useful electronic signal; and the output system itself, which involves amplification, display *etc.* in an appropriate format. The term “biosensor” is now generally applied to those sensor devices which employ a biological or biochemical detection system, or uses biological molecules – usually an enzyme, antibody or nucleic acid – to recognize sample molecules of interest via hydrogen bonding, charge-charge interactions, and other biochemical interactions[2] (cf. Figure 1.1).

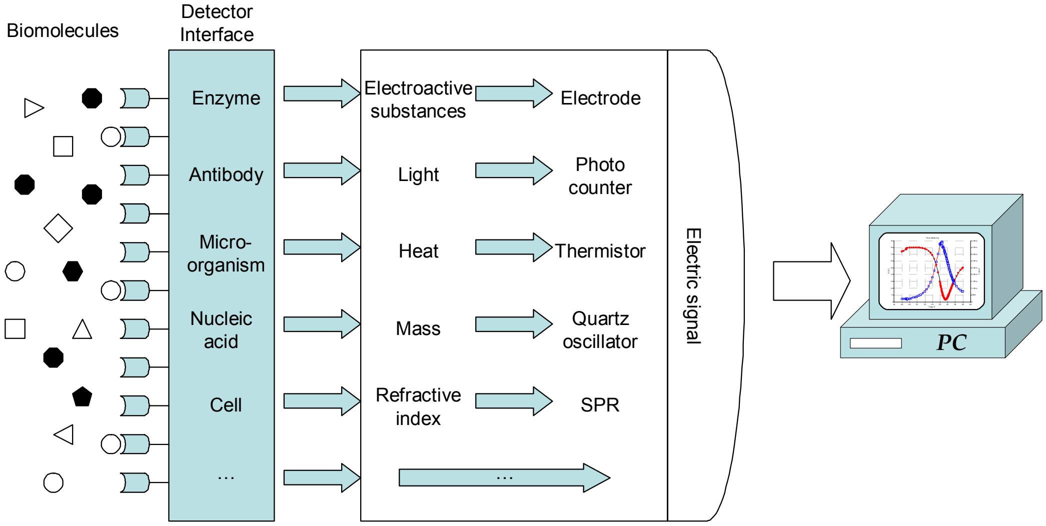

Figure 1.1: Schematic representation of the principle of biosensors.

Biosensors can be classified according to three schemes: (1) the detector type, *e.g.* an immunosensor, (2) the physics of the transduction process, *e.g.* an amperometric sensor, or (3) the application, *e.g.* a medical biosensor. Each scheme is useful in a particular context, though (2) is the most commonly used. Table 1.1 provides compilations of the various biosensors in terms of the transduction mechanisms.

Transduction system	Measurement
Electrochemical	Amperometry (current at fixed voltage)
	Potentiometry (voltage at zero current)
Electrical	Conductivity
Optical	Luminescence
	Fluorescence
	Refractive index
Thermal	Calorimetry
Piezoelectric	Mass - quartz crystal microbalances
	Mass-surface acoustic waves

Table 1.1: Principal transduction systems used in biosensors[3].

The last four decades have witnessed an extraordinary growth in research on biosensors after the pioneering work of Clark and Lyons in 1962[4]. The integration of the features such as high sensitivity, high specificity, miniaturization, low cost and essentially real-time measurements for biosensors in a variety of applications has generated intense commercial interest and potentially growing markets.

The genomic era of biomedical research in the 1990s provided massive amounts of information on DNA sequences from many species culminating in the nearly completed human genome sequence[5,6]. In the post-genomic era, proteomics focuses not only on the structure properties of individual proteins, but also on the high throughput study of the expressions, interactions, and, to some extent, functions of large number of proteins. Therefore, biophysical approaches including biosensors in the proteomic era should provide data, complementary to the detailed molecular protein structures, revealing insight into how proteins behave in their natural environment, and how they interact dynamically with each other[7].

1.2 Optical Biosensor

Optical biosensors comprise transducers for detecting the presence of biological molecules. A conventional spectrophotometer tuned to a wavelength adsorbed by a protein is an example of an optical biosensor, but the term has acquired a more specific usage, signifying a transducer which can detect the presence of molecules on a surface. Although optical transducers all depend upon the special properties of light interacting with a solid/liquid interface, they can be divided into two categories[8]. In the first category, *e.g.* ellipsometry, SAR (scanning angle reflectometry) and OWLS (optical waveguide lightmode spectroscopy), the fundamental properties such as phase and amplitude of the reflected light are recorded directly and used to calculate the number of analyte molecules present at the interface via the extended Fresnel reflection coefficients. In the second category, *e.g.* TIRS (total internal reflection spectroscopy) and SPR (surface plasmon resonance), the complementary information is obtainable at the expense of a complete description of the adsorbed layer.

Compared with classical homogeneous solution methods for investigating molecular recognition, optical biosensors offer several assets: (1) generally there is no need to label the molecules being detected; (2) they can be used to monitor recognition processes in real time *in situ*; (3) many important biological recognition processes take place at surfaces, which is therefore a highly relevant environment; (4) signal/noise ratios are better, hence sensitivity is higher.

Among optical biosensors, the most commercially available detection instrument is SPR or related spectroscopies (evanescent waveguide or refractometry) to monitor the changes of the refractive index at the solid/liquid interface. The first commercial SPR biosensor was released by Biacore (Uppsala, Sweden) in 1990[9]. Just as the name of the company, BIA, which is the abbreviation of "biomolecular interaction analysis", SPR instruments are designed to detect the molecular recognitions and reactions on the surface. A recent paper[10] has documented that judicious use of SPR to measure interactions on the surface can provide data equivalent to, or better than, solution methods of analysis.

SPFS (surface plasmon field-enhanced fluorescence spectroscopy)[11,12], recently developed and based on SPR technology, has enabled successful quantitative analysis of oligonucleotide and other trace targets. Moreover, the ability of SPFS for simultaneously monitoring the interfacial refractive index changes and the fluorescence variations presents the possibility of biological activity detection of intrinsic fluorescent proteins or biomolecules.

1.3 Aim of the Study

One key factor in biosensor construction is the development of immobilization technologies for stabilizing biomolecules and tethering them to the surfaces[1]. The usual aim is to produce a thin film of immobilized biologically active material on or near the transducer surface which responds only to the presence of one or a group of materials or substances requiring detection. Since the immobilization technique used to attach the biological material to the sensor surface is crucial to the operational behavior of the biosensor, realistic strategies for the development of immobilization techniques are essential for practically useful biosensors.

There are a number of requirements that the immobilization technique must satisfy if biosensors are to be of practical use: (1) the biological component must retain substantial biological activity as well as long-term stability when attached to the sensor surface; (2) the biological film must remain tightly associated with the sensor surface whilst retaining its structure and function; (3) the biological material needs to have a high degree of specificity to a particular biological component; (4) the sensor surface can be regenerated. Our research focuses on the requirements for biomolecular immobilization and the various attachment methods used for protein immobilization in biosensors. However, for different objects being investigated, the emphasis is not identical.

A controlled immobilization of molecules on the surface is an essential requirement in most areas of supramolecular engineering and molecular nanotechnology. Contrary to conventional carriers where the location, local density, and orientation of functional groups and porosity are only know approximately, with S-layer lattices, the properties of a single constituent unit are replicated with the periodicity of the lattice and thus define the characteristic of the whole two-dimensional array[13]. Meanwhile, it has already been proved that functional groups can be incorporated in S-layers in dense crystalline packing[14]. Thus, our research of interest in Chapter 4 is to fabricate such a supramolecular platform according a to S-layer lattice in SPR biosensors for biotin-streptavidin based molecular interaction.

The fundamental basis of immunosensors is the specificity of the molecular recognition of antigens by antibodies to form a stable complex, which is similar to the immunoassay methodology. The immunosensor is now considered as a major development in the immunochemical field. Despite an overwhelming number of papers, a future substitution of traditional immunoassays by immunosensors simply depends on the successful solution to some fundamental issues related to immobilization, orientation, and specific recognition features of the antibodies or antibody-related reagents on the transducer surface[15]. In Chapter 5, we take the signature pregnancy molecule, hCG, as an example, trying to build a sensitive SPFS-based hCG immunoassay which is able to reach the requirements for clinical diagnostics.

Green plants obtain all their energy by photosynthesis, the process in which light is converted to chemical energy. Multi-protein complexes called photosystems, as the structural unit for photosynthesis, catalyze the conversion of the light energy captured in excited chlorophyll molecules to useful forms. A photosystem contains a reaction center plus a light-harvesting, or antenna, complex[16]. The knowledge of how the antenna complexes transfer the sunlight energy directionally to the reaction center and how they handle the maximum energy collection efficiently while avoiding photo-damage is potentially useful for constructing artificial devices for the conversion of solar energy, *e.g.* solar cells, and for designing electronic devices on a molecular scale[17]. In Chapter 6, we endeavor to anchor light-harvesting complex II on a gold surface by different immobilization strategies while maintaining their biological activities and long-term durability. Meanwhile, attempts were made to mimic the resonance energy transfer among the neighboring complexes by recording such transfer simultaneously, helping to solve some fundamental issues on the biomimetic solar cell design.

2 THEORETICAL BACKGROUND

2.1 Surface Plasmon Optics

Surface plasmon resonance (SPR) is an electron charge density wave phenomenon that arises on the surface of a metallic film when light is reflected at the film under specific conditions. The resonance is a result of energy and momentum being transformed from incident photos into surface plasmons, and is sensitive to the refractive index of the medium in contact to the metal film. The phenomenon of anomalous diffraction on diffraction gratings due to the excitation of surface plasmon waves was initially described in the beginning of the twentieth century by Wood[18] although it was the works by Otto[19], Kretschmann and Raether[20], Agerwal[21], and Swalen[22] that brought understanding and showed the versatility of the technique.

2.1.1 Evanescent Wave and Surface Polaritons

2.1.1.1 Total Internal Reflection (TIR) and Evanescent Wave

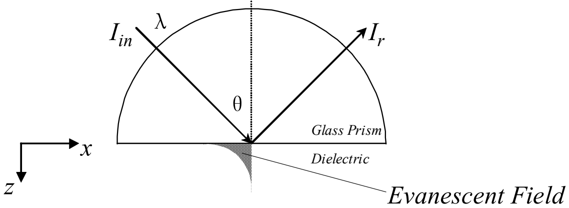

Figure 2.1: TIR of a plane wave of wavelength λ and intensity I_{in} at the base of a glass prism with in contact with a dielectric medium of $\varepsilon_d < \varepsilon_p$. For incident angles $\theta > \theta_c$, the critical angle for total internal reflection, the evanescent field at the interface decays exponentially into the dielectric with a decay length *l*.

In order to describe SPR, it is helpful to start with the phenomenon of total internal reflection which occurs at an interface between two media of different optical properties described by their different dielectric functions, ε_i[23]. As shown in Figure 2.1, a light beam (wavelength λ) propagating in a medium with higher refractive index $n_p = \sqrt{\varepsilon_p}$, *e.g.* glass prism, hits an interface at a medium with lower refractive index $n_d = \sqrt{\varepsilon_d}$, *e.g.* water, at an angle of incidence above a critical angle θ_c, is totally reflected at the interface and propagates back into the high refractive index medium. θ_c is given by Snell's law and depends on the refractive indices of the two media.

Although the fully reflected beam does not lose any net energy across the TIR interface, a scrutinization of the optical field near the interface would indicate that above the critical angle, the optical electric field along the propagation direction, E_x, has the oscillatory character of an electromagnetic mode, while the component perpendicular to the interface, E_z, does not fall to zero abruptly, but decays exponentially with a decay length l which is a function of the angle of incidence

$$l = \frac{\lambda}{2\pi\sqrt{(n \cdot \sin\theta)^2 - 1}}, \qquad \theta > \theta_c. \qquad \textbf{--- 2.1}$$

Such an electromagnetic field distribution is called an evanescent wave[24].

2.1.1.2 Surface Polaritons at a Noble Metal/Dielectric Interface

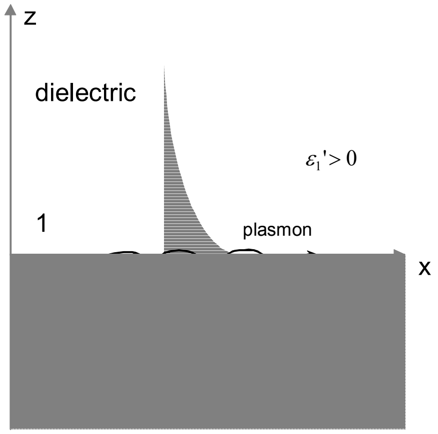

Figure 2.2: Schematic presentation of a surface plasmon at the interface between a metal and a dielectric. Note the sign of the two media need to be opposite to allow for plasmon excitation.

If the TIR interface is coated with a thin noble metal layer so as to provide an optical resonator, one is still dealing with an evanescent wave phenomenon, however, with a few significant differences.

As shown in Figure 2.2, we consider an interface in the *xy*-plane between two half-infinite spaces, 1 and 2, whose optical properties can be described by their complex dielectric functions $\varepsilon_1 = \varepsilon_1' + i\varepsilon_1''$ and $\varepsilon_2 = \varepsilon_2' + i\varepsilon_2''$, respectively. Ignoring magnetic materials, surface polaritons can only be excited at such an interface if the dielectric displacement $\vec{D}$ of the electromagnetic mode has a component normal to the surface (*z*-direction) which can induce a surface charge density σ,

$$(\vec{D}_2 - \vec{D}_1) \cdot \vec{z} = 4\pi\sigma \qquad \textbf{--- 2.2}$$

The electric field of an electromagnetic plane wave can be described in a complex form by the equation:

$$\vec{E} = \vec{E}_0 e^{i(\vec{k} \cdot \vec{r} - \omega t)} \qquad \textbf{--- 2.3}$$

where $\vec{E}_0$ is the electric field amplitude, $\vec{k}$ is the wavevector pointing into the propagation direction, $\vec{r}$ is the position vector, *ω* is the angular frequency (*ω=2πf*) and *t* is the time. The magnitude of $\vec{k}$ is given by:

$$|k| = \sqrt{\mu\mu_0 \varepsilon\varepsilon_0 \omega^2} \qquad \textbf{--- 2.4}$$

where μ and μ_0 are the magnetic permeability (dimensionless) and magnetic permeability in free space, respectively, ε and ε_0 are dielectric constant (without dimension) and dielectric constant in free space, respectively.

S-polarized light (transversal electric (TE) waves) propagating along the *x*-direction possesses only electric field components, $\vec{E}_i = (0, E_y, 0)$, parallel to the surface, and hence are unable to excite surface polaritons. Only p-polarized light (transversal magnetic (TM) waves) modes with $\vec{E}_i = (E_x, 0, E_z)$ or, equivalently, $\vec{H}_i = (0, H_y, 0)$ can couple to such modes. Therefore, the resulting surface electromagnetic wave will have the following form:

$$\begin{aligned} \vec{E}_1 &= (E_{x1}, 0, E_{z1}) e^{i(\vec{k}_{x1}\vec{x} + \vec{k}_{z1}\vec{z} - \omega t)} \\ \vec{H}_1 &= (0, H_{y1}, 0) e^{i(\vec{k}_{x1}\vec{x} + \vec{k}_{z1}\vec{z} - \omega t)} \end{aligned} \quad z > 0$$

$$\begin{aligned} \vec{E}_2 &= (E_{x2}, 0, E_{z2}) e^{i(\vec{k}_{x2}\vec{x} + \vec{k}_{z2}\vec{z} - \omega t)} \\ \vec{H}_2 &= (0, H_{y2}, 0) e^{i(\vec{k}_{x2}\vec{x} + \vec{k}_{z2}\vec{z} - \omega t)} \end{aligned} \quad z < 0 \qquad \textbf{--- 2.5}$$

where $\vec{k}_{x1}$ and $\vec{k}_{x2}$ are the wavevectors in *x*-direction and $\vec{k}_{z1}$ and $\vec{k}_{z2}$ are those in *z*-direction. Both fields $\vec{E}$ and $\vec{H}$ must fulfill the Maxwell equations:

$$\begin{aligned} \nabla \cdot \vec{H} &= 0 \\ \nabla \cdot \vec{E} &= 0 \\ \nabla \times \vec{E} + \frac{1}{c}\frac{\partial \vec{H}}{\partial t} &= 0 \\ \nabla \times \vec{H} - \frac{\varepsilon}{c}\frac{\partial \vec{E}}{\partial t} &= 0 \end{aligned} \qquad \text{--- 2.6}$$

with c being the speed of light in vacuum. Considering the continuity relations of the in-plane components:

$$\begin{aligned} E_{x1} &= E_{x2} \\ H_{y1} &= H_{y2} \end{aligned}, \qquad \text{--- 2.7}$$

inserting (2.7) into (2.5) yields:

$$k_{x1} = k_{x2} = k_x . \qquad \text{--- 2.8}$$

And it follows from Equations (2.5) and (2.6) that

$$\begin{aligned} k_{z1}H_{y1} &= \frac{\omega}{c}\varepsilon_1 E_{x1} \\ k_{z2}H_{y2} &= -\frac{\omega}{c}\varepsilon_2 E_{x2} \end{aligned} . \qquad \text{--- 2.9}$$

Together with the continuity relations (2.7), this leads to the only nontrivial solution if:

$$\frac{k_{z1}}{\varepsilon_1} + \frac{k_{z2}}{\varepsilon_2} = 0 . \qquad \text{--- 2.10}$$

This indicates that surface electromagnetic modes can only be excited at interfaces between two media with dielectric constants of opposite sign. As mentioned above, we are dealing here with the interface between a metal ($\varepsilon_2 = \varepsilon_m = \varepsilon_m' + i\varepsilon_m''$) and a dielectric material ($\varepsilon_1 = \varepsilon_d = \varepsilon_d' + i\varepsilon_d''$), and the coupling is essentially the collective plasma oscillations of the nearly free electron gas in a metal to an electromagnetic field. These excitations are called plasmon surface polaritons (PSP) or surface plasmons (SP).

From (2.6) and (2.9), one can obtain:

$$k_x^2 + k_{zd}^2 = (\frac{\omega}{c})^2 \varepsilon_d . \qquad \text{--- 2.11}$$

Inserting (2.10) into (2.11) leads to the dispersion relationships (i.e. the energy momentum relation) for surface plasmons at a metal/dielectric interface:

$$k_x = \frac{\omega}{c}\sqrt{\frac{\varepsilon_m \cdot \varepsilon_d}{(\varepsilon_m + \varepsilon_d)}}\ . \qquad \textbf{--- 2.12}$$

In the usual treatment, ω is taken to be real. Since ε_m is complex, k_x is also complex. Therefore, the amplitude of the electric field decays exponentially into both media in *z*-direction as well as into the propagation direction. The penetration depth of the evanescent filed wave, l_c, is usually defined as the distance over which the wave decays to 1/*e*, or about 37%, of its maximum intensity. For $\lambda =$ 632.8 nm light at gold/water interface, L_x is ~27 *nm* at the gold side, and ~242 *nm* at the water side. The propagation length, L_x, can be calculated by $L_x = 1/2k_x^{"}$. For $\lambda =$ 632.8 nm light at gold/air interface, L_x = 10 μm, while the length becomes 4 μm at gold/water interface. This decay has a strong impact on lateral resolution of methods like surface plasmon microscopy. The damping of the electromagnetic field will cause heat, dissipating into the metal and the dielectric.

2.1.2 Surface Plasmon Spectroscopy with Prism Coupling

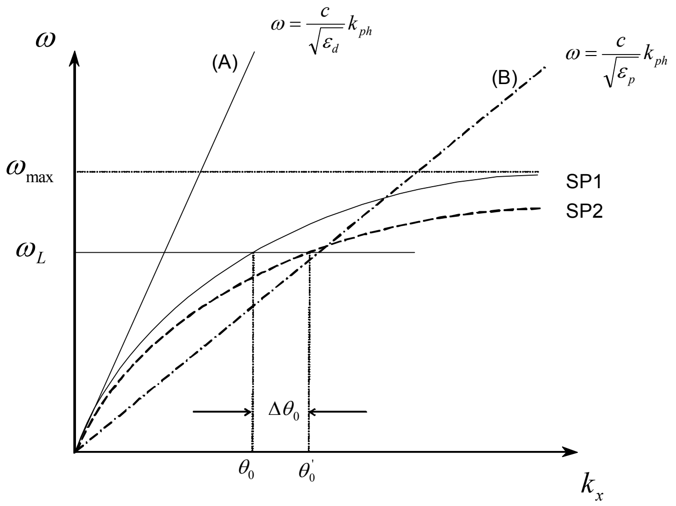

Figure 2.3: The dispersion relation of free photos in a dielectric (A), and in a coupling prism (B), compared to the dispersion relation for non-radiative surface plasmons at the metal/dielectric interface before (SP1) and after (SP2) the adsorption of an additional dielectric layer.

In the frequency (spectral) range of interest we have:

$$\sqrt{\frac{\varepsilon_m \cdot \varepsilon_d}{(\varepsilon_m + \varepsilon_d)}} \geq \sqrt{\varepsilon_d}\ . \qquad \text{--- 2.13}$$

This leads to the consequence that the momentum of a free photon propagating in a dielectric medium (line (A) in Figure 2.3),

$$k_{ph} = \frac{\omega}{c}\sqrt{\varepsilon_d}\ , \qquad \text{--- 2.14}$$

is always smaller than the momentum of a surface plasmon mode (curve SP1 in Figure 2.3), propagating along an interface between that same medium and the metal. Thus, it tells us that in addition to the energy conservation, this is not sufficient to fulfill the momentum matching condition for resonant SP excitation because, for very low energies, the SP dispersion curve asymptotically reaches the line (A), whereas for higher energies it approaches the cutoff angular frequency ω_{max} determined by the plasma frequency of the employed metal, ω_p:

$$\omega_{\max} = \omega_p \Big/ \sqrt{1+\varepsilon_d}\ . \qquad \text{--- 2.15}$$

It is therefore important to note, that surface plasmons are not directly excited by light in vacuum, unless the wavevetor of the free photos, is increased by passing the photos through a medium with higher refractive index than the dielectric, or adding a grating vector through the periodically corrugated surface structure to match the plasmon wavevector at the interface. Experimentally, the former can be achieved by reflecting the incident light on the base plate of a high refractive index prism, namely, the prism coupling, and the latter can be realized by the grating coupling.

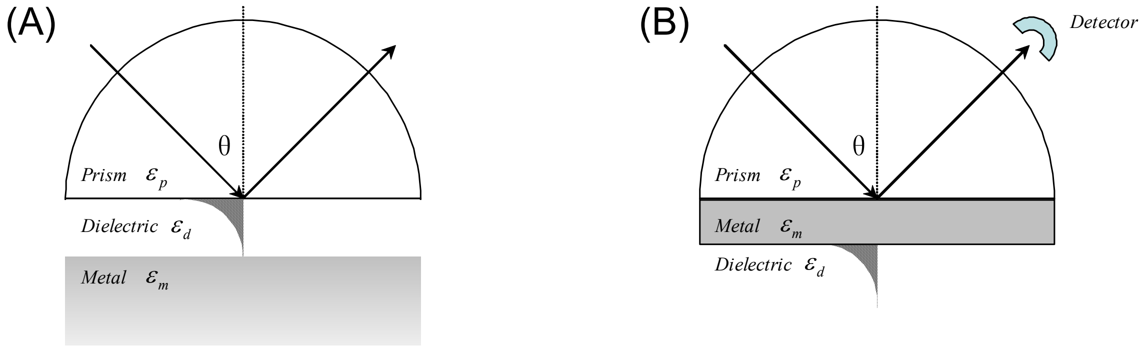

Figure 2.4: Prism coupling geometries for Otto configuration (A) and Kretschmann-Raether configuration (B). Coupling is only possible when the refractive index of the prism is higher than that of the dielectric.

By far, the prism coupling is the most predominant coupling techniques for increasing the wavevector of the incident light, k_{ph}, and also the main technique which will be discussed in our research. Various shapes of prisms can be used for exciting PSP, such as triangular prisms, half cylindrical prisms, hemispheral prisms. For simplicity, we will use half cylindrical prisms in the discussion of this chapter, to avoid considering of angle conversion by refraction at the air/prism interface.

In the prism coupling, the light travels through the high refractive index prism **(**$\varepsilon_p > \varepsilon_d$**)**, characterized by a larger momentum of $k_{ph} = \frac{\omega}{c}\sqrt{\varepsilon_p}$, which for a certain spectral range can exceed the momentum of the SP to be excited on the metal surface (cf. line (B) in Figure 2.3). For the excitation of surface plasmons, only the photo wavevector projection to the x-direction is the relevant parameter. Hence, resonant coupling between the incident photons and surface plasmons can be obtained by choosing the appropriate angle of incidence θ_0,

$$\begin{gathered} k_{ph}\sin\theta_0 = \frac{\omega_L}{c}\sin\theta_0\sqrt{\varepsilon_p} = k_{sp} = k_x = \frac{\omega_L}{c}\sqrt{\frac{\varepsilon_m\cdot\varepsilon_d}{(\varepsilon_m+\varepsilon_d)}} \\ \theta_0 = \arcsin\sqrt{\frac{\varepsilon_m\cdot\varepsilon_d}{(\varepsilon_m+\varepsilon_d)\cdot\varepsilon_p}} \end{gathered} . \qquad \textbf{--- 2.16}$$

Two prism coupling geometries are schematically shown in Figure 2.4, which are called Otto configuration and Kretschmann-Raether configuration, respectively. In the case of the Otto configuration (cf. Figure 2.4 (A)), the evanescent field bridges a 200 nm wide air gap between the prism and the metal, and the plasmons are excited at the metal/air interface[19]. Since this configuration is experimentally challenging, it has not gained any practical importance[25]. The Kretschmann-Raether configuration (cf. Figure 2.4 (B)) is more versatile because it is much easier to realize[20]. In this most widespread version of surface plasmon spectroscopy, the photos in the prism couple through a very thin metal layer to the PSP states at the other side in contact with the dielectric medium. The thickness of the metal film influences the coupling angle, θ_0, as well as the coupling efficiency, *e.g.* the minimum reflectivity. This dependence can be simulated by Fresnel's equations using the transfer matrix methods. For the excitation by $\lambda =$ 632.8 nm He-Ne laser light, an optimal thickness is in the range of 47 nm for gold with dielectric function $\varepsilon_m = -12.3 + 1.29i$.

2.1.3 SPR Response to a Thin Film Deposition

If one makes the experiment by recording the reflected intensity, *e.g.* with a diode detector (cf. Figure 2.4 (B)), as a function of the angle of incidence, θ, a typical SPR angular-dependent reflectivity scan curve will be produced and the critical angle for TIR, θ_c, as well as the appropriate angle for the resonance minimum, θ_0, can be observed. Such a typical resonance curve of the prism/gold/water system is shown in Figure 2.5 in solid line.

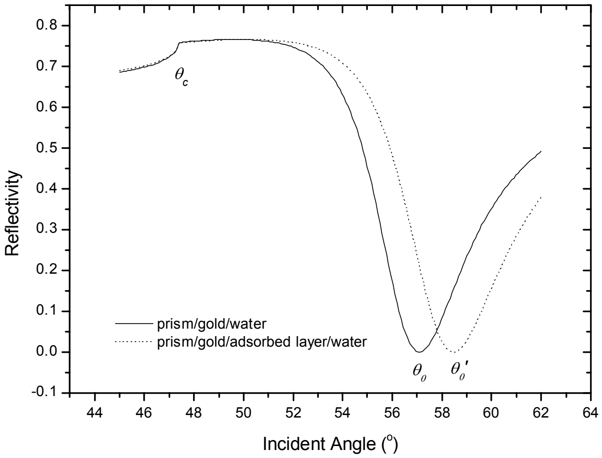

Figure 2.5: Typical surface plasmon resonance curves of the prism/gold/water system before (solid line) and after (dot line) the deposition of an ultrathin layer onto the gold.

Since the evanescent field of the surface plasmons decays exponentially into the dielectric medium, changes of the optical properties of the adjacent dielectric will alter the excitation conditions for plasmons. If an ultrathin and non-adsorbing layer with different dielectric constant ($\varepsilon_f \neq \varepsilon_d$) is deposited onto the metal layer, it will induce a change on the overall dielectric function integrated over the range of the evanescent field, thus shifts the SPR resonance minimum angle. This can be directly inferred from (2.16), where the new dielectric function ε_d' is larger than the original one, ε_d, which results in a higher resonance minimum angle, θ_0'.

Similarly, k_{sp} in the surface plasmon dispersion equation (2.12) shifts to a larger wavevector, depicted as curve SP2 in Figure 2.3. This can be expressed mathematically by:

$$k_{sp2} = k_{sp1} + \Delta k \qquad \text{--- 2.17}$$

where k_{sp1} and k_{sp2} are the surface plasmon wavevectors before and after the adsorption. It is important to note that the increment Δk depends strongly on the refractive index and the thickness of the adsorbed layer. At a given frequency ω_L, the intersection with the dispersion relation of the photons is therefore shifted towards a higher k value. As a consequence, the angle of incidence that determines the photon wavevector projection along the SP propagation direction has to be slightly increased to fulfill the resonance criterion (cf. Figure 2.3, from θ_0 to θ_0'). This is also experimentally shown in Figure 2.5 where the angular scan curve is shifted from the left (solid line) to the right (dotted line).

In conclusion, in the case of the adsorption of an ultrathin, non-adsorbing layer defined by a thickness d and a refractive index n, the resonance angle displacement $\Delta\theta$ is proportional to the optical thickness nd of the layer:

$$\Delta\theta \propto n \cdot d\,. \qquad \text{--- 2.18}$$

If the refractive index of the material is known, the geometrical thickness can be determined, and vice versa. This characteristic resonance minimum shift is one of the most fundamental and significant features for the practical application in methods like surface plasmon spectroscopy or microscopy.

On the other hand, for the surface mass chance resulting from the protein immobilization, through the calibration between the reflectivity responses measured by our home-made setup and Biacore, Yu[26] deduced an empirical equation for the calculation of the surface protein concentration A by the angle of resonance minimum shift $\Delta\theta$:

$$A = \frac{\Delta\theta}{0.19^{o}}(ng \cdot mm^{-2})\,. \qquad \text{--- 2.19}$$

2.2 Fluorescence

Fluorescence labeling and staining, when combined with an appropriate analytical instrument, is a sensitive and quantitative method that is widely used in the fields of biochemistry and molecular biophysics today. These fluorescence spectroscopy techniques offer a number of important advantages, *e.g.* sensitivity, multiple-label possibility, stability, low hazard, commercial availability, lower cost, *etc.*. The concept of using fluorescence label techniques in connection with surface plasmon optics as a means to enhance the signal of the interfacial binding events has been realized by surface plasmon field-enhanced fluorescence spectroscopy (SPFS)[11].

2.2.1 Fluorescence Process

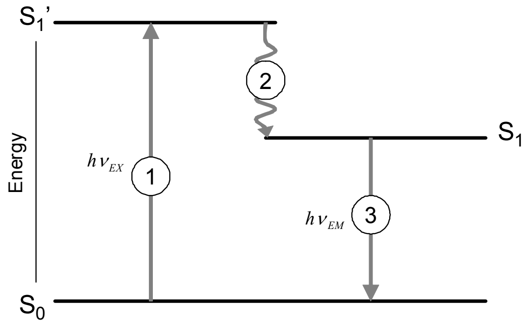

Figure 2.6: Jablonski diagram illustrating the process involved in creating an excited electronic singlet state by optical absorption and subsequent emission of fluorescence. ① Excitation; ② Vibrational relaxation; ③ Emission.

Fluorescence results from a process that occurs if certain molecules (generally polyaromtic hydrocarbons or heterocycles) called fluorophores, chromophores, fluorochromes, or fluorescent dyes absorb light. The absorption of light raises their energy level to an excited state. As they relax from this excited state, they emit fluorescence light[27]. The three-stage process responsible for fluorescence is illustrated by a simple electronic state diagram (cf. Figure 2.6).

If a photon of energy, $h\nu_{EX}$, supplied by an external source such as a lamp or a laser, is absorbed by a fluorophore, an excited, unstable, electronic state (S_1') is created.

The excited state of a fluorophores is characterized by a very short half-life, usually on the order of a few nanoseconds. During this brief period, the fluorophores undergoes conformational changes and is also subject to a multitude of possible interactions with its molecular environment. As a consequence, the energy of S_1' is partially dissipated, yielding a relaxed singlet excited state (S_1) from which fluorescence emission originates. Additionally, other processes such as collisional quenching, fluorescence energy transfer and intersystem crossing may also depopulate molecules from S_1. The fluorescence quantum yield, Φ, which is the ratio of the number of fluorescence photons emitted to the number of photos absorbed, is a measure of the efficiency of fluorescence in competition with these other processes.

A photon of energy $h\nu_{EM}$ is emitted, returning the fluorophores to its ground state S_0. Due to energy dissipation during the excited-state lifetime, the energy of this photon is lower, and therefore of longer wavelength than the excitation photon $h\nu_{EX}$. The difference in energy or wavelength represented by ($h\nu_{EX}$ -$h\nu_{EM}$) is called the Stokes shift.

2.2.2 Fluorescence Resonance Energy Transfer (FRET)

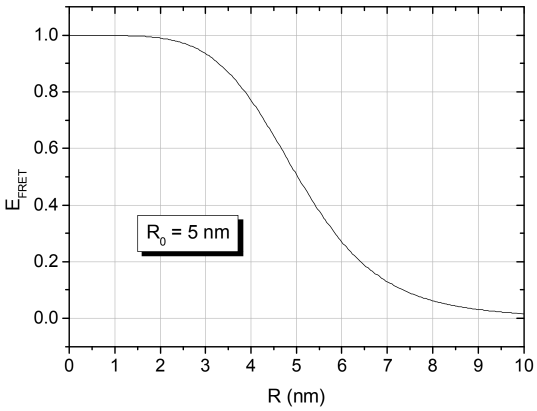

Figure 2.7: Schematic example of FRET efficiency dependent on the donor-acceptor distance.

Fluorescence resonance energy transfer (FRET), or Förster resonance energy transfer, is a distance-dependent interaction between the electronic excited states of two dye molecules in which excitation is transferred from a donor molecule to an acceptor molecule without emission[28]. As discussed in Section 2.2.1, an excited donor molecule has several routes to release its captured energy returning to the ground state. The excited state energy can be dissipated to the environment (as light or heat) or transferred directly to a second acceptor molecule, sending the acceptor to an excited state. The latter process is called FRET. Once excited, the acceptor can return to the ground state by the same pathways as the donor. If the acceptor molecule is also fluorescent, it can emit light at its characteristic wavelength, which is always longer than the emission wavelength of the donor.

The rate (k_T) and efficiency (E) of FRET are expressed as follows respectively:

$$k_T = R_0{}^6 R^{-6} \tau_D{}^{-1} \qquad \text{--- 2.20}$$

$$E = k_T \big/ (\tau_D{}^{-1} + k_T) = \frac{1}{1 + (R/R_0)^6} \qquad \text{--- 2.21}$$

where τ_D is the decay time of the donor in the absence of acceptor, R is the donor-acceptor distance, R_0 is the Föster distance where FRET has 50% efficiency, typically in the range of 20-60 Å[29]. An example of FRET efficiency versus donor-acceptor distance if the Föster distance is 5 nm is shown in Figure 2.7. R_0 is determined by the following equation:

$$R_0{}^6 = 8.79 \times 10^{23} [\kappa^2 n^{-4} \Phi_D J(\lambda)] \qquad \text{--- 2.22}$$

where κ^2 is dipole-dipole orientation factor (ranging from 0 to 4, $\kappa^2 = 2/3$ for randomly oriented donors and acceptors), n is the refractive index, Φ_D is the fluorescence quantum yield of the donor in the absence of the acceptor. $J(\lambda)$ is the FRET spectral overlap integral as illustrated in Figure 2.8, determined by the following equation:

$$J(\lambda) = \int F_D(\lambda) \varepsilon_A(\lambda) \lambda^4 d\lambda \qquad \text{--- 2.23}$$

where $F_D(\lambda)$ is the fluorescence emission intensity of the donor as a fraction of the total integrated intensity, $\varepsilon_A(\lambda)$ is the extinction coefficient of the acceptor at λ.

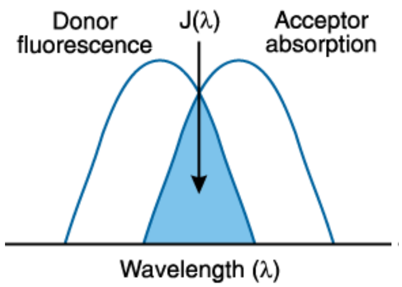

Figure 2.8: Schematic representation of the FRET spectral overlap integral.

From (2.21), (2.22) and (2.23), it is easily concluded that an efficient FRET should have the following conditions:

- donor and acceptor molecules must be in close proximity (typically 10-100 Å);
- the absorption spectrum of the acceptor must overlap the fluorescence emission spectrum of the donor (cf. Figure 2.8);
- donor and acceptor transition dipole orientations must be approximately parallel.

The distance dependence of FRET has resulted in its widespread biological applications since the distances are comparable with the dimensions of biological macromolecules. Thus, FRET has become a powerful technique for studying conformational distribution and dynamics of biological molecules[30].

2.2.3 Surface Plasmon Field-Enhanced Fluorescence Spectroscopy (SPFS)

Surface plasmon spectroscopy has matured into a well-accepted analytical tool for the characterization of interfaces and thin films as well as for the sensitive detection of kinetic processes, e.g. for monitoring interfacial binding reactions[24,31]. With a lower limit for a reliable signal detection corresponding to an effective layer of about 0.1-0.2 nm, SPR has generated a sufficient signal-to-noise level allowing for a detailed kinetic analysis and determination of binding kinetics[32]. However, problems arise if only a very dilute lateral packing of the proteins can be achieved or if very small analytes of low molecular weight are to be detected, resulting in angular shifts too low to be observed[33]. Therefore, the concept of SPFS combining surface plasmon spectroscopy with fluorescence label techniques is developed to enhance the signal response of the interfacial binding events.

2.2.3.1 Field Enhancement

As shown in Figure 2.5, the critical angle, θ_c, whose value is determined only by the refractive indices of the prism and the dielectric medium, indicates the onset of the attenuated total reflection (ATR) phenomenon. The resonance minimum angle, θ_0, on the other hand, suggests the condition where the incident photons wavevector matches the surface plasmon wavevector at the metal/dielectric interface. At this resonance angle, almost all the energy of the incident radiation is converted into surface plasmon excitation and the intensity of the electromagnetic field is greatly enhanced, expressed as the lowest reflectivity.

The enhancement factor is given by the ratio of the magnetic field intensity on the metal surface at the dielectric side divided by the incoming magnetic field intensity for p-polarized light[34]. The calculated intensities are normalized to the incident intensity and are plotted together with the corresponding reflectivity in Figure 2.9 depending on the angle of incidence for three-phase systems prism/Ag/water and prism/Au/water. Peak intensities scaled against the incoming intensity can reach an enhancement factor of 58 for the former and 16 for the latter. Generally, the smaller the imaginary dielectric constant *ε''*, i.e. the lower the absorption and hence dissipation of the optical field intensity, the higher the enhancement factor.

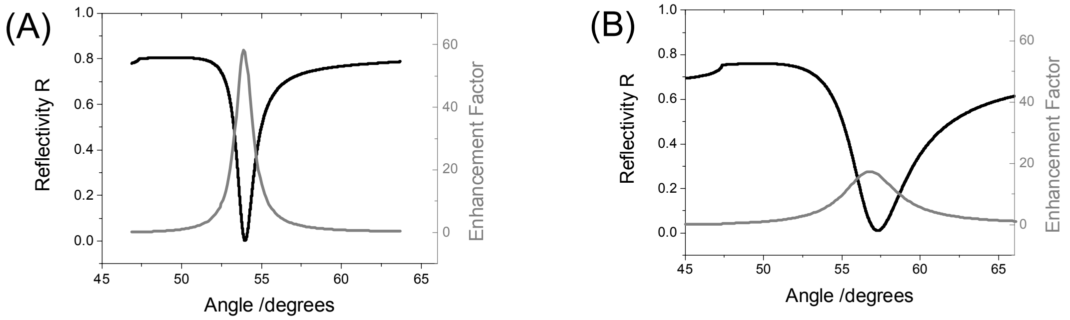

Figure 2.9: Simulation curves of the reflectivity and the relative field intensity as a function of the He-Ne laser light incident angle on three-phase systems prism/Ag/water (A) and prism/Au/water (B).

This field enhancement phenomenon is well known and widely applied in other spectroscopy technologies, *e.g.* surface-enhanced Raman scattering (SERS)[35].

2.2.3.2 Fluorescence at the Metal/Dielectric Interface

In the case of total internal reflection, only a moderate field enhancement by a factor of 4 is obtained at the critical angle due to constructive interference between the incoming and reflected electromagnetic field. This enhancement together with the evanescent character of this surface light triggered its successful use in total internal reflection fluorescence (TIRF)[36]. As mentioned above, the electromagnetic field enhancement of SPR is more substantial than that of TIR, as a consequence, much stronger fluorescence emission should be obtained if the fluorophores are excited by surface plasmon evanescent wave.

As discussed in Section 2.1.1.2, the evanescent field decays exponentially into the dielectric layer adjacent to the metal film with the characteristic parameter, the penetration depth, at which the surface field intensity drops down to *1/e* of the interface value, typically several hundred nanometers into the dielectric medium. Therefore, surface plasmon sensitive fluorescence measurements will only be possible if the dyes is in close proximity to the metal film.

However, the electronic coupling of the molecular orbitals localized in the chromophore with the extended band structure of the metallic electrons in the solid substrate generates new decay channels for the excitation energy of the dye, leading to a strong modification of radiative lifetimes and fluorescence intensities as the fluorophores are coming closer and closer to the metal surface[11]. Figure 2.10 summarizes some of the observed distance-dependent energy transfer mechanisms.

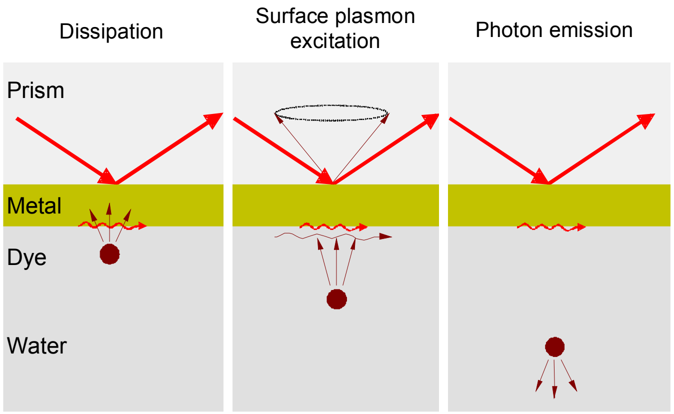

Figure 2.10: Schematic of the different electronic coupling regimes for a fluorophore in water at different distances to a metal film surface.

If a dye is positioned at a distance within 10 nm to the metal surface, a substantial ‘radiation-less’ de-excitation with a corresponding reduction of the radiative lifetime and the fluorescence intensity is found. The fluorescence is ‘quenched’, dissipating the excitation energy in the metal as heat. This quenching phenomenon can be modeled by the Förster resonance energy transfer, showing a R^{-6} dependence of the transfer efficiency to the separation distance. However, integrating over all possible sites of an entire surface of acceptors will yield a R^{-4} dependence (cf. dashed curve in Figure 2.11).

At an intermediate-distance regime (a few nm up to ~20 nm), the optically excited chromophores can effectively couple back to the plasmonic states of the metal substrate. Since some of the excitation energy is dissipated in the dye molecule via vibronic excitation, the corresponding back-coupled surface plasmon mode is red-shifted relative to the excitation and hence re-radiates in a cone via the prism at a slightly smaller angle.

At sufficient separation distances (>20 nm), free emission of the fluorophores can be achieved. The fluorescence intensity only depends on the intensity of the evanescent field except for some (negligible) interference effects between the radiation field directly emitted and the one reflected from the metallic surface.

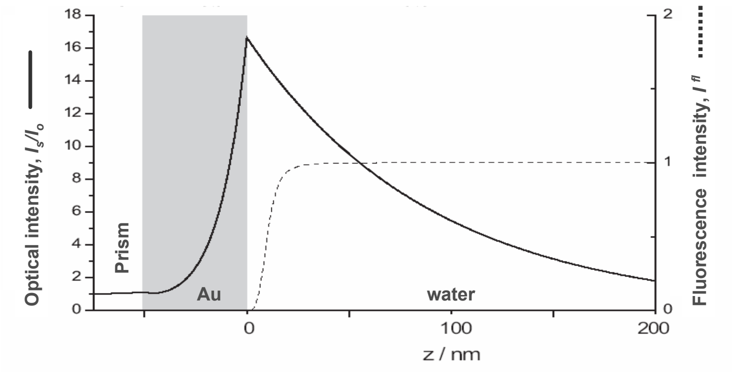

Figure 2.11: Comparative presentation of the distance dependence of the optical field enhancement of a surface plasmon evanescent wave mode excited at a prism/Au/water interface (solid curve), and the Förster energy transfer mechanism, expressed as the relative fluorescence intensity (dashed curve) placed at a certain distance above the metal/water interface.

Figure 2.11 summaries these findings in their consequence for the design of an interfacial architecture optimized for maximum sensitivity enhancement by combining the spatial characteristics of surface plasmon fields and the quantum efficiency for radiative dipoles near a metal surface. In contrast to the quenching processes that only occur for chromophores within 10-15 nm of the surface, the exponential decay of the surface plasmon field ranges on a much longer distance of several hundred nanometers. This means that fluorescent species placed at least 1 Förster distance (typically 5-7 nm) away from the surface experience a loss in the fluorescence intensity of a factor of 2 at most.

They are still in the largely enhanced optical field of a resonantly excited surface plasmon mode used for chromophore excitation. Therefore, by carefully designing the supramolecular interfacial layers proving the binding sites for the recognition process of fluorescently labeled analyte, one can gain enormously in detection sensitivity by exploiting the enhanced surface plasmon optical field without being compromised by the quenching mechanism.

2.3 Langmuir Isotherm

Biomolecules carry out their roles *in vivo* by interaction with one or more binding partners. Hence, a quantitative analysis of these recognition events *in vitro* provides an illuminating insight into biological function and mechanism[37]. The classical Langmuirian model of interaction in free solution is used as a foundation for the development of analytical methodologies for the interaction analysis. The simplest physically plausible isotherm is based on three assumptions[38]:

1) Adsorption cannot proceed beyond monolayer coverage;
2) All sites are equivalent and the surface is uniform;
3) The ability of a molecule to adsorb at a given site is independent of the occupation of neighboring sites.

For the reversible interaction observed between an immobilized ligand B and a soluble ligate A, we have:

$$A + B \underset{k_{off}}{\overset{k_{on}}{\Leftrightarrow}} AB \, . \qquad \textbf{--- 2.24}$$

The rate of complex AB formation is described by the association rate constant k_{on}, which has units of $M^{-1}s^{-1}$. The rate of complex dissociation is described by k_{off}, which has units of s^{-1}. The rate of association of A with B is equal to $k_{on}[A][B]$. The rate of dissociation of AB is equal to $k_{off}[AB]$. On mixing A and B, association and dissociation of AB will occur. Equilibrium will eventually be reached if the rates of association and dissociation of AB are equal. At equilibrium, $[AB]$, $[A]$ and $[B]$ are constant. Hence, at equilibrium:

$$k_{on}[A][B] = k_{off}[AB]. \quad \text{--- 2.25}$$

This may be rearranged as follows:

$$\frac{[A][B]}{[AB]} = \frac{k_{off}}{k_{on}} = K_D \quad \text{--- 2.26}$$

where K_D is termed the dissociation equilibrium constant, and has units of M. The lower the value of K_D, the greater the affinity. The reciprocal term K_A, the association equilibrium constant, having units of M^{-1}, is sometimes used in the literature as the measure of affinity, where:

$$K_A = \frac{1}{K_D}. \quad \text{--- 2.27}$$

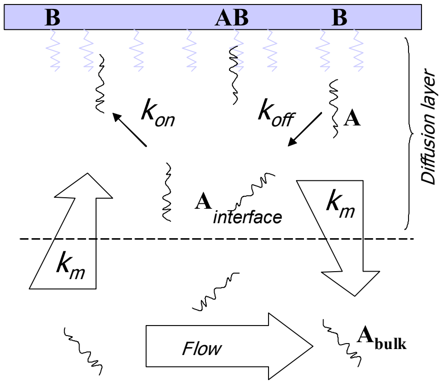

Figure 2.12: Schematic showing basic interactions on the biosensor surface. The ligand (B) is attached to the surface via a flexible linker. During the association phase, analyte (A) is flowed past the surface. k_m is the mass transport coefficient used to describe the diffusion of analyte through the diffusion layer. k_{on} and k_{off} are the association and dissociation rate constants, which describe the formation of the complex (AB).

However, as shown in Figure 2.12, at a solid/liquid interface, the transportation of A from the bulk solution to the interface has to be taken into account. Thus, the formation of the complex AB will be also influenced by the mass-transport rate constant k_m from the bulk to the interface and from the interface to the bulk, expressed as:

$$\frac{d[AB]}{dt} = k_f[A_{bulk}][B] - k_r[AB] \quad \text{--- 2.28}$$

where k_f is the forward rate constant, and k_r is the reverse rate constant. From (2.24), at the interface, there is also:

$$\frac{d[AB]}{dt} = k_{on}[A_{interface}][B] - k_{off}[AB]. \quad \text{--- 2.29}$$

Combination of (2.28) and (2.29) will yield:

$$k_f = \frac{k_{on}k_m}{k_m + k_{on}[B]} = \frac{k_{on}}{1+\frac{k_{on}[B]}{k_m}}, \qquad k_r = \frac{k_{off}k_m}{k_m + k_{on}[B]} = \frac{k_{off}}{1+\frac{k_{on}[B]}{k_m}}. \qquad \text{--- 2.30}$$

If k_m is very small, or the surface concentration of B is very large, i.e. $k_m << k_{on}[B]$, the interaction is controlled by the mass-transport rate:

$$\frac{d[AB]}{dt} = k_m[A_{bulk}] - \frac{k_m k_{off}}{k_{on}[B]}[AB]. \qquad \text{--- 2.31}$$

At the initial association stage, $[AB]$ is very small, the complex forming rate is solely dependent on the bulk concentration of A, and the binding signal increases linearly with time t:

$$\frac{d[AB]}{dt} = k_m[A_{bulk}]. \qquad \text{--- 2.32}$$

This can be used for the concentration analysis of ligate A.

If the mass-transport rate is much larger than the association rate constant, or the surface concentration of the immobilized species is low, i.e., $k_m >> k_{on}[B]$, then $[A_{interface}] = [A_{bulk}]$. k_f and k_r approximately equal to the intrinsic rate constants k_{on} and k_{off}. Under such conditions, the binding rate can be expressed as:

$$\frac{d[AB]}{dt} = k_{on}[A][B] - k_{off}[AB]. \qquad \text{--- 2.33}$$

After some reaction time, t, $[B] = [B]_0 - [AB]$, where $[B]_0$ is the concentration of B at $t=0$. As shown in Figure 2.12, the ligands are immobilized onto the surface and the ligates are continuously replenished from the injection volume flowing over the surface. The signal observed, R, is proportional to the formation of AB complexes on the surface and the maximum signal, R_{max}, is proportional to the surface concentration of active ligands on the surface. Therefore, (2.33) becomes:

$$\frac{dR}{dt} = k_{on}C(R_{\max} - R) - k_{off}R \qquad \text{--- 2.34}$$

where C is the constant concentration of ligates in solution. This yields the solution:

$$R_t = \frac{k_{on}CR_{\max}}{k_{on}C + k_{off}}(1 - e^{-(k_{on}C + k_{off})t}) = R_{eq}(1 - e^{-(k_{on}C + k_{off})t}) \qquad \text{--- 2.35}$$

where R_{eq} is the equilibrium response at a given ligate concentration C. If considering about the baseline correction, (2.35) becomes:

$$R_t = (R_{eq} - R_{t=0})(1 - e^{-(k_{on}C + k_{off})t}) + R_{t=0} \qquad \text{--- 2.36}$$

where $R_{t=0}$ is an additional fitting parameter equivalent to the signal at the point of injection of ligates ($t = 0$), which is not zero.

In the dissociation process, where C = 0 because of the fresh buffer rinse, (2.34) becomes:

$$\frac{dR}{dt} = -k_{off} R \qquad \text{--- 2.37}$$

The solution for (2.37) is:

$$R_t = R_0 e^{-k_{off} t} \qquad \text{--- 2.38}$$

where R_0 is the response at the start of the dissociation process. If considering about the baseline correction, (2.38) becomes:

$$R_t = (R_0 - R_{t \to \infty}) e^{-k_{off} t} + R_{t \to \infty} \qquad \text{--- 2.39}$$

where $R_{t \to \infty}$ is the response value after infinite time and represents complete dissociation of the AB complexes. Equation (2.36) and (2.39) can be utilized to yield k_{on} and k_{off} from a single set of association and dissociation data via nonlinear least squares fit.

On the other hand, the interaction dynamic also can be deduced from the equilibrium analysis. Upon equilibrium of the dynamics, the net effect of the association and the dissociation process is zero, from (2.34) one obtains:

$$R_t = R_{eq} = \frac{k_{on} C R_{\max}}{k_{on} C + k_{off}} = \frac{C R_{\max}}{C + {}^{k_{off}}\!/_{k_{on}}} = \frac{C R_{\max}}{C + K_D} = \frac{C K_A R_{\max}}{C K_A + 1} \qquad \text{--- 2.40}$$

which gives the equilibrium response at a given analyte concentration C. Experimentally, this can be achieved by a stepwise saturation of the ligand on the surface by a series of concentrations of ligates, or titration method in this research. Plotting these equilibrium responses R_{eq} as a function of the ligate concentration C results in the well-known Langmuir adsorption isotherm. The dissociation equilibrium constant K_D can be obtained directly from this curve as being equal to the ligate concentration at $R_{max}/2$. Meanwhile, a plot of C/R_{eq} as a function of C yields a straight line with a slope of $1/R_{max}$ and a y-axis intercept of $1/R_{max}K_A$.

3 EXPERIMENTAL METHODS

3.1 SPFS Setup and Liquid Handling System

3.1.1 Home-Made SPFS Setup

The surface plasmon resonance setup used for the described study was based on a conventional Kretschmann configuration, which is also the most widely used geometry in SPR sensors[39]. The schematic description of the setup is depicted in Figure 3.1.

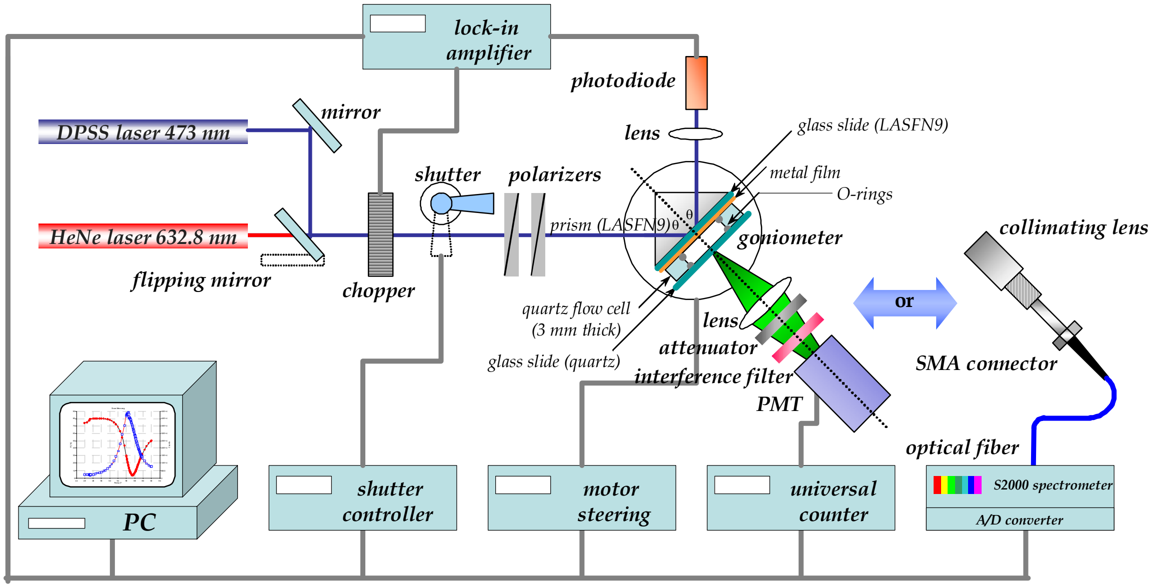

Figure 3.1: Schematic of a surface plasmon spectroscopy setup in the Kretschmann configuration combined with modules for the fluorescence absolute value detection or the fluorescent spectrum detection.

In this setup, surface plasmons can be excited by two different lasers, which is a Helium-Neon (HeNe) laser (Uniphase, 5mW, λ = 632.8 nm) and a Nd:YAG Diode Pumped Solid-State (DPSS) laser (CrystaLaser, 5mW, λ = 473 nm) respectively. A manually controlled flipping mirror (Owis) is utilized to select between the two lasers. The continuous laser beam passes through a chopper (Perkin Elmer, frequency = 1331 Hz) connected to a lock-in amplifier (Perkin Elmer). A PC-controlled shutter is also mounted in the optical path in order to minimize the photobleaching of the fluorophores. Two polarizers (Glan-Thompson) are used next, adjusting the plane of polarization and the intensity of the laser. Finally, the laser beam enters a right angle coupling prism (Schott, LASFN9, n = 1.85 @ $\lambda =$ 632.8 nm) and is reflected off the metal/dielectric interface, focused by a convex lens (Owis, f = 50 mm) onto a photodiode detector which is connected to the same lock-in amplifier as the chopper. The prism/sample unit and the photodiode detecting unit are mounted on two-axial goniometers (Huber) with the precision of 0.001° rotational movements, enabling an independent tuning of respective angular positions. Normally, the former unit rotates at θ, while the latter unit rotates at 2θ, relative to the fixed excitation laser beam, in the surface plasmon resonance scan measurements.

The fluorescence detection module is mounted along the normal direction of the metal-dielectric interface, rotating together with the prism/sample unit. In a general surface plasmon field-enhanced fluorescence mode, the fluorescence emission emitted normal to the meta/dielectric base plane is collected by a focusing lens (Owis, f = 50 mm) and passes through an interference filter (LOT, λ = 671 nm, transmittance = 60%, for Cy5 (Cyanine 5, from Amersham Pharmacia Inc.) or Alexa Fluor 647 (from Molecular Probes Inc.) excitation, λ = 680 nm, transmittance = 50%, for LHCII excitation, $\Delta\lambda$ = 10 nm for both cases) to block the scattered and out-coupled excitation light, before it's finally gathered by a photomutiplier tube (PMT, Hamamatsu), which is connected to a universal counter (Agilent) via a home-made electronic interface to convert analog to digital data, expressed in counts per second (cps). In the case where the fluorescence light intensity is beyond the PMT's linear input-versus-output range ($< 2.5\times10^{6}$ cps), an appropriate attenuator (neutral filter, LOT) is added to weaken the intensity according to its attenuation factor.

Two modes of operation are possible: an angular scan mode in a θ–2θ reflection geometry, or a kinetics mode in order to resolve time-dependent processes at a fixed angle of observation. For both modes, the reflectivity channel as well as the fluorescence intensity channel can be recorded simultaneously. Data acquisition and electronics control are accomplished by custom programs.

While this normal mode of SPFS only detects the absolute fluorescence intensity values convoluted with the bandpass of the interference filter, the full spectroscopic information of surface excited chromophores can be obtained by replacing the above fluorescence detection module with a spectrometer unit, consisting of a UV collimating lens, an optical fiber cable, an A/D converter with USB interface and a S2000 miniature fiber optic spectrometer (all from Ocean Optics Inc.). With the modified SPFS, one can obtain the full surface-enhanced fluorescence spectrum near the resonance angle, which indicates the behavior of surface-bound chromophores, and the fluorescence spectrum of homogeneously distributed chromophores in the bulk solution, which is primarily excited by the radiation of refraction and transmission below the critical angle.

3.1.2 Flow Cell and Liquid Handling System

Although Ward and Winzor concluded that microfluidics- (*e.g.* Biacore sensor) and cuvette-based (*e.g.* IAsys sensor) biosensor provided essentially equivalent opportunities for detecting and quantifying macromolecular interactions[40], we still choose a microfluidics flow cell as the default liquid handling system, for its distinctive features of uniformity of the ligate solution in contact with the sensor surface, feasibility of reducing the potential contribution of mass-transfer processes, comparatively low sample consumption, *etc*.. The schematics of the flow cell attached to the prism coupling unit in the SPR setup is also shown in Figure 3.1. The prism is index matched to a glass slide (Schott, LASFN9) which is metal coated and constitutes one side of the flow cell. The cell body is made of a low fluorescence quartz glass (Schott, Herasil) sealed with O-rings against the metal and the quartz cover slide (Schott, Herasil). As presented in Figure 3.2, both the inlet and outlet ports of the flow cell are connected to hollow steel needles with an outer diameter of 1 mm, positioned in a symmetric way, in order to get highly efficient liquid switching. The flow cell is attached to the sample tube via Tygon tubing with an inner diameter of 0.76 mm, to form a loop through which liquid phase is continuously circulated by a peristaltic pump (Ismatec). The volume of the reaction chamber is about 85 µl while the volume of the whole loop is about 300 µl. In order to ensure a thorough liquid switching, at least 500 µl sample solution is needed. The flow cell is mounted perpendicularly together with the prism/sampling unit, with the inlet at the bottom and the outlet on the top, in order to remove the miniscule stagnant air bubbles aggregating at the static metal-solution interface during extended measurements. The solution exchange is accomplished manually, and a high circulation rate of 3.641 ml/min is the default flow rate to reduce the influence of mass-transport kinetics unless otherwise stated.

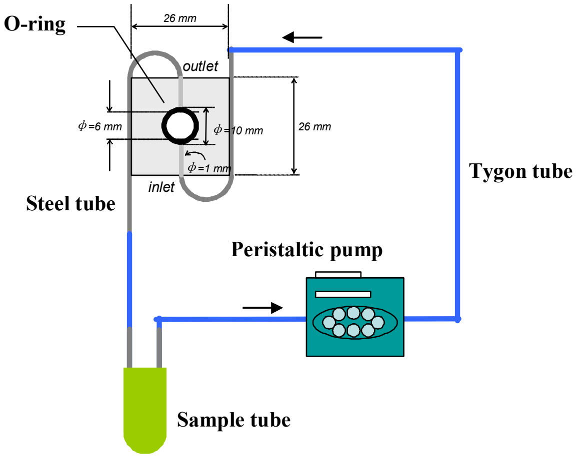

Figure 3.2: Sketch of the closed-loop circulation system with the integration of a flow cell.

3.2 Surface Modification Techniques

In the following the applied techniques that were used to modify surfaces with metallic and dielectrics films are illustrated.

3.2.1 Substrate and Metal Film Preparation

High refractive LASFN9 glass slides (25×25×2.5 mm, Schott, n = 1.85 @ λ = 632.8 nm) are used in all experiments. After the cleaning process of 15 minutes ultrasonic treatment in 2% Hellmanex (Helma) aqueous solution, followed by 15 minutes ultrasonic treatment in MilliQ water and 15 minutes ultrasonic treatment in Ethanol (Fisher Scientific), the slides are desiccated in a stream of nitrogen and placed directly into the thermal evaporation apparatus (Edwards, FL400) for further processing.

For optimal surface plasmon spectroscopic measurements with the excitation by a HeNe laser (λ = 632.8 nm), a gold (99.99%, Balzers materials) film with a thickness of 47 nm is needed, whereas for energy transfer experiments with LHCII with the Chlorophyll *b* excitation by a Nd:YAG DPSS laser (λ = 473 nm), a silver (Balzers materials) film with a thickness of 23 nm followed by a gold film of 5 nm is advisable. Since the rate of the deposition might have an influence on the surface roughness of the metal layer, all the evaporations are accomplished at a deposition rate of 0.1 nm/s under ultra-high vacuum condition (*ca.* 5×10^{6} mbar). After that, the slides are removed from the apparatus to be stored separately under Argon until further use within one week.

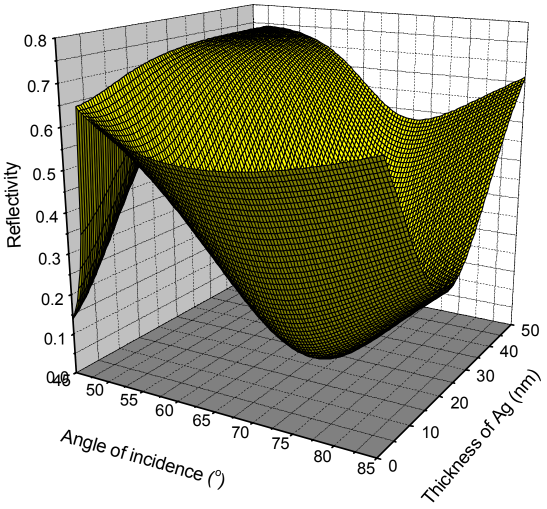

Figure 3.3: ATR scan curves with respect to the variation of silver thickness protected by 5 nm gold.

It is worthy to note that as indicated by Equation (2.10), surface electromagnetic modes can only be excited at interfaces between two media with dielectric constants of opposite sign. For excitation by a blue laser, the dielectric function of gold, $\varepsilon_{Au} = -1.6 + 4.5i$[41], with a small real part close to zero, and a large imaginary part resulting in strong dissipation, prevents from plasmon resonance excitation. On the other hand, silver, with the dielectric function of $\varepsilon_{Ag} = -7.3 + 0.7i$[41], is able to be utilized for PSP excitation. However, silver has long been known to be unstable in air or solution for its ease of oxidation, therefore, 5 nm of gold is always evaporated onto the silver film as a protection layer. This ultrathin layer of gold also broadens the resonance width of ATR scan curve. Therefore, as shown in Figure 3.3, the thickness of the silver film needs to be carefully tuned in order to get the optimal resonance. At this optimized thickness combination of 23 nm of silver and 5 nm of gold, the magnetic field enhancement factor is 3.5 and the electric field enhancement factor is 10.5.

3.2.2 Self-Assembled Monolayers

Highly stable molecular layers prepared by the self-assembling method have been applied for the development of various detection systems such as electrochemical detection, optical detection, and so on. Self-assembled monolayers (SAMs) are molecular assemblies that are formed spontaneously by the immersion of an appropriate substrate into a solution of an active surfactant in an organic solvent[42]. In particular, thiol compounds with gold[43,44], silver[42], copper[45] or platinum[46] are well-established combinations. However, most of the work to date has been made on gold surfaces, mainly because of the fact that gold does not have a stable oxide, and thus it can be handled in ambient conditions.

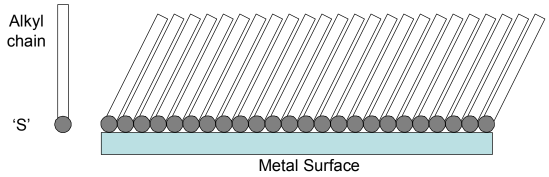

Figure 3.4: A self-assembled monolayer of alkanethiols on a metal surface.

The self-assembling process of alkanethiols on gold is initiated by the strong chemical interactions between the sulfur and gold surface. This interaction is considered to be the result of chemisorption that forced a thiol molecule to adsorb in a way commensurate with the gold lattice. Then, the tail-to-tail interaction of the molecules created by lateral interchain interactions, such as by van der Waals, steric, repulsive and electrostatic forces, is strong enough to align the molecules parallel on the gold surface and create a close-packed, oriented crystalline film[42] (cf. Figure 3.4).

Formation of binary SAMs has long been a strategy to functionalize sensor surfaces[47,48]. In general, these methods involves the self-assembling process in a mixed thiolates solution, composed of one species with a functional end group (*e.g.* biotin) and the other species with a passive end group (*e.g.* hydroxyl). The fabrication of such SAM structures might result in maximizing the ligate binding density, controlling the orientation of the immobilized ligate and minimizing nonspecific binding of other components in the bulk solution. The structural formulae of the thiol couple used to attach streptavidin are given in Figure 3.5. The ratio of passive spacer thiol to biotin-terminated thiol has been set at 9:1 in the mixed solution prepared in absolute ethanol (Fisher Scientific, HPLC grade) with a net thiol concentration of 500 μM according to the optimization result by Spinke[49]. The solution is brought into contact with the gold film in a home-made Teflon incubation cell and allowed to self-assemble overnight at room temperature. Subsequently, the slides are removed, rinsed thoroughly with ethanol and blown dry by a stream of nitrogen, then stored under an Argon atmosphere until use.

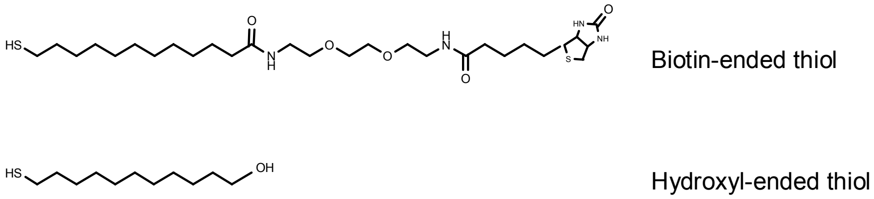

Figure 3.5: Chemical structures of biotin-ended thiol and hydroxyl-ended thiol used to form the binary SAM for streptavidin coupling.

Similarly, other binary SAMs are prepared as the procedure mentioned above. The detailed conditions may be altered somewhat as will be stated when discussed later.

3.2.3 Spin coating for Deposition of Polystyrene Film

The spin coating technique is used to prepare films of variable thickness (nm-mm). The film material is dissolved in an appropriate solvent of different concentrations. After the sample is placed onto the spin coater, its surface is completely covered with the solution followed by spinning the sample at a moderate speed (2000-4000 rpm). After the appropriate time, the sample can be removed from the apparatus for further storage under Argon.

The resulting layer is a function of the used concentration, the used solvent, the rotation speed and the process duration. For polystyrene (Sigma-Aldrich), a solution prepared in toluene (Fisher Scientific) was used and the gold covered slide was spun for 60 seconds at a speed of 2000 rpm. The slide was placed into a heating oven (Memmevt) at a temperature of 100°C for 6 hours until all toluene solvent molecules are evaporated. The relation between the thickness of polystyrene layer on gold surface and the concentration of the toluene solution is presented in Table 3.1.

Concentration of Polystyrene	10 mg/ml	5 mg/ml	2.5 mg/ml	1 mg/ml
Thickness of Polystyrene on gold	40.2 nm	19.2 nm	9.1 nm	3.5 nm

Table 3.1: The relation between polystyrene thickness and polystyrene concentration.

3.2.4 Sol-gel Procedure for Deposition of Silica Film

Supramolecular architectures based on silane coupling chemistries on silica substrates are commonly used in many applications. One way to utilize SPR technology for monitoring surface interactions taking place on silica substrates is to thermally evaporate a thin layer of SiO_x onto the metal layer. However, in most cases, the interface of SiO_x/aquesous medium is not stable[50]. As an alternative, the following sol-gel procedure is used to deposit silicon oxide films on silver and gold samples.

1) A solution of ca. 20 mM 3MPT (3-(mercaptopropyl)trimethoxysilane, Fluka, previously vacuum-distilled) in anhydrous ethanol (Fisher Chemicals) was prepared;
2) Clean Au or Ag surfaces were immersed into above 3MPT solution to allow for a SAM to form for ca. 2 hours for Ag and 3 hours for Au. Caution was taken to avoid water contamination during these steps. Therefore the used glass-ware was dried in an oven and the reactions were carried out under Argon atmosphere;
3) After that the samples were rinsed with ethanol to remove unbound 3MPT followed by rinsing with MilliQ water;
4) In order to activate the surface the samples were placed in aqueous 0.1 M HCl for 1-12 hours;
5) The sol-gel solution was prepared 30 minutes before spin coating. After the mixing of water, HCl and methanol (Fisher Chemicals), TMOS (tetramethoxysilane, Fluka) was added and the solution was vigorously shaken. The mixture was allowed to react for 30 minutes and shaken or stirred periodically meanwhile. The final thickness of the sol-gel layer was determined by the rotation speed of the spin coating and the amount of TMOS in the solution. Typical mixtures are given in Table 3.2;
6) The 0.1 M HCl solution was removed from the samples by rinsing with MilliQ

water;

7) The samples were placed onto the spin coating apparatus;
8) Ca. 45 µl/cm^2 sol-gel solution was applied to the samples, in order to cover its surface completely prior to spinning.
9) The samples were spun at 3400 rpm for 1 minute, then placed into a dessicator for 2 days prior to use.

Water (µl)	163	163	163	163
0.1 M HCl (µl)	81	81	81	81
Methanol (µl)	55	55	55	55
TMOS (µl)	210	5	10	20
Thickness (nm)	3	8	15	30

Table 3.2: Typical spin coating solutions for sol-gel film of different thickness.

3.2.5 SCWP Activation and Self Assembly on Gold

As a natural anchoring molecule for S-layer proteins in the bacterial cell wall, secondary cell wall polymers (SCWPs) can not be coated on the gold surface directly by recrystallization unless the completion of the chemical modification showed in Figure 3.6. The experimental protocol for the integration of a sulphhydryl group into the polymer chain and the self assembly of activated SCWPs onto gold surface is as follows:

1) Add 0.5 ml 250 mM boric acid buffer (Sigma-Aldrich), pH 8.4, to dissolve the mixture of 1 mg amino-group terminated SCWPs and more than 1 mg iminothiolane;
2) Ventilate above solution with nitrogen or argon gas for 2 hours at room temperature to prevent the oxidation of the formed sulphhydryl groups;
3) Rinse the protein desalting column (Amersham Pharmcia Biotech) with degassed MilliQ water;
4) Transfer above solution into the column;
5) Elute the column with MilliQ water, the rinsed out solution is separated into 10 Eppendorf tubes with each tube 0.5 ml solution;
6) Take 30 µl solution out from every tube, add 20 µl Ellman's reagent (DTNB, 5, 5'-Dithiobis(2-nitrobenzoic acid), Sigma) to do Ellman's test[51], the sample including free thiol groups will produce a distinctive yellow color;

7) Collect the solution in the positive tubes, modify the pH value to 3.5 with 0.01 N HCl (Sigma-Aldrich);
8) Drop enough solution to the clean gold chip to cover the surface, incubate 30 minutes at room temperature;
9) Rinse the chips with MilliQ water and store them in containers with MilliQ water at 4 degrees.

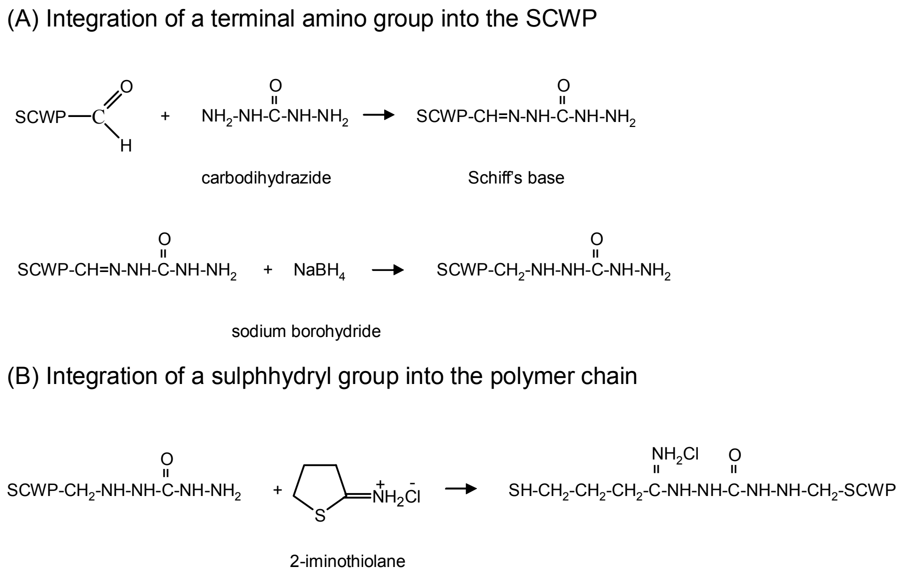
(A) Integration of a terminal amino group into the SCWP

(B) Integration of a sulphhydryl group into the polymer chain

Figure 3.6: Chemical Modification of the Secondary Cell Wall Polymer.

3.3 PREPARATION OF RECONSTITUTED LHCII SOLUTION FOR SURFACE IMMOBILIZATION

The problem of unavailability of large quantities of proteins intended for biophysical and structural studies has been successfully side-stepped in the case of soluble proteins by the recombinant route. In the case of membrane proteins this strategy faces a variety of problems because of the formation of insoluble aggregates, known as inclusion bodies[52] which seem to be developed when highly expressed recombinant proteins cannot be tolerated as soluble proteins in the cell cytoplasm. The proper way to reconstitute membrane proteins *in vitro* can overcome this barrier, making inclusion bodies as an excellent starting point for producing active membrane proteins in large quantities for structural and functional studies. Stable LHCP-pigment complexes can be refolded *in vitro* in detergent solution by mixing denatured LHCP with pigments and subjecting it to renaturing conditions such as a number of freeze-thaw cycles[53,54]. Later experiments showed that reconstitution can also be induced by adding a nonionic detergent like octyl glucoside (OG) to the pigment-protein mixture in lithium dodecylsulfate (LDS) and then removing most of the dodecyl sulfate by precipitation[55].

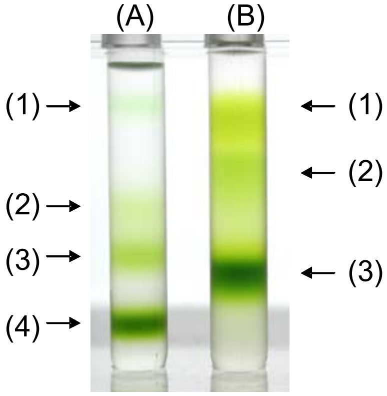

Figure 3.7: Separation of LHCII monomers and trimers by sucrose density centrifugation. The samples loaded on analytical sucrose density gradients were: (A) reconstituted LHCII monomers trimerized in the presence of lipids (PG); (B) reconstituted LHCII monomers treated in the same way as (A) except that no lipids were added. The labeling bands are (1) free chlorophylls, (2) intermediates, (3) monomers, (4) trimers.

The protocol of LHCII's reconstitution described in this chapter is based on the studies mentioned above.

1) Add the protein solution contained 100 μg LHCP into 50 μL reconstituted buffer (100 mM Tris, pH 9.0, 2% (w/v) SDS);
2) Add 5 μL 10 mM Dithiothreitol (DTT, Biomol) into the above solution;
3) After preparation of pigments solution containing 50 μg of total extract (cf. Section 6.2) dissolved in 5 μL ethanol, slowly mix it with aforementioned protein solution, stirred strongly by Vortex for 30 seconds simultaneously;
4) Add 7.5 μL 10% (w/v) n-Octyl-β-D-glucoside (OG, Bachem);
5) Further add 7.5 μL 2 M KCl, then keep the mixed solution in an ice box for 20 minutes;

6) Remove precipitated potassium dodecyl by centrifugation for 8 minutes with the rotation speed of 12000 rpm (Hettich Universal 30RF, Rotor 1412) at 4°C, harvest the clear supernatant solution (ca. 75 µL, containing 1% (w/v) OG);
7) Transfer the supernatant into a 4 mL centrifugation tube, add n-dodecyl-β-D-maltoside (DM, Sigma-Aldrich) to a final concentration of 0.1% (w/v) and sucrose (Merck) to a final concentration of 0.4 M;
8) Fraction different components in the solution by ultracentrifugation for 16 hours with the speed of 54000 rpm (Optima XL-100K, Class S) at 4°C;
9) Use a syringe to harvest the appropriate bands of reconstituted LHCII with different oligomeric state (cf. Figure 3.7). Store the complex solution at -20°C until further use.

For surface immobilization experiments, the ultrafiltration process needs to be completed before the binding in order to remove the high concentration of sucrose which will cause a strong detuning effect for the SPFS detection. The detailed protocol is as follows:

1) Take the reconstituted solution out from the refrigerator and thaw it in an ice box;
2) Mix 100 µl reconstituted solution and 400 µl detergent containing working buffer softly;
3) Insert the Microcon sample reservoir (YM-30, Millipore) into the filtrate vial, pipette above solution into the sample reservoir, seal with the attached cap;
4) Place the assembly in a compatible centrifuge and counterbalance with a similar device;
5) Spin with the speed of 14000×g at 4°C for 10 minutes;
6) Discard the filtrate in the vial, add more working buffer in the reservoir (0.5 ml maximum volume), repeat 5) for 2 or 3 times,
7) Remove the assembly from the centrifuge, separate the vial from the reservoir;
8) Place the sample reservoir upside down in a new vial, then spin 3 minutes at 1000×g to transfer the concentrate to the new vial;
9) Separate the sample reservoir and store the concentrated complex solution at 4°C for later use within 2 days. The concentrations of the complexes are calculated on the basis of the extinction coefficient of 546000 $M^{-1}cm^{-1}$ at λ = 670 nm as determined by Butler and Kühlbrandt[56].

4 S-LAYER MATRIX: ANOTHER STRATEGY FOR BIOMOLECULAR COUPLING

4.1 Introduction

Crystalline monomolecular cell surface layers (S-layers) are one of the most common outermost cell envelope components of prokaryotic organisms. These isoporous structures are composed of a single protein or glycoprotein species endowed with the ability to assemble into a closed lattice during all stages of cell growth and cell division, they can be considered the simplest type of biological membrane developed in the course of evolution[14].

S-layer proteins can be extracted from the bacterial surfaces with hydrongen-bond breaking agents such as guanidine hydrochloride (GHCl) or expressed heterologously in *Escherichia coli*[57,58]. Isolated S-layer subunits are able to assemble into monomolecular arrays either in suspension, at liquid-surface interfaces, on lipid films, on liposomes and on solid supports (e.g., polymers, metals, silicon wafers). The crystalline arrays exhibit oblique, square or hexagonal lattice symmetry[59] (cf. Figure 4.1). One morphological unit, also referred to as the unit cell, may consist of one, two, three, four or six identical protein subunits.

By genetic engineering methods, S-layer proteins can be incorporated in the outer surface of the protein lattice with functional domains, such as Z-domain, a synthetic analogue of the B-domain of protein A, capable of binding the Fc part of IgG[60], the variable domain of a heavy chain camel antibody against prostate-specific antigen (PSA)[61], the enhanced green fluorescent protein (EGFP)[62], and Strep-tag I[63] *etc.*, but not interfering with the self assembly properties of the proteins. Due to these unique features, S-layer technologies particularly provide new approaches for biotechnology, biomimetics, molecular nanotechnology, nanopatterning of surfaces and formation of ordered arrays of metal clusters or nanoparticles as required for nanoelectronics.

Subunits of most S-layer proteins interact with each other and with the supporting envelope layer (*e.g.* plasma membrane, outer membrane or peptidoglycan) by a combination of non-covalent forces including hydrogen or ionic bonds, and hydrophobic or electrostatic interactions[64]. Moreover, many S-layer proteins from *Bacillaceae* recognize a distinct type of pyruvylated heteropolysaccharide called secondary cell wall polymer (SCWP) which is covalently linked to the peptidoglycan matrix of the cell wall[65]. In bacteria S-layer-homologous (SLH), three motifs which have been identified at the N-terminal part of many S-layer proteins, are involved in forming the SLH-domain. The binding mechanism between SLH-domains and SCWPs is widespread among prokaryotes and is considered having been conserved during evolution[66].

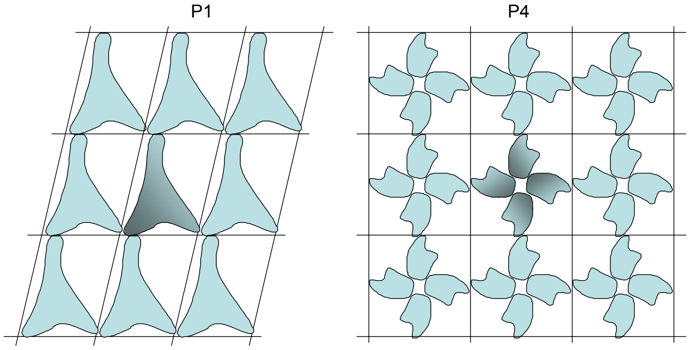

Figure 4.1: Schematic drawing of different S-layer lattice types. The regular arrays exhibit oblique (SbsB) or square (SbpA) lattice symmetry. The morphological units (shaded ones in the middle) are composed of one or four identical subunits.

In cooperation with Prof. Uwe B. Sleytr's group at the Center for Nanobiotechnology in Vienna, Austria, S-layer protein SbsB from *B. stearothermophilus* PV72/p2, an oxygen-induced strain variant from *Bacillus stearothermophilus* PV72/p6, and S-layer protein SbpA from *Bacillus sphaericus* CCM 2177 has been fully investigated about their self-assembly properties on gold surface characterized by SPR technique. In order to be fully utilized as the building blocks for streptavidin-biotin based biomolecular coupling systems, both targets can be streptavidin fused then refolded to heterotetramers consisting of one chain of the recombinant fusion protein and three chains of core streptavidin, which are called rSbsB-streptavidin heterotetramer (rSbsB-HT)[57] and rSbpA-streptavidin heterotetramer (rSbpA-HT)[67] respectively. The schematic morphology of the above S-layer proteins lattice is shown in Figure 4.1, and their corresponding characteristic features are given in Table 4.1. In this study, the possibility of S-layer fusion proteins as the basis to fabricate biosensors for DNA hybridization test will also be inspected.

	SbsB	**SbsB-HT**	**SbpA**	**SbpA-HT**
M_w of subunit	95 kDa	145 kDa	127 kDa	177 kDa
Lattice symmetry	Oblique		Square	
Base vectors	10.4 nm×7.9 nm		13.1 nm×13.1 nm	
Thickness of S-layer	4.5 nm	N/A	8 nm	N/A
Largest pore size	4 nm		4.5 nm	
Isoelectric point	5.08	N/A	4.2	4.95

Table 4.1: Characteristic features of S-layer proteins lattice.

4.2 Materials

All the SPFS experiments described in this chapter were made under HeNe laser excitation and the fluorescence intensity were recorded by a PMT.

Aqueous solutions were made in MilliQ water (Millipore, resistance > 18.2 MΩ/cm).

Tween®20 (Polyoxyethylene Sorbitan Monolaurate) was purchased from USB Corporation. Trizma®Base was from Fluka. Sodium hydroxide (NaOH) was from Aldrich. Calcium chloride ($CaCl_2$), guanidine hydrochloride (GHCl), n-Dodecyl-β-D-maltoside (DM), ethylenediaminetetraacetic acid disodium salt dihydrate (EDTA), phosphate buffered saline (PBS) tablets were purchased from Sigma-Aldrich.

PBST buffer refers to 10 mM phosphate buffer, pH 7.4, 137 mM NaCl, 2.7 mM KCl, 0.05% (v/v) Tween®20.

HBS-P buffer (degassed 10 mM HEPES buffered saline, pH 7.4, 150 mM NaCl, 0.005% (v/v) surfactant P-20 (equivalent to Tween®20)) was kindly provided by Biacore (Uppsala, Sweden). Eluent buffer refers to HBS-P buffer adding 50 μM EDTA and 0.1% (v/w) DM.

Biotinylated Hu8 was kindly provided by Prof. Harald Paulsen's group.

rSbpA, rSbpA-HT, rSbsB-HT and their corresponding SCWP were provided from Prof. Uwe B. Sleytr's group. Self assembly of thiolated SCWP on the gold surface was performed according to the protocol presented in Section 3.2.5.

All probes used in this study were commercially available (MWG GmbH) 30mer DNA sequences labeled with a biotin or thiol at the 5' terminal. All targets used (MWG GmbH) were 15mer DNA sequences labeled with a Cy5 chromophore at the 5' terminal. Nucleotide sequences of the probes and the targets are shown in Table 4.2.

5'-**Biotin**-T_{15}TGT ACA TCA CAA CTA-3'	Biotinylated P2
3'-ACA TGT AGT GTT GAT-**Cy5**-5'	T2 (MM0)
3'-ACA TG**C** AGT GTT GAT-**Cy5**-5'	T1 (MM1)
3'-ACA TG**C** A**C**T GTT GAT-**Cy5**-5'	T3 (MM2)
5'-**SH**-T_{15}TGT ACA TCA CAA CTA-3'	Thiolated P2

Table 4.2: Base sequences for different DNA probes and targets (mismatch base position underlined).

4.3 Recrystallization of S-layer Proteins on Gold or SCWPs

The ability of S-layer proteins to recrystallize into isoporous monomolecular arrays in suspension and at a broad spectrum of surfaces (e.g. silicon, metals, polymers) and interfaces (e.g. air/liquid interface or lipid films)[68] makes them the natural supramolecular footstones for biosensors investigation. Plenty of studies have been made for understanding the surface topography after recrystallization[14,57,64,68-70], most of which are through atomic force microscopy (AFM), scanning force microscopy (SFM) and transmission electron microscopy (TEM) technologies. SPR spectroscopy is used here to characterize the recrystallization process of S-layer proteins on gold and on their matching SCWPs.

For recrystallization experiments on gold or on SCWPs, S-layer proteins were generally dissolved at a concentration of 1 mg/ml in 5 M GHCl in 50 mM Tris-HCl buffer (pH 7.2) and dialyzed against MilliQ water for two hours with several changes of fresh MilliQ water. Potential self-assembly products were removed by centrifugation at 16,000×g for 5 minutes at 4^{o}C. The clear supernatant was diluted to a final concentration of 0.1 mg/ml in recrystallization buffer (0.5 mM Tris-HCl, pH 9.0, 10 mM $CaCl_2$) before each experiment.

The recrystallization process usually lasted for 30-60 minutes at a circulation rate of 3.6 ml/min.

4.3.1 Recrystallization of rSbpA on Gold

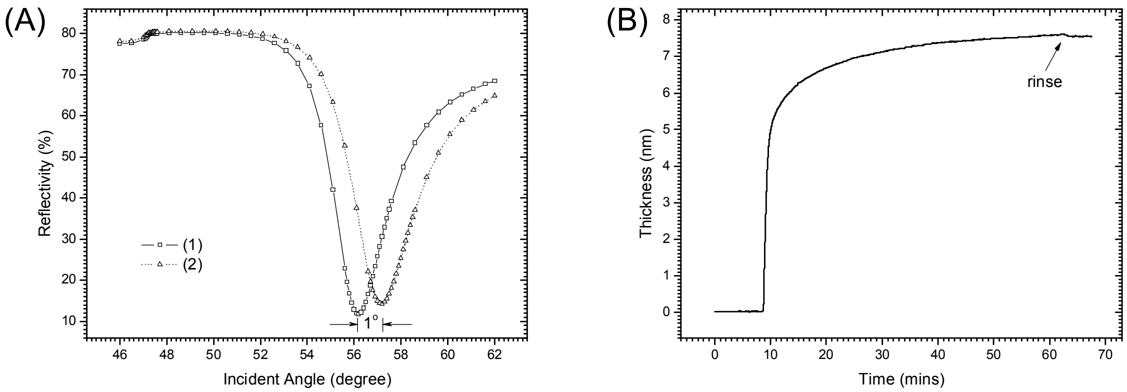

Figure 4.2: rSbpA's recrystallization on gold. (A) SPR scan curves before (1) and after (2) rSbpA's recrystallization. (B) The kinetic measurement of rSbpA's recrystallization.

As shown in Figure 4.2, rSbpA can recrystallize directly onto gold. The final thickness increment after rinse amounted to ca. 8 nm (at a refractive index of n = 1.45[49]), which was also the thickness of a rSbpA molecule (cf. Table 4.1). Meanwhile, the SPR angular shift for rSbpA's recrystallization was 1°, equal to a protein density of ~5.2 ng/mm^2 according to Equation (2.19). This value was consistent with a 100% surface coverage of rSbpA proteins, indicating the formation of a rSbpA proteins monolayer. The surface density for 100% coverage of rSbpA proteins is calculated as follows:

$$\frac{1mm^2}{13.1nm\times 13.1nm\times 6.02\times 10^{23}mol^{-1}}\times 127kg/mol\times 4=4.9ng/mm^2 \qquad \textbf{--- 4.1}$$

4.3.2 Recrystallization of rSbsB-HT on SCWPs

On the other hand, SH-functionalized SCWP for rSbsB could self assemble onto gold to form a ~4 nm thick polymer layer (assuming a refractive index of n = 1.45) (cf. Figure 4.3). C-terminal rSbsB-HTs (streptavidin was attached to the C-terminus of rSbsB) were bound on such SCWP in recrystallization buffer next (cf. Figure 4.3), resulting in a ~8 nm thick protein layer. The calculated surface density of rSbsB-HT was ~6 ng/mm^2, twice the theoretical value for 100% coverage with rSbsB-HTs (~3 ng/mm^2). Both results imply a branched structure of S-layer proteins on SCWPs (cf. Figure 4.6 (A)).

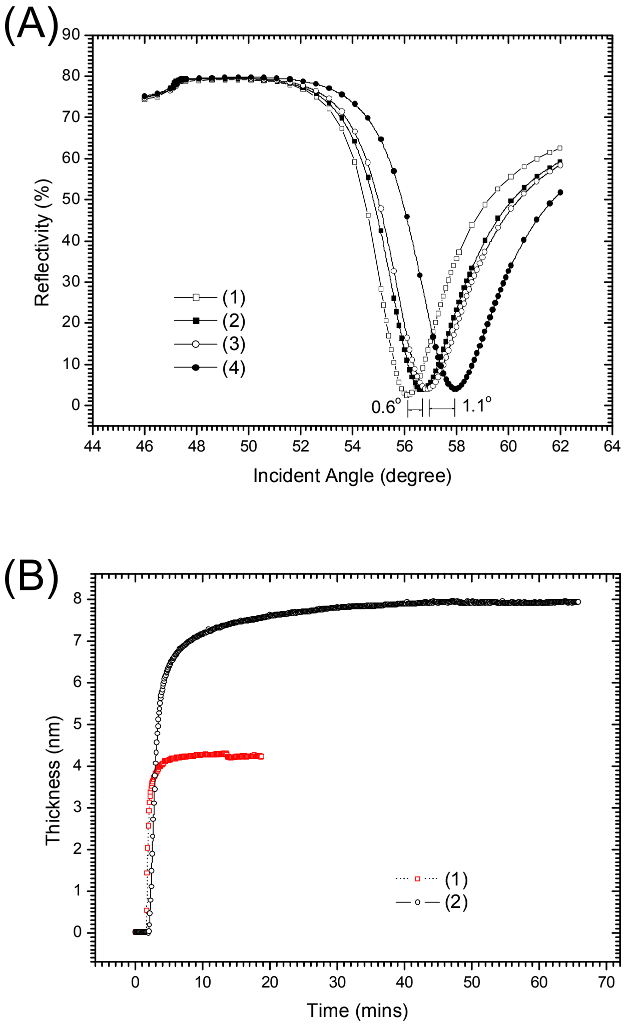

Figure 4.3: rSbsB-HT's recrystallization on SCWPs. (A) SPR scan curves before (1) and after (2) self assembly of SCWP, as well as before (3) and after (4) rSbpA's recrystallization. The difference between (2) and (3) was caused by the buffer exchange. (B) The kinetic measurements about SCWP's self assembly in MilliQ water (1) and rSbpA's recrystallization (2).

4.3.3 Recrystallization of rSbpA-HT on Gold and on SCWPs

There's no big difference between the mass changes caused by self assembly of rSbpA-HTs directly onto gold or by indirectly recrystallization of rSbpA-HTs on gold supported SH-functionalized SCWPs. The former produced a protein layer with a thickness of 7.52 nm, while the latter resulted in a 9.37 nm thick protein layer. Since there is no direct information about the thickness of one rSbpA-HT protein molecule, we could only give a rough estimate based on the thickness of rSbpA protein and conclude that the recrystallization process should also form a rSbpA-HT protein monolayer. The SPR angular shift of 1.025° and 1.25° for above recrystallization corresponded to 5.4 ng/mm^2 and 6.6 ng/mm^2 of protein density, respectively. These values were also in accordance with the theoretical coverage of a complete rSbpA-HT monolayer (6.3 ng/mm^2), which is some degree higher than that of rSbpA.

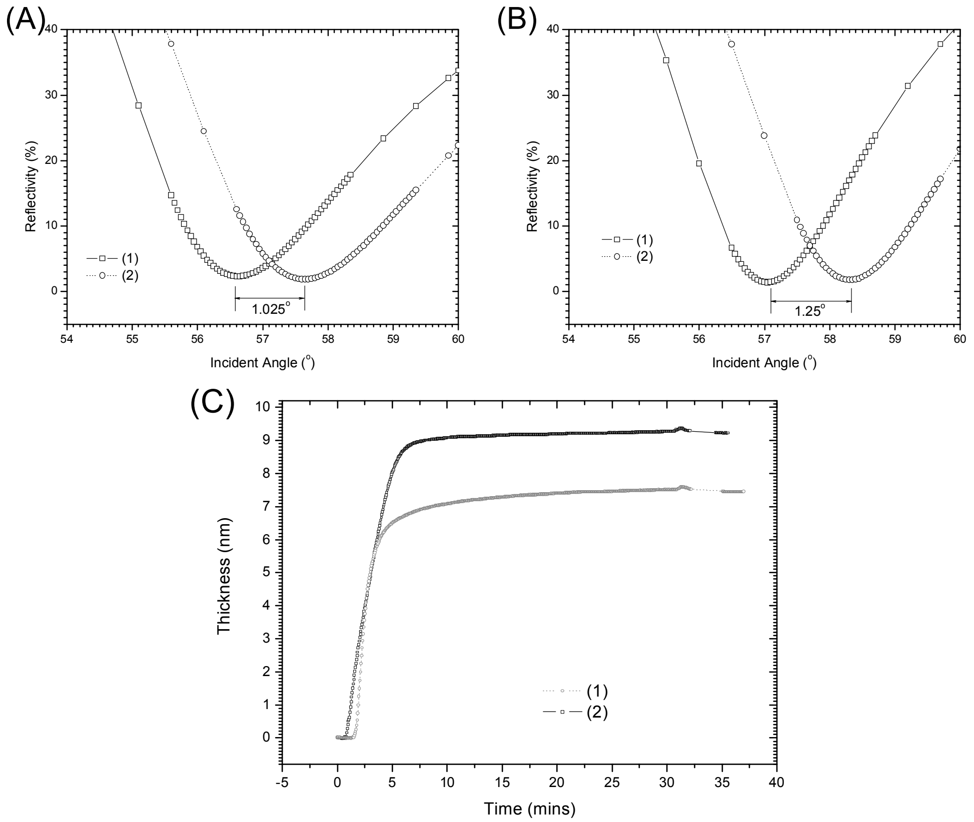

Figure 4.4: rSbpA-HT's recrystallization on Au and on SCWPs. (A) SPR scan curves before (1) and after (2) rSbpA-HT's recrystallization on gold. (B) SPR scan curves before (1) and after (2) rSbpA-HT's Recrystallization on SCWPs. (C) The kinetic measurements of rSbpA-HT's recrystallization on gold (1) and on SCWPs (2).

4.4 Grafting Experiments

Structural and permeability studies have shown that S-layer lattices are highly porous protein meshwork with pores occupying up to 70% of their surface[14]. It would be quite natural to estimate the advantages of fully using this high degree of structural regularity. Nanometer-scale phase separation in mixed composition self-assembled monolayers has been observed by many groups[71,72]. This surface heterogeneity phenomenon will impair the benefits of using mixed thiols, resulting in the steric hindrance problems during the following binding of other molecules on top of the self-assembled thiols. Efficient use the naturally ordered S-layer lattices structure would be one of the possible ways to reduce the influence of the phase segregation greatly.

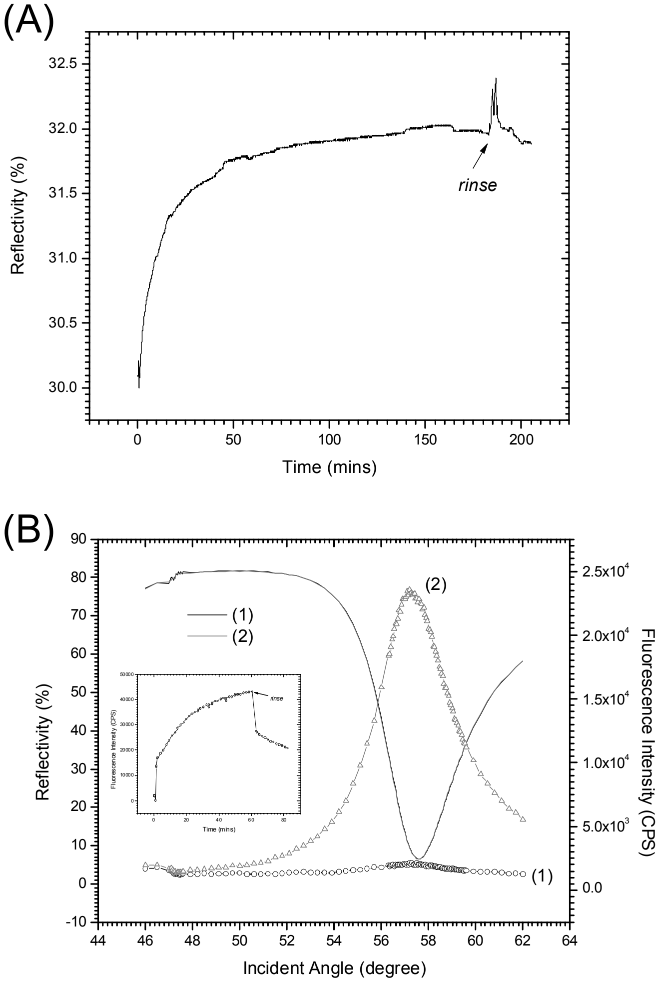

Figure 4.5: Grafting experiments. (A) Kinetic process about self assembly of thiolated 30mer P2 oligonucleotides. (B) SPFS scan curves before (1) and after (2) Cy5 labeled T1's binding. The inset shows the fluorescence kinetic measurement.

In order to prove this, grafting experiments have been made to self assemble thiolated 30mer oligonucleotides strands P2 into S-layer lattice pores after the completion of rSbpA's recrystallization onto gold. The self assembly process of thiolated P2 is shown in

Figure 4.5 (A), carried out in PBS buffer with the concentration of 1 µM. After that, 100 nM Cy5 labeled 15mer T1 prepared in PBS buffer was injected into the flow cell with the continuous flow rate of 3.6 ml/min. From the kinetic process characterized by the fluorescence channel which is plotted in the inset of Figure 4.5 (B), as well as the SPFS scan curves before T1's injection (1) and after the buffer rinse (2), the conclusion could be made that the DNA hybridization was not strong enough since the fluorescence intensity was only at 10^4 cps magnitude, at least 2 orders of magnitudes smaller than the signal obtained for streptavidin supported biotinylated P2 system[73]. Although this might be attributed to the quenching effect of chromophores to the metal surface due to the proximity, the most possible explanation should be the low hybridization efficiency. Since the oligonucleotide strands are randomly coiled (1.5 nm thickness[74]) and the rSbpA lattice shows a thickness of about 8 nm with pores in the lattice of only 4.5 nm width (cf. Table 4.1), a surface coupled oligonucleotide strand was not easily accessible by a complementary fluorescently labeled second strand against the steric hindrance effect. One possibility to overcome this is to choose other kinds of S-layer proteins with larger pores. This work is still in progress.

4.5 DNA Hybridization on S-layer-Streptavidin Fusion Proteins

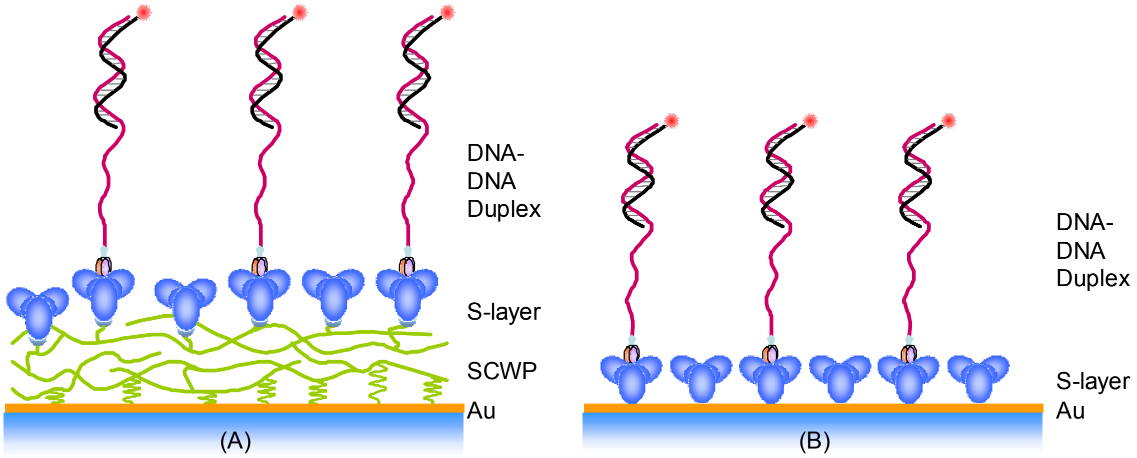

Figure 4.6: Schematic arrangement of S-layer supramolecular structures for DNA hybridization. (A) The mixture of S-layer proteins and S-layer-streptavidin fusion proteins constructed on top of SCWPs. (B) The mixture of S-layer proteins and S-layer-streptavidin fusion proteins directly recrystallized on a gold surface.

Although the grafting experiments did not fully demonstrate the expected advantages of the crystalline S-layer array in reducing of the surface heterogeneity phenomenon, streptavidin functionalized S-layer proteins still can be used as the supramolecular structures for DNA hybridization inspection for their highly ordered arrangement and the good separation of fluorescent chromophores from the metal surface. Figure 4.6 gives the schematic structure of an S-layer matrix used for DNA hybridization examination.

4.5.1 Instability Problem

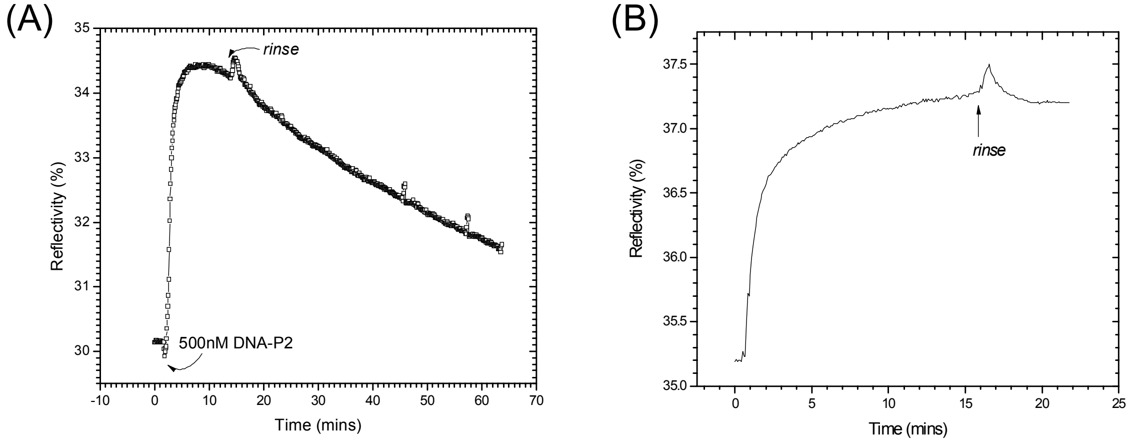

Figure 4.7: The influence of glutaraldehyde on the stability of SCWP anchored rSbsB-HT. (A) Without using glutaraldehyde, the reflectivity kept declining during the buffer rinse process after biotinylated P2's binding. (B) After treating with glutaraldehyde, rSbsB-HTs could not be pulled out from the surface, and the reflectivity signal maintained constant after the fresh buffer rinse.

It has been known that the affinity between SLH-motifs and their matching SCWPs is not so high[75]. Thus, the merit of less fluorescence quenching for the structure in Figure 4.6 (A) compared to the one in Figure 4.6 (B) will be impaired by a continuous loss of S-layer proteins in further coupling steps, which is clearly exhibited in Figure 4.7 (A). The persistent mass loss of the whole system can be observed during fresh buffer rinse after the binding of biotinylated DNA probes on SCWPs' supported rSbsB-HTs reached its equilibrium.

Glutaraldehyde has long been used in Prof. Uwe B. Sleytr's group[13,76] to cross-link S-layer proteins to obtain particularly stable composite structures. The mechanism behind this method is to connect amine-containing biomolecules to produce a compact network[77].

In our study, after using a 0.25% (w/v) glutaraldehyde solution prepare in PBS buffer for 15 minutes at room temperature, the subunits of S-layer proteins were fused together to form a whole lattice sheet on the surface, and could not be easily separated individually anymore (cf. Figure 4.7 (B)).

4.5.2 DNA Hybridization Kinetics Analysis on S-layer Fusion Proteins

A typical fluorescence response plot of DNA hybridization process including three kinds of mismatches on the same chip is shown in Figure 4.8. The catcher stands were bound to the SCWP supported rSbsB-HT layer via a biotin-group at the 5’ end of an additional 15mer of thymines used as spacers. The highly sensitive fluorescence intensity signal was then used to quantify the kinetics of binding and dissociation of different oligonucleotides exhibiting full complementarity to the catcher probes (MM0) or having one (MM1) or two mismatches (MM2) in the base sequence, respectively.

A detailed experimental protocol for hybridization was described elsewhere[78,79]. In general, the concentration of the probes was 500 nM, and the concentration of the targets was 100 nM. All samples were prepared in PBS buffer. The different kinetics behavior of the three types of binding processes, as well as the highly repeatable performance after regeneration with 50 mM NaOH solution for one minute each time, provided considerable evidence that such a supramolecular architecture is an ideal platform to monitor biomolecular interactions on the surface.

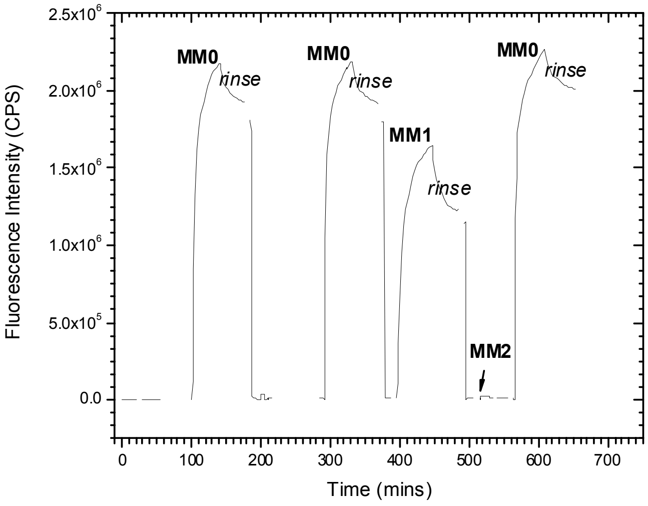

Figure 4.8: Different hybridization kinetics for different DNA targets characterized in fluorescence channel on the same SCWP supported rSbsB-HT chip.

The surface hybridization and the corresponding kinetic and equilibrium data were analyzed assuming a simple Langmuirian model for the interaction according to the methods presented in Section 2.3. The data obtained with a rSbpA-HT lattice directly recrystallized on the gold surface was compared with the results obtained for a biotin SAM ($\chi = 0.1$) supported streptavidin supramolecular structure.

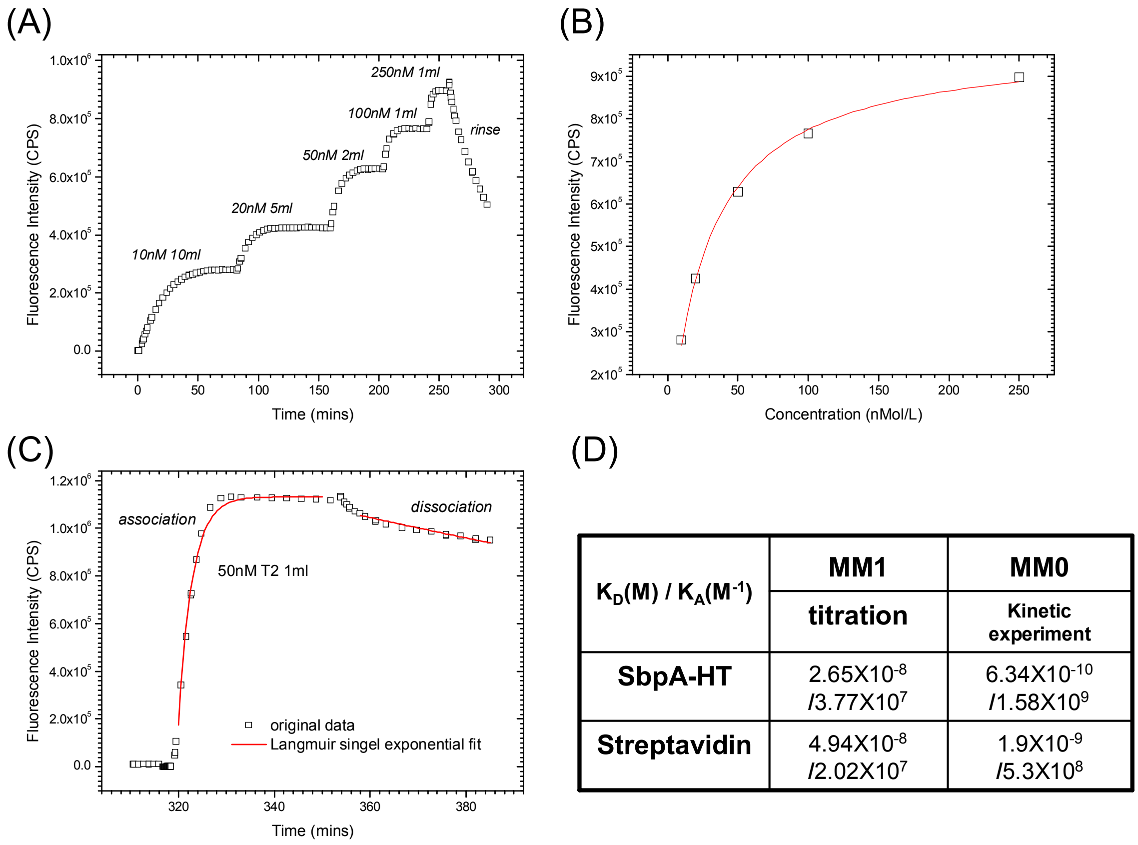

$K_D(M)$ / $K_A(M^{-1})$	**MM1**	**MM0**
	titration	**Kinetic experiment**
SbpA-HT	$2.65X10^{-8}$ $/3.77X10^{7}$	$6.34X10^{-10}$ $/1.58X10^{9}$
Streptavidin	$4.94X10^{-8}$ $/2.02X10^{7}$	$1.9X10^{-9}$ $/5.3X10^{8}$

Figure 4.9: MM1 and MM0 hybridizations on gold supported rSbpA-HT matrix for Langmuir adsorption model analysis. (A) The MM1 titration measurement with five target concentrations. (B) A plot showing the correlation between target concentrations and their corresponding saturation intensities, with a curve fitted to the Langmuir isotherm model. (C) The MM0 hybridization experiment which is matched with single exponential interaction controlled kinetics. (D) The comparisons between the affinity parameters got in rSbpA-HT matrix and on normal streptavidin surface.

As mentioned above, one way to elucidate the kinetic properties is to measure the association process and the dissociation process at a given target concentration to obtain k_{on} and k_{off} by a Langmuir simulation. Another method instead is to perform a titration experiment by stepwise increase of the target concentration to saturate the surface probe architecture. The titration experiment for MM1 hybridization taking place at the gold supported rSbpA-HT matrix characterized by fluorescence is plotted in Figure 4.9 (A), in which a series of DNA T1 solution from 10 nM to 250 nM was stepwise introduced into the loop with a circulation rate of 3.6 ml/min. The volume used for each concentration is also indicated. Note that the volume used for the lower concentration was larger in order to provide sufficient targets for the surface saturation. The fluorescence saturation intensity values were plotted as a function of the bulk concentrations of the targets (cf. Figure 4.9 (B)). The resulting plot is perfectly fitted to the Langmuir isotherm to obtain a dissociation equilibrium constant $K_D = 2.65\times10^{-8}$ M. On the other hand, for 50 nM DNA T2's binding (MM0) on gold supported rSbpA-HT surface, a single exponential kinetic fit (cf. Figure 4.9 (C)) was applied to yield the kinetic constants of $k_{on} = 1.13\times10^{5}$ $M^{-1}s^{-1}$ and $k_{off} = 7.2\times10^{-5}$ s^{-1}, subsequently the dissociation constant $K_D = 6.34\times10^{-10}$ M. The affinity parameters obtained here were comparable to those on a biotin SAM ($\chi = 0.1$) supported streptavidin matrix (cf. Figure 4.9 (D)).

4.5.3 LOD of DNA Hybridization on S-layer Fusion Proteins

The limit of detection (LOD), is one of the most important factors to judge the sensitivity of a biological or chemical analytical system. The LOD of DNA hybridization measurements based on S-layer fusion proteins matrix was also tested in our study.

4.5.3.1 Definition of LOD

In statistics, LOD is the minimum single result which, with a stated probability, can be distinguished from a suitable blank value. The limit defines the point at which the analysis becomes possible and this may be different from the lower limit of the determinable analytical range. The limit of detection, expressed as the concentration, c_L, or the quantity, q_L, is derived from the smallest measure, x_L, that can be detected with reasonable certainty for a given analytical procedure. The value of x_L is given by the equation:

$$x_L = \bar{x}_{bi} + ks_{bi} \qquad \textbf{--- 4.2}$$

where $\bar{x}_{bi}$ is the mean of the blank measures, s_{bi} is the standard deviation of the blank measures, and k is a numerical factor chosen according to the confidence level desired[80]. Usually k is set as 3 and LOD is called 3Sigma.

4.5.3.2 LOD of DNA Hybridization on Gold supported rSbpA-HTs

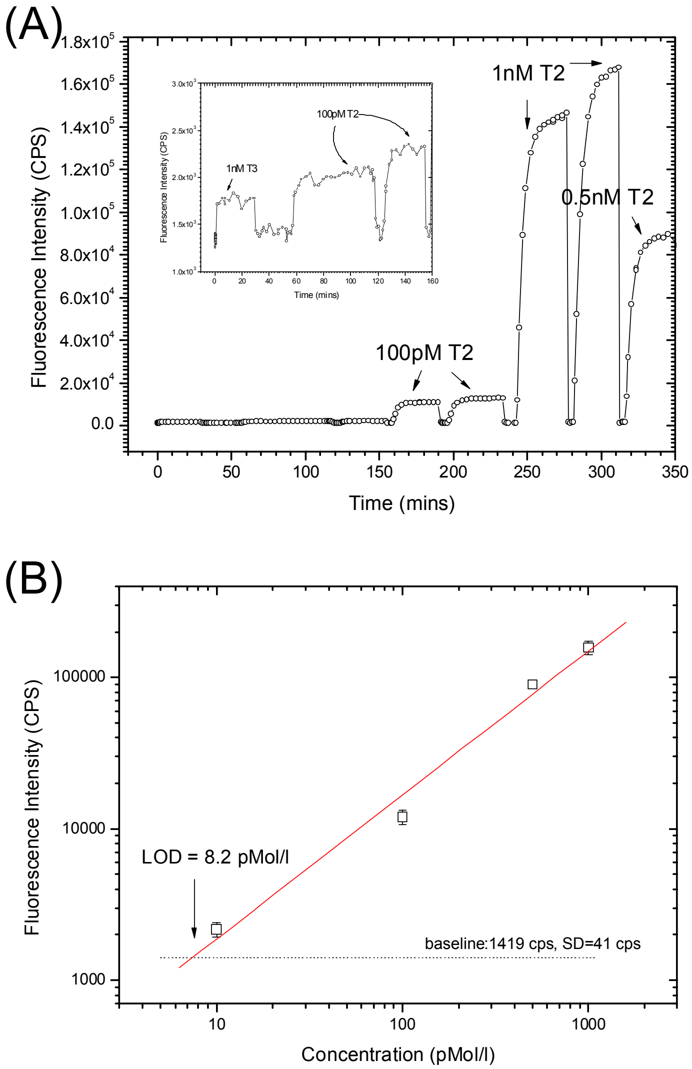

Figure 4.10: LOD test of MM0 hybridization on gold supported rSbpA-HT surface. (A) Kinetic fluorescence working curves acquired by injection a series of T2 solution with concentration from 10 pM to 1 nM. The inset shows the amplification of the beginning part of fluorescence response at low concentration samples injection. (B) Dose-response curve constructed by the final fluorescence intensity after 30 minutes of reaction versus the targets concentration.

The LOD of MM0 DNA hybridization achievable on gold supported rSbpA-HT layer was first measured. Recrystallization of rSbpA-HT on a gold surface and the functionalization with biotinylated P2 probes followed the aforementioned protocols. For every experimental injection, 900 µl T2 samples with the desired concentrations (10 pM, 100 pM, 500 pM, 1 nM) were prepared in PBST buffer. The sample was injected into the flow cell and circulated in the loop at a rate of 3.6 ml/min for 30 minutes. After that, the surface was regenerated with 50 mM NaOH solution followed by fresh buffer rinse for the next binding. The fluorescence intensity response before regeneration was selected for the dose-response plotting. Every concentration was repeated twice except 500 pM. Before MM0 hybridization, 900µl 1 nM T3 sample was introduced into the flow cell for 30 minutes, producing a fluorescence response less than that of 10 pM T2. Exchanging the T3 solution by PBST buffer abruptly leveled down the signal, indicating there was almost no non specific binding (NSB) of the targets. The kinetic fluorescence working curve is shown in Figure 4.10 (A) and the corresponding dose-response curve is plotted in Figure 4.10 (B) in a double-logarithmic graph. The linear fit line illustrates the excellent quality of the dose-response curve. Extrapolating the linear curve to the baseline level resulted in a theoretical detection limit of 8.2 pM. The baseline was attained by calculating an average value of fluorescence intensity response data for 30 minutes.

One advantage of recrystallization of rSbpA-HT on gold can be seen in the strong interactions between the inner surface of the S-layer proteins and gold, which is responsible the robust properties of the surface without any loss of fusion protein after regeneration (reflectivity channel data not shown). In fact, the S-layer proteins could not be removed from the gold even with ethanol or chaotropic agents like urea and GHCl[81]. The rSbpA-HT matrix has already shown superiority over streptavidin layer by showing less fluorescence quenching, because the average thickness of such S-layer protein monolayer is at least 8 nm (cf. table 4.1) while the thickness for biotin SAM plus streptavidin amounts to ca. 5.3 nm[47]. This advantage should become even more obvious if rSbpA-HT proteins self assemble on their SCWPs, resulting in a better distance separation of fluorophores from the metal surface. Therefore, the LOD of DNA hybridization occuring in SCWPs supported rSbpA-HT matrix is supposed to be smaller than that on gold supported rSbpA-HT layer.

4.5.3.3 LOD of DNA Hybridization on SCWPs supported rSbpA-HTs

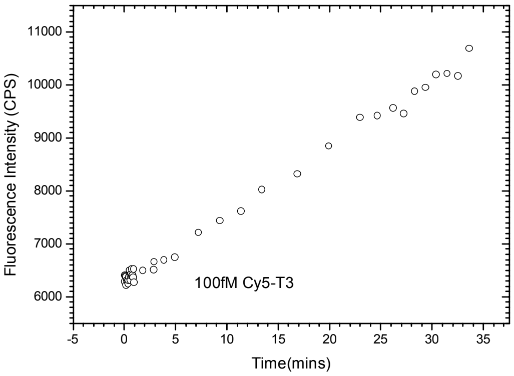

Figure 4.11: NSB of T3 on glutaraldehyde treated biotinylated P2 surface constructed on the top of SCWPs supported rSbpA-HT layer.

The self assembly of thiolated SCWPs and the further coupling of rSbpA-HTs, as well as the immobilization of biotinylated P2 were investigated following the statements above. 0.25% glutaraldehyde was routinely used for cross-linking of S-layer proteins before introducing P2. The non specific adsorption of MM2 targets was tested at the beginning of the hybridization studies. Unexpectedly, even 100 fM showed a strong non specific adsorption (cf. Figure 4.11) and the adsorbed targets could not be removed by 50 mM NaOH solution (data not shown). Since NSB has been checked on gold supported rSbpA-HTs already and there was no evidence of such adsorption, the abnormal signal most came from the cross-linking treatment by glutaraldehyde.

In Section 4.5.1, we have discussed the instability problem of S-layer proteins on SCWPs. But the utilization of glutaraldehyde resulted in strong NSB. The following protocol has to be adopted as a compromise in order to test the LOD of DNA hybridization on SCWPs supported rSbpA-HTs. The supramolecular structure of SCWPs, rSbpA-HT proteins and biotinylated P2 was built up first. Glutaraldehyde was not used this time. Usually at a relatively low analyte bulk concentration, the initial binding is under mass-transport control and the binding rate is constant and not related to the interaction affinity[82]. Thus, the slope of the binding is proportional to the active analyte concentration, which means we can take the slope of the linear part after each injection for the dose-response curve, not worrying about the regeneration. The kinetic working curve is shown in Figure 4.12

(A), and the amplification of the early part of the fluorescence working curve is shown in Figure 4.12 (B). A series of 1 ml T1 samples prepared in PBST buffer with concentrations of 1 pM, 10 pM, 100 pM, 500 pM and 1 nM were stepwise injected into the flow cell and circulated in the loop at a rate of 3.6 ml/min until the linearity of the binding curve has changed. Note that the reflectivity signal keep declining due to the lack of cross-linking. Before the concentration analysis, 1 ml 1 nM T3 solution was introduced into the flow cell in order to test NSB on the surface. Fresh PBST buffer rinse after 20 minutes of circulation almost flatted the signal to the original background level, indicating a good impurities resistance of the S-layer surface without using glutaraldehyde. On the same chip, the "blank" injections only with PBST buffer before the concentration analysis were repeated twice. Two slopes were obtained by linear fit, and analyzed statistically to quantify the baseline deviation (cf. Figure 4.12 (C)). The slope obtained from the linear fit for every mass-transport kinetic part was plotted versus the targets concentration in Figure 4.12 (D) in a double-logarithmic graph. The linear fit line illustrates a theoretical LOD of 1.57 pM, better than the LOD value obtained on gold supported rSbpA-HTs.

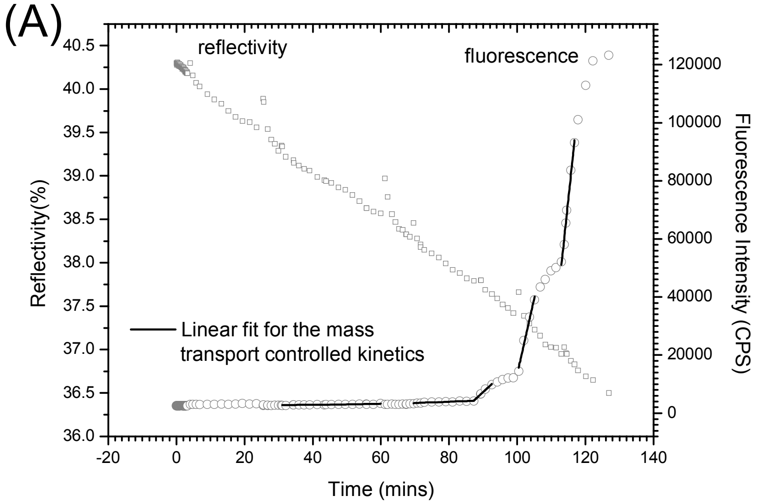

Figure 4.12: LOD test of MM1 hybridization on SCWPs supported rSbpA-HT surface. (A) Kinetic working curves acquired by injection a series of T1 solution with concentration from 1 pM to 1 nM. (B) The amplification of data recorded by fluorescence channel for the response at low concentration samples injection. (C) Fluorescence response of PBST buffer injection as the blank. (D) Dose-response curve constructed by the slope of fluorescence intensity linear increasing part versus the targets concentration.

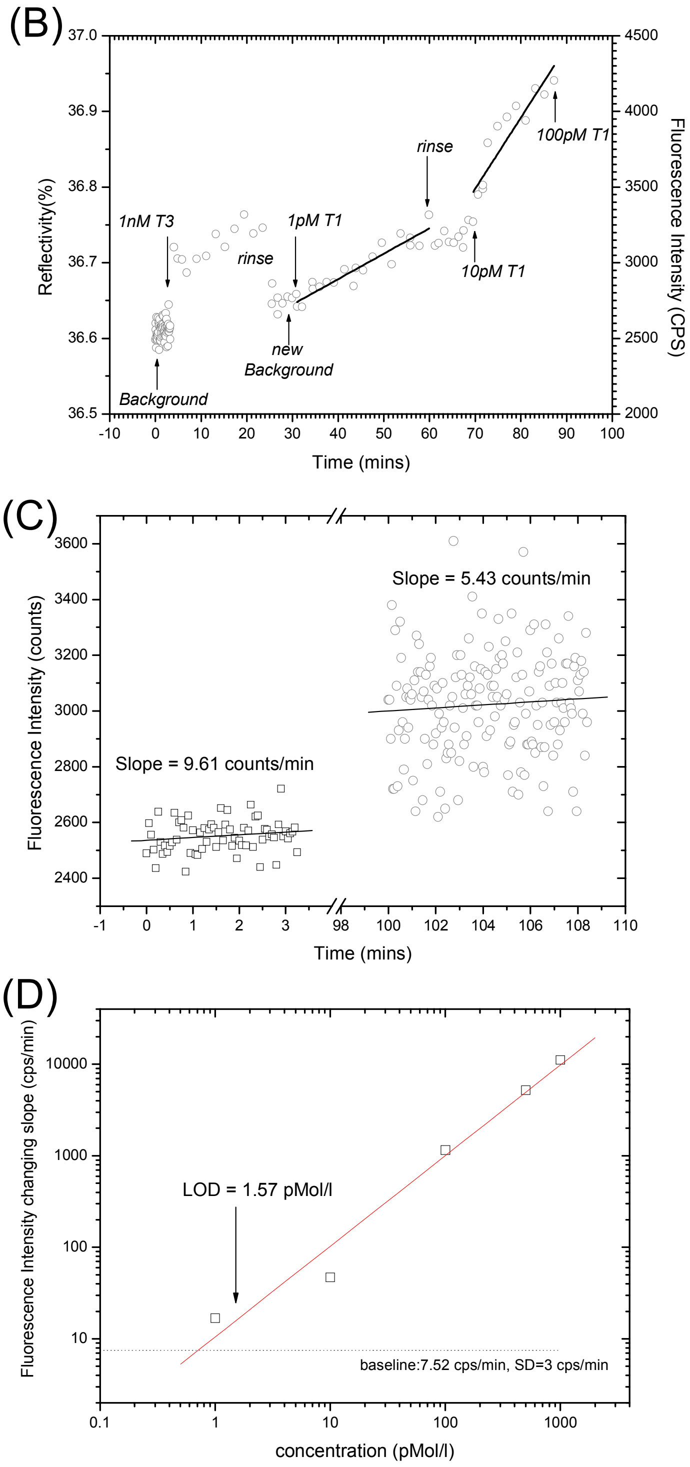

Figure 4.12: (continued)

As expected, the sensitivity for DNA hybridization measurements characterized by SPFS on a SCWPs supported S-layer surface is higher than on a gold supported S-layer surface due to the reduced fluorescence quenching. However, such advantage is impaired by the instability problem resulting from the low affinity between the S-layer proteins and the SCWPs. Cross-linking via glutaraldehyde could improve the stability of S-layer proteins, however, generate a new issue, *i.e.* NSB, which might be avoided by blocking the active sites before targets injection or application of other suitable cross-linker.

4.6 Immobilization of LHCII on S-layer Fusion Proteins

As discussed above, the self assembly of the S-layer fusion proteins (rSbpA-HT or rSbsB-HT) was exploited to arrange chains of core streptavidin in defined order and orientation in a two-dimensional protein crystal. Owing to the versatile applications of the streptavidin-biotin interaction as a biomolecular coupling system, the chimeric S-layer was also designed to serve as a compatible patterning element for the immobilization of biotinylated LHCII complexes (cf. Chapter 6).

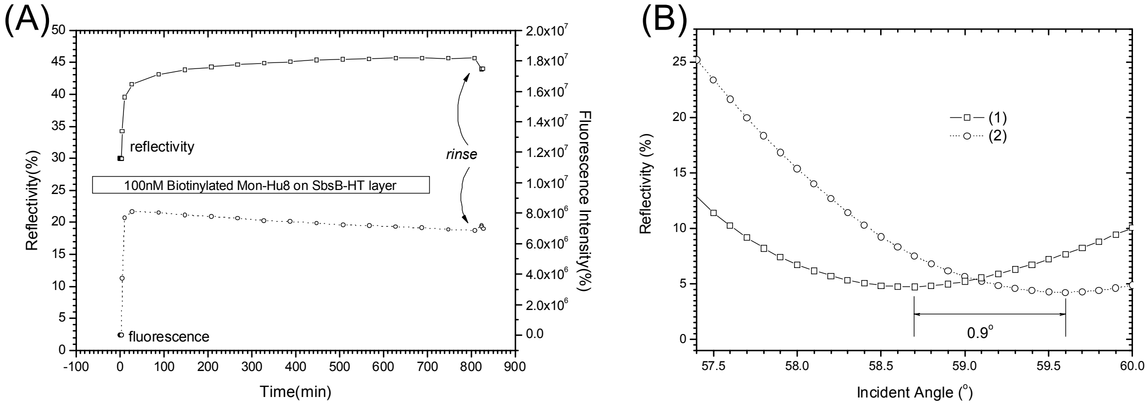

Figure 4.13: The immobilization of biotinylated Hu8 monomers on SCWPs supported rSbsB-HT layer. (A) Kinetic working curves. (B) SPR angular scan curves before the sample injection (1) and after the fresh buffer rinse (2).

As shown in Figure 4.13, after surface functionalization with SCWPs and rSbsB-HTs, 100 nM biotinylated Hu8 monomers prepared in eluent buffer (0.01 M Hepes, pH 7.4, 0.15 M NaCl, 50 μM EDTA, 0.005% P-20, 0.1% (w/v) DM) was injected into the flow cell and still for ca. 800 minutes. The final angular shift was 0.9° (cf. Figure 4.13 (B)), equal to a coverage of S-layer by a LHCII monolayer of 66% (cf. Section 6.8), more than that on a streptavidin layer (cf. Table 6.3). This is consistent with the conclusion obtained in solution where rSbpA-HTs showed an even higher biotin binding capacity in comparison to free streptavidin[67]. Moreover, the fluorescence intensity was still about 80% of its original peak value after 13 hours of incubation, suggesting a good biological activity maintained on the S-layer fusion protein layer (cf. Figure 4.13 (A)).

4.7 Conclusion

S-layers are a simple self assembly system leading to monomolecular isoporous protein lattices with repetitive physicochemical properties down to the nanometer scale. Incorporation of peptide stretches representing functional domains of other proteins by recombinant DNA technologies will broaden the application potential of S-layers and could lead to the development of new biosensor systems.

By applying surface plasmon spectroscopy, the recrystallization behaviors of S-layer proteins or S-layer-streptavidin fusion proteins on gold or secondary cell wall polymers were recorded. The optical thicknesses and the surface densities were calculated for different protein layers. Although grafting experiments did not fully confirm the expected advantages of the ordered lattice structure of the S-layer proteins, in DNA hybridization tests performed in order to discriminate different mismatches, recombinant S-layer-streptavidin fusion protein matrices successfully showed their potential in exploitation of new microarray platforms. Moreover, secondary cell wall polymers coated gold chips, covered with more controlled and oriented assembly of S-layer fusion proteins, represented an even more sensitive fluorescence testing platform. Finally, S-layer fusion proteins as the matrix for LHCIIs' immobilization strongly demonstrate superiority over normal streptavidin layers, proving the possibility of utilizing them as a new strategy for biomolecular coupling.

5 SPFS HCG IMMUNOASSAY

5.1 Introduction

Human chorionic gonadotropin (hCG) is a glycoprotein hormone secreted by the trophoblastic cells of the placenta during pregnancy. It is a member of the glycoprotein hormone family which includes luteinizing hormone (LH), follicle-stimulating hormone (FSH), and thyroid-stimulating hormone (TSH). Its function is to maintain the corpus luteum and stimulate steroid secretion from the ovary in the beginning stages of gestation. Apart from its physiological action, hCG is found in pathological cases such as choriocarcinoma, hydatidiform mole and testicular cancer[83].

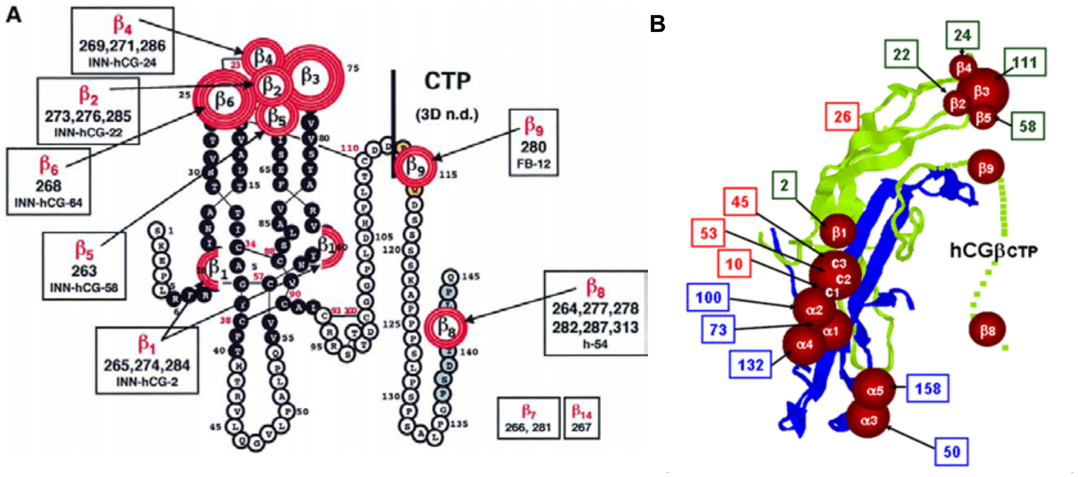

Figure 5.1: Representation of the structure of hCG. (A)Assignment of epitopes to the amino acids sequence structure of hCG[84]. (B) 3-D localization of epitopes on hCG α subunit (green), hCG β subunit (blue) and hCG dimer only (red)[85].

The molecular weight of hCG is approximately 37.9 kDa based on the native form, which contains 2 subunits (cf. Figure 5.1). The α subunit (14.9 kDa) contains 92 amino acid residues and five disulphide bridges, with a dimension of 6 nm × 2.5 nm × 1.5 nm, and the β subunit (23 kDa) contains 145 amino acid residues and six disulphide bridges, with a dimension of 6 nm × 2.5nm × 2 nm[86]. The two subunits are stabilized by three disulphide bonds forming a cystine knot. They are associated in an anti-parallel fashion and form the biologically active αβ-heterodimer termed hCG[84].

Quantitative determinations of hCG and hCG derivatives in serum or urine are important in the diagnosis and monitoring of pregnancies and hCG-secreting malignancies, and in testing for Down's syndrome. For example, hCG is produced in large amounts by the trophoblastic cells and is usually detectable in serum about 7-9 days after conception when implantation occurs (cf. Table 5.1). This gives high requirements to the specificity and the sensitivity of the detection methods.

1st week	10 – 30
2nd week	30 - 100
3rd week	100 – 1,000
4th week	1,000 – 10,000
2nd & 3rd month	30,000 – 100,000
2nd trimester	10,000 – 30,000
3rd trimester	5,000 – 15,000

Table 5.1: Expected values for hCG levels (3rd IS 75/537) during normal pregnancy (in mIU/ml)[87].

Today, the clinically available hCG detection methods are mainly based on immunoassays. Immunoassays use antibodies or antibody-related reagents for the determination of sample analytes[88]. The selectivity of the ligand-binding of antibodies allows these biomolecules to be employed in analytical methods that are highly specific even in complex biological matrices, such as blood, plasma, or urine. By combining the selectivity of antibody–analyte interactions with the vast array of antibodies preformed during immunization processes of host animals and the availability of numerous readily detectable labels, immunoassays can be designed for a wide variety of analytes while with extraordinarily low detection limits as well as relatively low cost. In general, immunoassays are categorized on the basis of the types of labels that they employed and divided into radioimmunoassay, enzyme immunoassays, fluorescence immunoassays, chemiluminescence immunoassays and so on.

As the most avant-garde concept in biological science, biosensors are analytical devices that integrate a biological element on a solid-state surface, enabling a reversible bio-specific interaction with the analyte, and a signal transducer[15]. If antibodies or antibody fragments are applied as biological element, the device is called an immunosensor. In contrast to immunoassays, modern transducer technology enables the label-free quantification detection of the immune complex.

Among other kinds of optical immunosensor systems, SPR is the most popular one not only in the scientific realm but also in the commercial world. Early in 1993, Spinke and co-workers had used SPR as the tool to characterize the formation of the supramolecular structure: biotin SAM, streptavidin, biotinylated Fab, hCG and monoclonal antibody, which was of relevance to immunoassays for pregnancy testing, and got a detection limit of approximately 1×10^{-8} M[33].

SPFS has the ability of simultaneously monitoring the interfacial refractive index changes and the fluorescence signals in real time. The surface enhanced fluorescence signal greatly upgrades the possibility of detection of trace substances in solution, which has been confirmed by the work of Yu[89]. In this chapter, we will present the hCG immunosensors investigation based on SPFS technology, including surface antibodies orientation study, affinity constants determination of different antibody-antigen systems, LOD measurements *etc.*.

5.2 Materials

hCG was purchased from Sigma-Aldrich with the purity of 14242 IU/mg (Product Nr. C-0434) and 6130 IU/mg (Product Nr. CG-10) respectively. The latter was only for Alexa Fluor 647 labeling, which was kindly done by Roche Diagnostics GmbH with a dye-to-protein molar ratio (D/P) of 8.9.

Mono-Biotinylated anti-hCG Fab (abbreviated as Bio-Fab), which was also kindly provided by Roche Diagnostics GmbH, is coming from the Fab fragment of M-1F7.9 (isotype IgG1-κ), directed to the epitope c2 on the intact αβ-heterodimer (cf. Figure 5.1).

Biotinylated anti-α-hCG IgG (abbreviated as Bio-α-IgG) and Alexa Fluor 647 labeled anti-α-hCG IgG (abbreviated as AF-α-IgG) were from Dr. Toby Jenkins' group in University of Bath, United Kingdom. The anti-α-hCG IgG mentioned here interacts with the region of α1α2α4 epitopes, which localizes between amino acids residues 13-22 in the hCG α subunit (cf. Figure 5.1). Biotinylated anti-β-hCG IgG (abbreviated as Bio-β-IgG) and Alexa Fluor 647 labeled anti-β-hCG IgG (abbreviated as AF-β-IgG) were also from Dr. Toby Jenkins' group. The anti-β-hCG IgG mentioned here interacts with the region of β2-β6 epitopes, which has relations with residues on the tip of both short β-hairpin loops 1 and 3 (cf. Figure 5.1). The biotinylation process and fluorescence labeling process were kindly completed by Margarida Vareiro, PhD student in Dr. Toby Jenkins' group, using Biotinamidocaproate N-hydroxysuccinimide ester from Sigma-Aldrich and Alexa Fluor 647 monoclonal antibody labeling kit from Molecular Probes respectively.

Tween®20 was from USB Corportation. Glycine was from Merck. Hydrochloric acid (HCl), phosphate buffered saline (PBS) tablets, sodium dodecyl sulfate (SDS) were purchased from Sigma-Aldrich. Streptavidin was kindly provided by Roche Diagnostics GmbH. All protein solutions were prepared in PBST buffer (0.01M phosphate buffer, 0.0027M potassium chloride and 0.137M sodium chloride, pH 7.4, 0.05% (v/v) Tween®20) unless otherwise stated.

All SPFS experiments were done at a circulation rate of 3.6 ml/min under the excitation of HeNe laser.

5.3 Appropriate Supramolecular Structures for hCG Detection

Despite an overwhelming number of papers in the field of immunosensors study, there are only a few commercial applications in clinical diagnostics. The reasons are, in part, unresolved fundamental questions relating to immobilization, orientation, and specific properties of the antibodies or antibody-related reagents on the transducer surface. As prerequisites for practical examinations, such immunosensors should firstly be simple and "rugged" for the measurements of analytes[15]. Secondly, the immobilization of antibodies should have an optimum density and adjusted but not random orientation. Finally, the antibody-antigen interaction on the sensor-coated surface is reversible, which means there should be an efficient regeneration way.

5.3.1 Biotin SAM Supported Streptavidin Structure

The streptavidin-biotin (or avidin-biotin) complex represents the highest affinity non-covalent interaction in nature. The affinity constant of 2.5×10^{13} M^{-1} between streptavidin and biotin[90] and the fact that biotin is able to be linked to almost any biomolecule make streptavidin and biotin a universal coupling system in biotechnology. On the other hand, formation of SAMs is usually the primary choice for surface modification on gold or silver surface (cf. Section 3.2.2), which is necessary in surface plasmon resonance technique. Therefore, the combination of streptavidin-biotin interaction and SAM structure should be one of the simplest and most robust fabrication strategies for immunosensors investigation.

The use of SAMs for the optimization of surface functionalization for molecular recognition process has been fully investigated by Spinke *et al.*[49] and the conclusion has been made that the choice of an appropriate biotin-containing molecule, with a spacer segment, and the dilution of this molecule within the monolayer by hydroxylthiols (the molar ratio of biotin thiol $\chi = 0.1$ in the mixed thiols solution), allows optimization of the binding properties of the monolayer – nonspecific interactions between streptavidin and the surface are below detection limit, while specific binding between the streptavidin and biotin groups can be maximized.

Surface Chemisty (Biotin SAM)	**SA's binding (angular shift)**	**Bio-β-IgG's binding (angular shift)**	**hCG's binding (angular shift)**	**Binding stoichiometry of IgG/SA**	**Binding stoichiometry of hCG/IgG**
χ=0.1	0.45°	0.45°	0.025°	1:2.6	1:4.6
χ=0.01	0.35°	0.3°	0.175°	1:3	2.2:1

Table 5.2: Comparison of two kinds of biotin SAM surfaces about hCG immobilization.

However, the mass change about the coupling of hCG on Bio-β-IgG surface on the top of above structure (cf. Table 5.2) only produced a SPR angular shift of 0.025°, slightly higher than the noise range. Two reasons were suggested to explain such low degree of binding. First, the size difference between one IgG molecule (14 nm × 10 nm × 5 nm)[91] and one streptavidin molecule (4.5 nm × 4.5 nm × 5.3 nm)[47] can not ignored. The steric hindrance caused by the even bigger dimension of the antigens held antibody (situation (1) in Figure 5.2 (A)) will greatly obstruct the following binding of hCG on its neighboring antibody (situation (2) in Figure 5.2 (A)). Second, the randomly distributed biotin labels in the IgG molecule might place on label near the epitope recognition sites, or the span of two arms in the antibody (10 nm) is just big enough to allow the IgG molecule to grasp two neighboring streptavidin monomer chains through a "greedy" manner, both of which will bate this antibody's antigen coupling ability (situation (3) in Figure 5.2 (A)). Thus, it is natural to conclude that a further dilution of biotin thiol in the SAM, followed by a reduced binding of streptavidin, will decrease the occurrence of the above situations while it increases the chances of hCG's access to antibodies. This is clearly reflected in Table 5.2, where the SPR angular shift came from hCG's coupling on biotin SAM χ = 0.01 surface was higher than that on a biotin SAM χ = 0.1 surface, and the stoichiometry of hCG/Bio-β-IgG was close to 2 (the small difference may come from the experimental error), which means almost each arm of one IgG molecule has grasped one hCG molecule. It is obvious that a continuous dilution of biotin thiol in the SAM will maintain the "avidity" property of the antibody to antigens, but the total number of the coupling antibodies will decrease concomitantly because of the reducing of streptavidin anchoring capacity on the surface. In principle, there should be an optimum point χ_{max} where the maximum binding of hCG can be attained. Further investigations are needed to find out this point.

In the sequent work of Spinke *et al.*[33], they figured out a better supramolecular structure for hCG immunoassay on the surface. Instead of using the whole antibody, biotinylated Fab fragments of anti-hCG IgG were employed. This Fab fragment is mono-biotinylation in the hinge region to ensure the proper orientation of the fragment on the surface with the binding site facing away from the surface. Furthermore, the size of the Fab fragment is only 5 nm × 7 nm × 4 nm[92], comparable with one streptavidin molecule. Therefore, the difficulties in using the whole antibody do not exist and the χ = 0.1 biotin SAM surface can be used again. This biomolecular interaction structure is schematic drawn in Figure 5.2 (B).

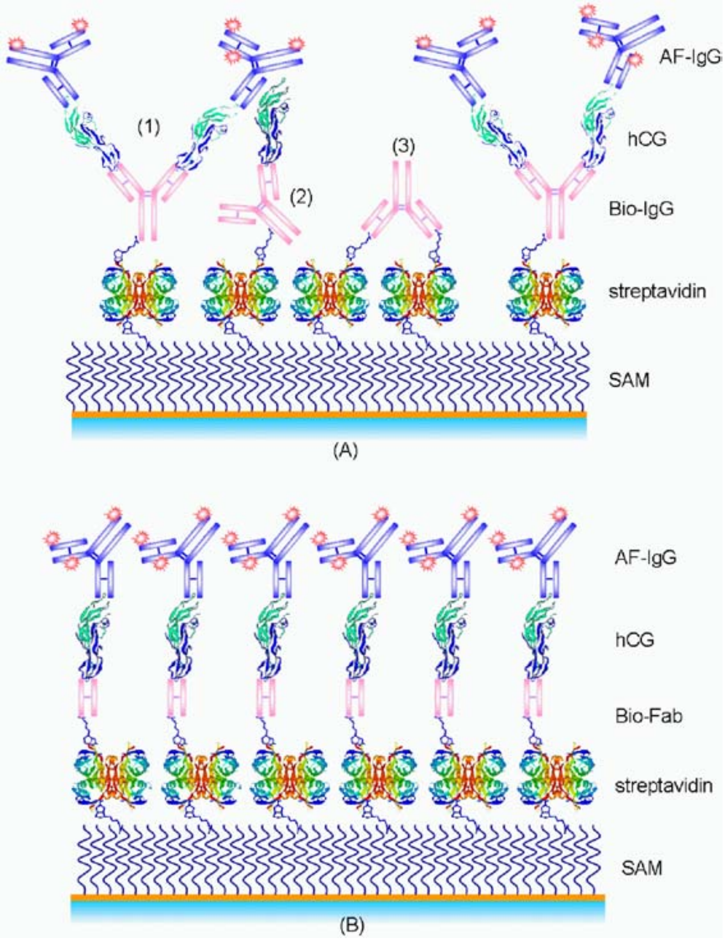

Figure 5.2: Schemes of different supramolecular structures for hCG detection. (A) Biotinylated antibody/hCG/AF labeled antibody structure. (B) Biotinylated Fab/hCG/AF labeled antibody structure.

5.3.2 Finding Appropriate Regeneration Conditions

In order to reuse the sensor chip surface, the analyte must be removed, but the ligand must stay intact, which is called regeneration procedure. The most frequent method used, is to inject a low pH-buffer such as 10 mM Glycine with pH 1.5-2.5[93]. It works probably because most proteins become partly unfolded and positively charged at low pH. The protein binding sites will repel each other and the unfolding will bring the molecules further apart[93]. Other procedures use high pH, high salt or specific chemicals to break the interaction. Sodium dodecyl sulfate (SDS), act as anionic detergent and a denaturing reagent, is able to break the hydrogen bonds between different molecules, thereby to regenerate the surface. The regeneration procedure has to be evaluated empirically because the combination of physical forces responsible for the binding are often unknown, and the regeneration conditions must not cause irreversible damage to the ligand. In this study, both Glycine-HCl buffer (10mM, pH 1.75) and SDS (0.5%) were used to test the influence to the surface. The recipes of both regeneration buffers were based on Biacore's protocols[94].

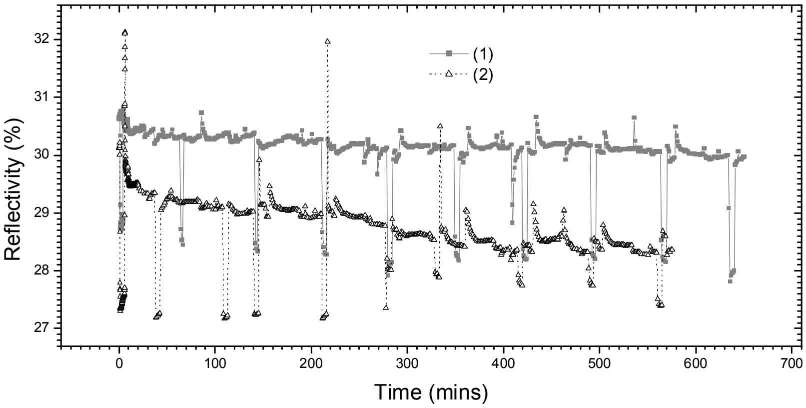

Figure 5.3: Reflectivity baselines comparison of Bio-β-IgG surface after regeneration with (1)10mM Glycine-HCl, pH 1.75, or (2) 0.5% SDS. The regenerations were performed in the intervals.

As shown in Figure 5.3, after the construction of a supramolecular structure of streptavidin/Biotin-β-IgG on a biotin SAM ($\chi = 0.1$) surface, a pulse injection of the regeneration buffer for 5 minutes was intended to strip off the loosely bound molecules. Binding of hCG and AF-α-IgG was initiated next, followed by a 5 minutes regeneration process. Such binding and regeneration cycles were repeated at least 10 times. The baseline of the solid line (Glycine regeneration) is more stable than the dot line (SDS regeneration), which might be attributed to the less offensive properties of Glycine buffer to this biomolecular matrix. Therefore, the Glycine buffer was chosen as the default regeneration buffer in all experiments of this chapter.

5.4 Affinity Determination

As a prerequisite for the design of the appropriate epitopes combination for hCG measurement in clinical applications, the affinity between different antibodies and their corresponding epitopes should be studied first.

5.4.1 Standard Protocol

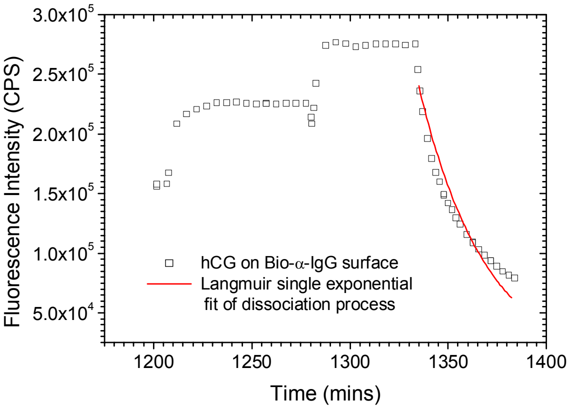

Figure 5.4: Kinetic fluorescence working curve of AF-hCG on Bio-α-IgG surface.

The protocol for all affinity determination experiments was standardized, using a series of AF-hCG solutions to saturate the surface bound antibodies, recording the data in the fluorescence channel for Langmuir isotherm simulations. Only the fluorescence signals were used taking into consideration that the SPR angular shift resulting from hCG coupling on the biotinylated IgG matrix (constructed on a biotin SAM ($\chi = 0.1$) surface supported streptavidin layer) was not strong enough for a reflectivity kinetics analysis (cf. Table 5.2). The titration method was chosen instead of interaction controlled kinetics simulation (cf. Section 2.3) because it was hard to apply a single-exponential Langmuir fit to all hCG/antibody interactions (cf. Figure 5.4). In addition, only $\chi = 0.1$ biotin SAM surfaces were adopted due to the following concerns. As presented in Table 5.2, although the mass change resulting from the Bio-β-IgG coupling on $\chi = 0.1$ biotin SAM surface is bigger than on $\chi = 0.01$ biotin SAM surface, the efficient hCG anchoring sites are less because of the steric hindrance. However, the decreasing of active surface ligand density will reduce the influence of mass-transport controlled kinetics, shorten thus the reaction time to reach equilibrium[95] (cf. Section 2.3). This is especially beneficial in high affinity biomolecular interaction titration experiment, where the surface saturation needs to be completed even at extremely low concentrations. As shown in the kinetic fluorescence working curve presented in Figure 5.5 (B), even on a $\chi = 0.1$ biotin SAM surface, it took about 50 hours from the sample injection to equilibrium for the lowest concentration (13.6 pM).

5.4.2 Results and Discussion

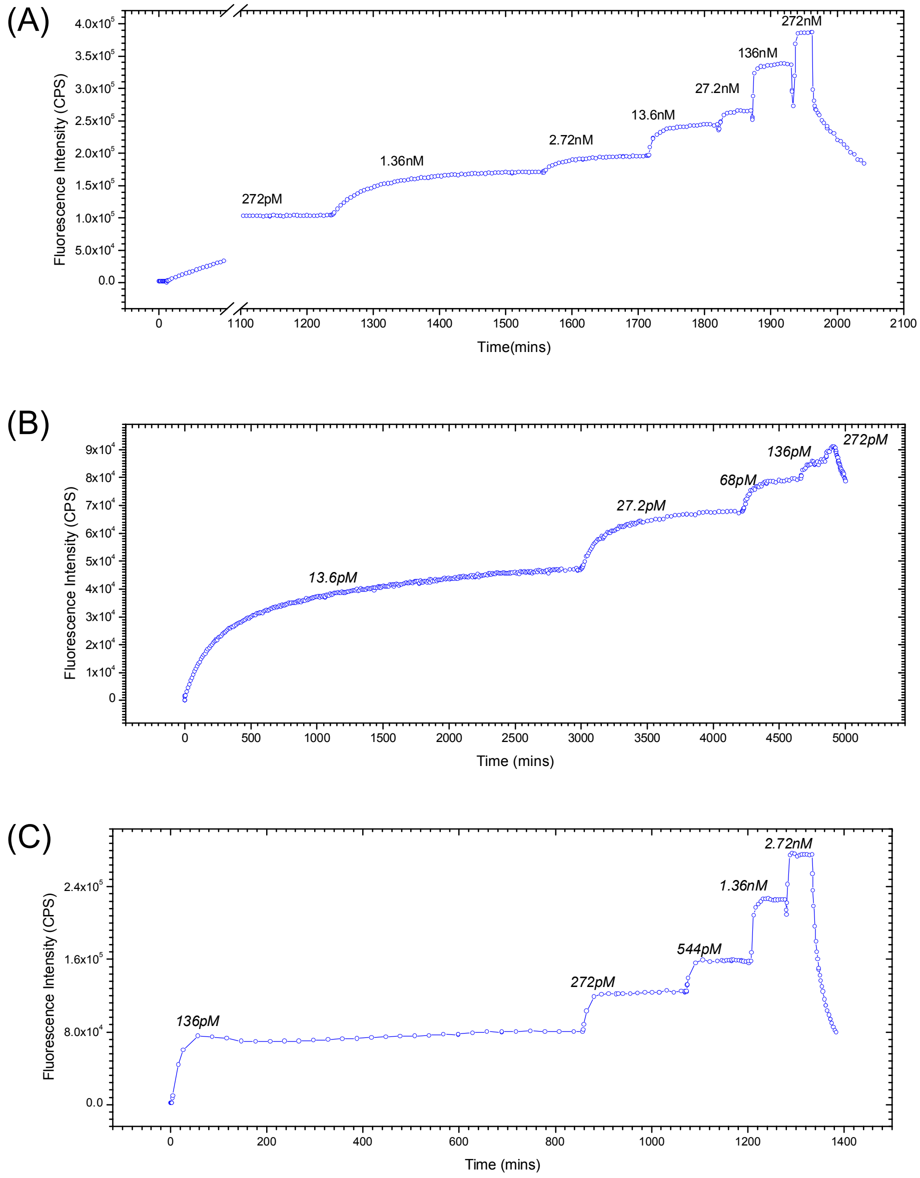

Figure 5.5: Concentration titration experiments on different surfaces and corresponding linearized versions of the Langmuir isotherm simulations. (A) Bio-Fab surface. (B) Bio-β-IgG surface. (C) Bio-α-IgG surface.

At first, a 500 nM streptavidin solution in PBS buffer was brought in contact with the biotin $\chi = 0.1$ surface for about 20 minutes until an association equilibrium was reached. After an SPR angular scan, PBS buffer was replaced by PBST buffer. Then a 500 nM biotinylated antibody solution prepared in PBST buffer was injected into the flow cell (Bio-Fab for Figure 5.5 (A), Bio-β-IgG for Figure 5.5 (B), Bio-α-IgG for Figure 5.5 (C)), and circulated for about 30 minutes in the loop. Finally, by a stepwise increase of the concentration of the AF-hCG solution in PBST buffer, different surface saturation levels from low to high were achieved expressed as different fluorescence intensity levels (cf. Figure 5.5). The time needed to reach the new equilibrium coverage became shorter as the concentration increased. A plot of concentration/fluorescence intensity as a function of concentration yields a straight line which is the linearized version of Langmuir isotherm simulation, from which the affinity constant can be deduced (cf. Section 2.3). These plots together with their linear regressions are shown in Figure 5.5 (continued). Several interesting features are worthwhile to be pointed out.

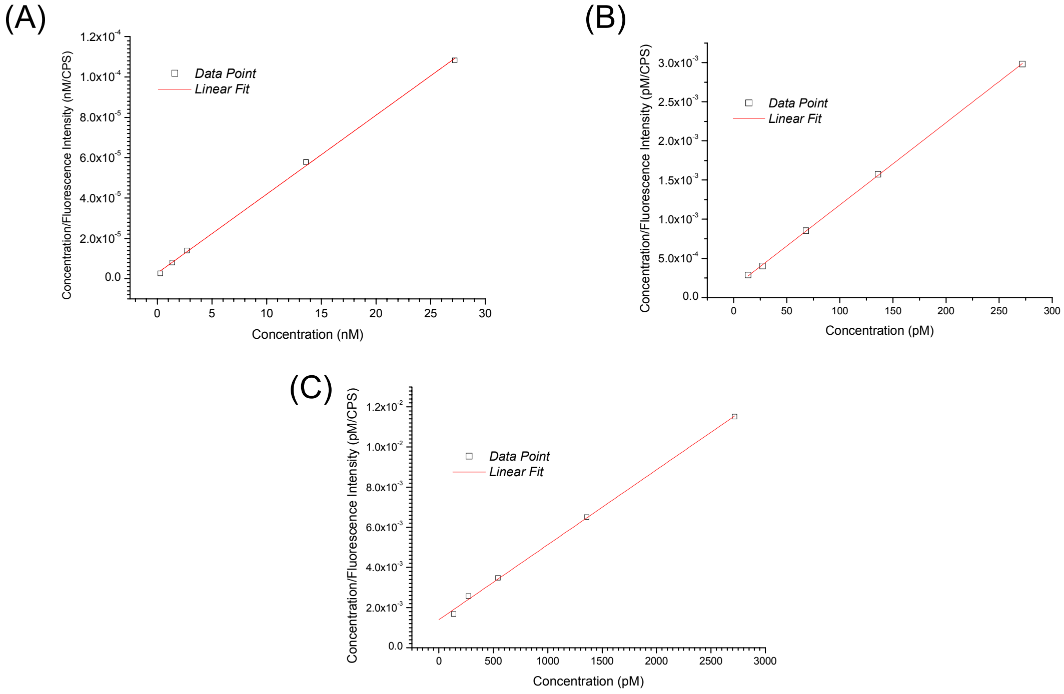

Figure 5.5 (continued)

Firstly, the affinity parameters obtained through the fluorescence concentration titration methods are shown in Table 5.3. Taking the hCG/bio-Fab (M-1F7.9) system as an example, one can see that the affinity measured is quite similar to the result from the literature[84], which was the estimated affinity between M-1F7.9 and ^{125}I-hCG. Interestingly, these values are about a factor of 2 different with the label-free determination via a Biacore instrument completed by Roche Diagnostics GmbH. Thus, this small difference may be mostly attributed to the labels.

Affinity Constant (M^{-1})	hCG/M-1F7.9	hCG/Bio-β-IgG	hCG/Bio-α-IgG
Concentration titration	1.41×10^{9} M^{-1}	7.78×10^{10} M^{-1}	2.67×10^{9} M^{-1}
Biacore (by Roche GmbH)	$3.9\text{-}4.8\times10^{9}$ M^{-1}		
Literature	2.1×10^{9} M^{-1}		

Table 5.3: Affinity parameters obtained for different systems.

Secondly, due to the high labeling efficiency (D/P = 8.9), the fluorescence contribution from the evanescent tail in AF-hCG solution was very strong, which resulted in an obvious signal deviation in the high concentration injection (cf. 272 nM in Figure 5.5 (B)). Therefore normally 2 ml PBST buffer was used to rinse the flow cell after the equilibrium reaching, and the first data point after rinse was taken as the saturation signal.

Finally, for the concentration titration, the number of AF-hCG molecules for each injection was supposed to saturate all the binding sites on the surface. A rough estimation of hCG binding sites on Bio-β-IgG surface is shown in Equation 5.1, where "SA" is the abbreviation of streptavidin.

$$AF-hCG_{number} = \frac{Area_{flowcell}}{Area_{SA}} \times SurfaceCoverage_{SA} \times stoichiometry_{IgG/SA} \times stoichiometry_{hCG/IgG}$$

--- 5.1

Knowing that the flow cell has a circular surface with a diameter of 3 mm, streptavidin has a surface area of 4.5 nm × 5.3 nm, the surface coverage of streptavidin is 53%[47], the stoichiometry of Bio-β-IgG/SA is 1:2.6, the stoichiometry of hCG/Bio-β-IgG is 1:4.6 (cf. Table 5.2), we can calculate that the number to saturate the surface should be 0.1 pMol. Considering about the non-specific adsorption in the circulation system, the number should be 9 times higher, equal to 1 pMol, which means for the lowest concentration injected in Figure 5.5 (B) (13.6pM), at least 100 ml solution need to be used.

5.5 Sandwich Assays

5.5.1 ELISA Introduction

ELISA (the acronym stands for Enzyme Linked ImmunoSorbent Assays) or EIA (Enzyme ImmunoAssay) assays, methods for determination of substances such as peptides, proteins, antibodies and hormones, in which a crucial element of the detection is an antigen-antibody interaction, was first described by Eva Engvall, *et al.*[96]. A key feature in all ELISAs is the fact that one of the reactants is labeled with an enzyme. The most commonly used enzymes are horseradish peroxidase (HRP) and alkaline phosphatase (AP). There are three major types of ELISA methods, which are illustrated in Figure 5.6 (A), (B) and (C), respectively.

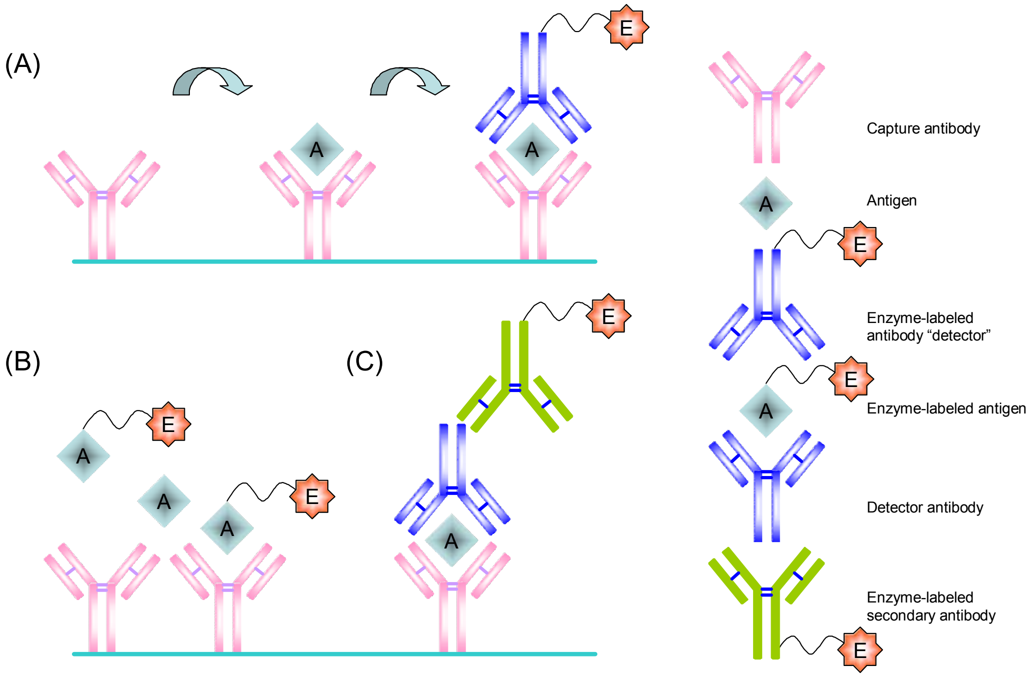

Figure 5.6: Schemes of different ELISA immunoassays. (A) Sandwich immunoassay. (B) Competitive immunoassay. (C) Sandwich immunoassay with secondary antibody amplification.

The first one is "sandwich" assay (cf. Figure 5.6 (A)). In this type of assay, the analyte is "sandwiched" between two different antibodies. A capture antibody is usually bound to a solid support. This antibody binds antigen (analyte) from the sample solution. After a rinse step to separate free from bound antigen, an enzyme-labeled detector antibody is added, which binds to a different epitope on the antigen. After the incubation and rinse steps, the enzyme substrate is added. The amount of colorimetric substrate product is proportional to the amount of labeled antibody bound to the support, which is proportional to the concentration of antigen in the sample[97].

Competitive assays (cf. Figure 5.6 (B)) are often used if the antigen is small and has only one epitope, or antibody binding site. The ligand is labeled instead of the antibody. The unlabeled antigen and the labeled antigen compete for binding to the capture antibody. The amount of color developed is inversely proportional to the amount of the unlabeled antigen. Careful standardization is required to interpret the results.

The ELISA assay can be designed with the use of a secondary antibody instead of a labeled primary antibody. Figure 5.6 (C) is a schematic of how these assays may be designed. In principle, the incubation step with the labeled primary antibody is replaced by two incubations, first with the primary (unlabeled) antibody, then with the labeled secondary antibody.

5.5.2 SPFS hCG Sandwich Assay and LOD determination

For the SPFS hCG immunoassay, we used a sandwich assay format first because of its better sensitivity and specificity for measurements of protein analytes. Surely, the enzyme-labeling was replaced with Alexa Fluor 647-labeling in our assays for fluorescence characterization. Based on the antibodies at hand, four kinds of combinations were designed.

1) Bio-α-IgG/hCG/AF-β-IgG
2) Bio-β-IgG/hCG/AF-α-IgG
3) Bio-Fab/hCG/AF-β-IgG
4) Bio-Fab/hCG/AF-α-IgG

50 μg hCG samples from Sigma were dissolved in 69.8 μl PBS buffer, adding 1.4 μl 0.5% NaN_3 to form a 10^7 mIU/ml (18.5 μM) stock solution, prevented from concentration depletion. A biotin SAM ($\chi = 0.01$) surface was used in 1) and 2), biotin SAM ($\chi = 0.1$) surface was used in 3) and 4) in order to get the maximum immobilization of hCG (cf. Section 5.3). For the functionalization of the SAM surface, a 500 nM streptavidin solution in PBS buffer was always circulated in the flow cell for 15 minutes first. Then a biotinylated antibody or Fab fragment solution with the concentration of 500 nM was introduced in the loop, circulated for 30 minutes to saturate the surface. 1 ml Glycine buffer (10 mM Glycine-HCl, pH 1.75) was always injected and circulated for 5 minutes

in order to get rid of the loosely bound molecules on the surface before the dose response experiments were done.

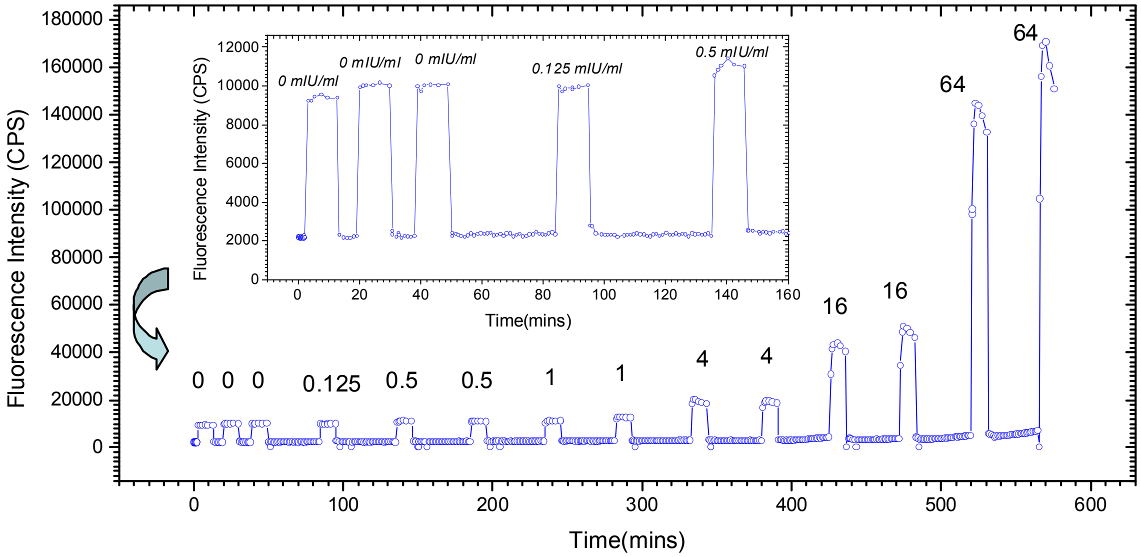

Figure 5.7: Kinetic fluorescence working curve of Bio-Fab/hCG/AF-β-IgG immunoassay. The inset shows the amplification of the beginning part of fluorescence response at low concentration samples injectioin.

Taking combination 3) as an example, for every experimental injection, 1 ml hCG samples with the desired concentrations (0.125 mIU/ml, 0.5 mIU/ml, 1 mIU/ml, 4 mIU/ml, 16 mIU/ml, 64 mIU/ml) were prepared in PBST buffer. Each sample was injected into the flow cell and circulated in the loop for 30 minutes. After a brief buffer rinse, 500 μl 10 nM AF-β-IgG solution prepared in PBST buffer was introduced in the circulation system for 10 minutes. Finally, this AF-β-IgG solution was replaced with PBST buffer and the surface was regenerated with the Glycine buffer (10 mM Glycine-HCl, pH 1.75), waiting for the next cycle of binding. Each concentration was repeated twice except the 0.125 mIU/ml sample, which did not produce an obvious response compared with the negative control sample. For the negative (or blank) sample, 10 nM AF-β-IgG solution was injected into the flow cell directly, the fluorescence jump from the chromophores in solution excited by the SPR evanescent field tail could be totally reversed after a fresh buffer rinse, suggesting the good resistivity of the supramolecular structure against non-specific impurity binding. The kinetic fluorescence working curve is shown in Figure 5.7. The fluorescence intensity signal at the end of a 10 minutes AF-β-

IgG circulation was used for the dose-response calibration curve plotting, which is shown in Figure 5.8 (C) and (D). The linear fit line illustrates a theoretical LOD of 0.5 mIU/ml (cf. Section 4.5.3.1), equivalent to 0.9 pM. Apparently, increasing the incubation time of hCG will improve the sensitivity of the assay, but impair the linearity of the dose-response curve simultaneously because prolonging of reaction time will bring the final response closer to the saturation level at this concentration, changing the curve into a titration working plot for a Langmuir isotherm.

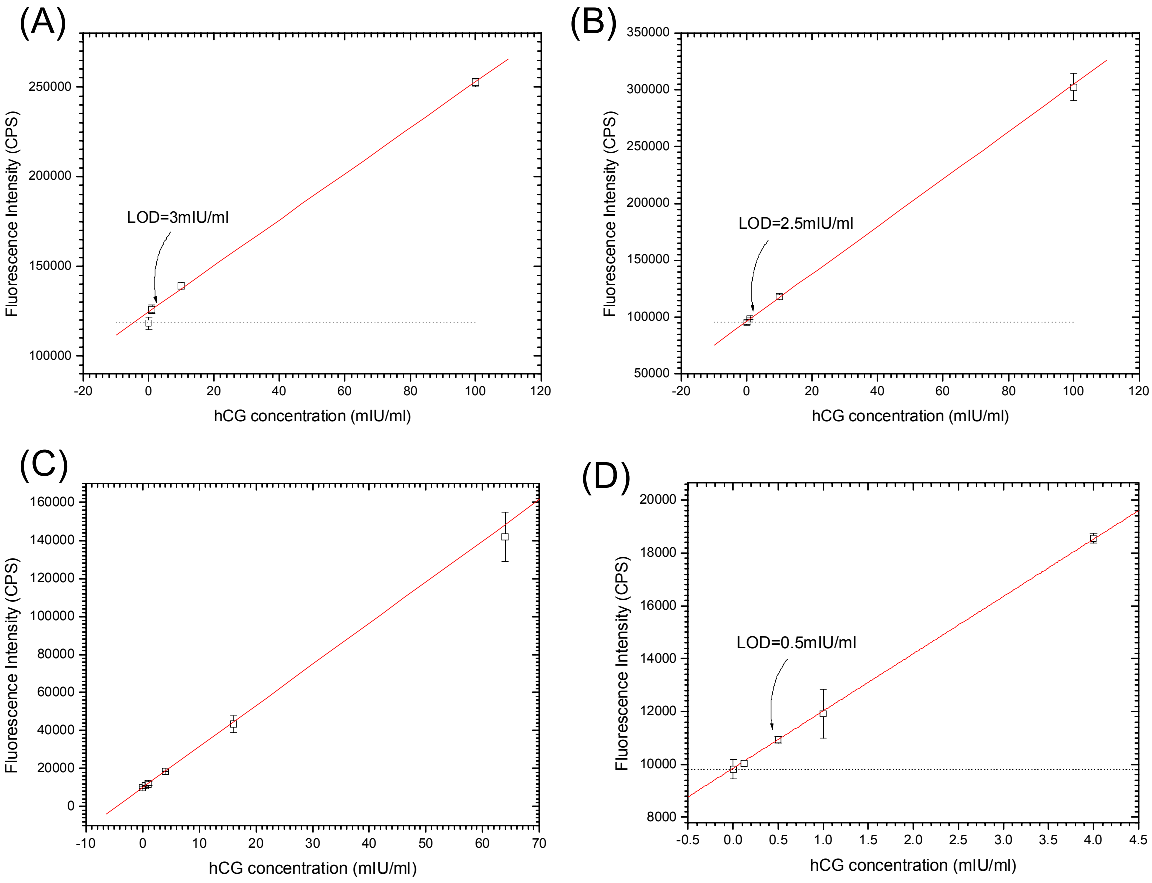

Figure 5.8: Dose-response curves of different immunoassays. (A) Bio-α-IgG/hCG/AF-β-IgG. (B) Bio-β-IgG/hCG/AF-α-IgG. (C) Bio-Fab/hCG/AF-β-IgG. (D) Amplification of (C) in the low concentration part.

Similarly, for combination (1) and (2), the LOD results of 3 mIU/ml and 2.5 mIU/ml were obtained respectively (cf. Figure 5.8 (A) and (B)). There is not too much difference between the LOD results of these two methods constructed with surface bound whole biotinylated antibodies. But the employment of biotinylated Fab fragments can greatly improve the performance of the immunoassay, which is attributed to the larger number of active anchoring sites owing to the better orientation of the Fabs on the surface.

Another interesting phenomenon was observed that when utilizing combination (4), after the injection of a high concentration (41.7 nM) of AF-α-IgG, there was only a "background jump" originating from fluorophores in the bulk solution. This background signal could be almost completely reversed to the baseline level after a fresh buffer rinse. A glimpse of the three dimensional structure of hCG epitopes (cf. Figure 5.1 (B)) could fully explained this unusual behavior. The Fab fragment of M-1F7.9 is directed toward the epitope c2, while the anti-α-hCG IgG interacts with the region of the α1α2α4 epitopes. These epitopes are very close to each other and, hence result in steric hindrance, which will strongly restrict further access of the huge AF-α-IgG molecules once hCG is bound to the Fab surface. On the contrary, in combination (3), the anti-β-hCG IgG interacts with the region of the β2-β6 epitopes, which are separated sufficiently from the epitope c2, insuring good detectability. Therefore, the proper selection of antibody combinations will dramatically impact on the performance of immunoassays. Theoretically, the antibody specific to the β2-β6 epitopes together with the antibody specific to the α3α5 epitopes could be considered as the best partners.

5.6 Other Assays

5.6.1 "One Step" Sandwich Assay

Referring to the method used in Section 5.7 as the "two steps" sandwich immunoassay, one of its disadvantages is that hCG anchoring and AF labeled antibody immobilization need to be completed separately, which increases the consumed time of one individual cycle. A more efficient assay will be highly appreciated in clinical diagnostics. Combining the two separate couplings steps mentioned above, leads to a "one step" sandwich immunoassay.

Figure 5.9 (A) shows the kinetic fluorescence working curve of this "one step" method based on the antibody combination Bio-Fab/hCG/AF-β-IgG. After surface activation, a series of 1ml mixed samples prepared in PBST buffer with the hCG concentration of 0 mIU/ml (negative sample), 0.5 mIU/ml, 1 mIU/ml, 8 mIU/ml and 64 mIU/ml, respectively, together with a fixed concentration of 5 nM AF-β-IgG were injected into the flow cell and circulated for 30 minutes in the loop. The Bio-Fab surface was regenerated with the Glycine buffer (10 mM Glycine-HCl, pH 1.75) in the intervals. Each concentration was repeated twice. The fluorescence response signal at the end of 30 minutes before regeneration was recorded for the dose-response plot (cf. Figure 5.9 (B) and (C)), in which the straight fit line illustrates the excellent linearity. Extrapolating the linear fit curve to the baseline level resulted in a theoretical detection limit of 0.15 mIU/ml, equivalent to 0.28 pM, at the same order of magnitude with the "two steps" SPFS sandwich assay. The benefits of the proper orientation of the Fab fragment were again obvious and the incorporation action even saved 10 minutes of time for each cycle in the assay.

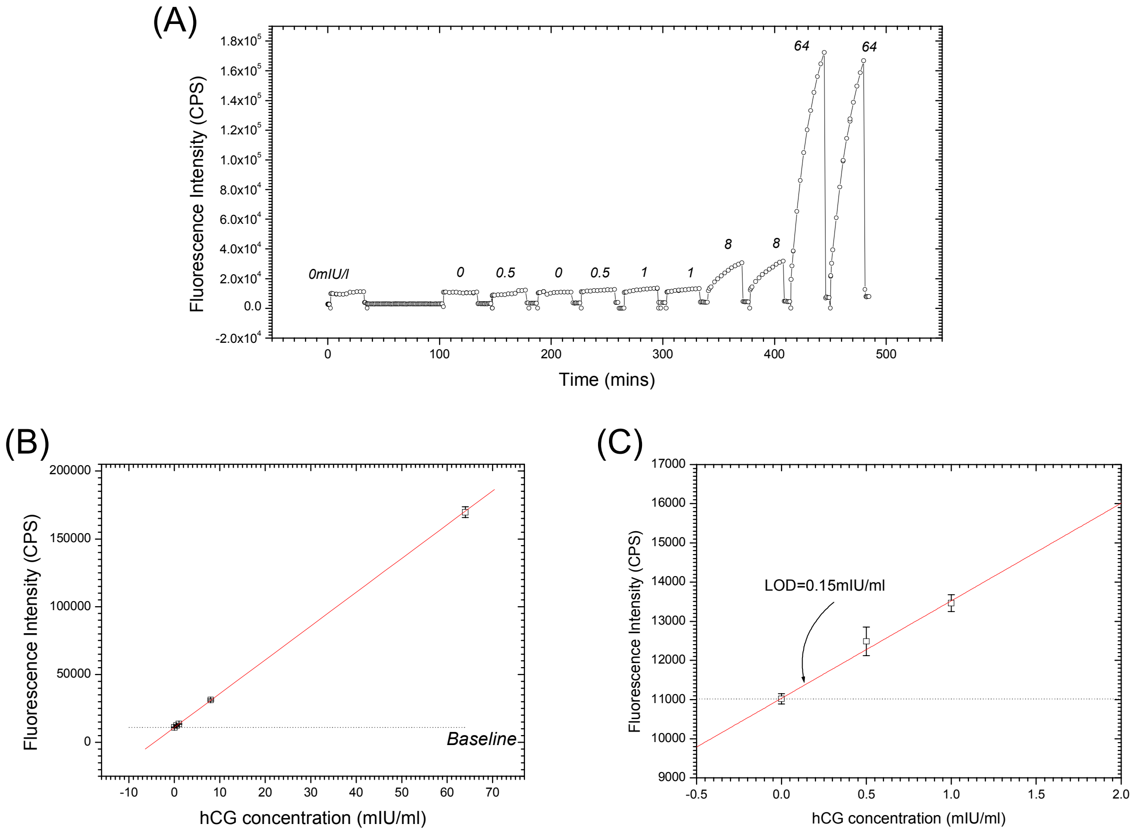

Figure 5.9: The result of "one step" sandwich immunoassay. (A) Kinetic fluorescence working curve. (B) Dose-response curve. (C) The amplification for the low concentration part in (B).

5.6.2 Competitive Assay

As discussed in Section 5.5, another popular ELISA method is the competitive immunoassay, which is based on the competition between labeled antigens with a concentration already known and unlabeled antigens with concentrations to be tested. The presumption for this method is that the affinity between the antibody and the unlabeled antigen is almost same as the affinity between the antibody and the labeled antigen. For a SPFS immunoassay, the same principle can be adopted to test the concentration of hCG. No matter what kind of antibody surface was preconstructed, the higher the amount of the unlabeled hCG in the mixed solution, the weaker the fluorescence intensity response after a fixed time of reaction should be.

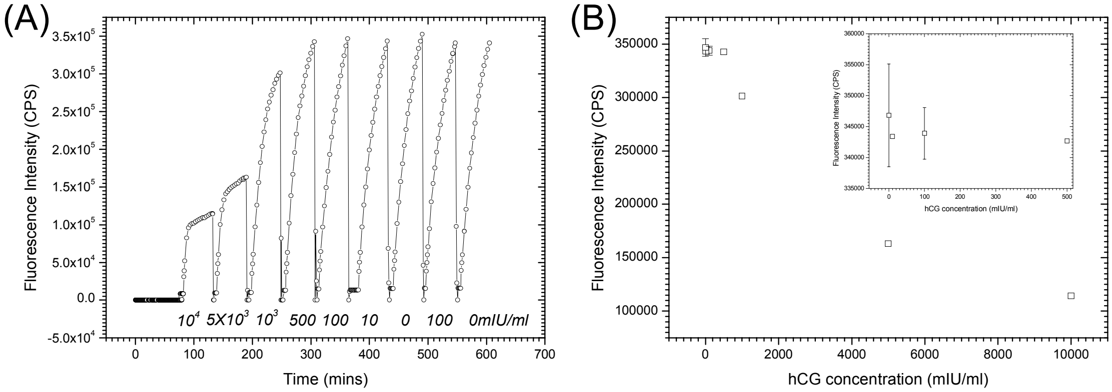

Figure 5.10: The result of competitive immunoassay. (A) Kinetic fluorescence working curve. (B) Dose-response curve. The inset shows the amplification in the low concentration part.

After the functionalization of the chip with a Bio-Fab/streptavidin/biotin SAM ($\chi = 0.1$) coating, a series of 1ml mixed samples prepared in PBST buffer with hCG concentrations of 10^4 mIU/ml, 5×10^3 mIU/ml, 10^3 mIU/ml, 500 mIU/ml, 100 mIU/ml, 10 mIU/ml, and 0 mIU/ml (negative sample), respectively, were injected into the flow cell and circulated for 50 minutes in the loop together with a fixed concentration of 1.088 nM AF-hCG. Glycine buffer was chosen as the regeneration buffer as usual. The kinetic fluorescence working curve is shown in Figure 5.10 (A), and the dose-response curve, *i.e.* the fluorescence intensity response after 50 minutes before regeneration versus the hCG concentration, is plotted in Figure 5.10 (B).

Even without calculation, one can directly judged from Figure 5.10 that the sensitivity of the competitive assay is not as high as the sandwich assay, which might be attributed to the inversely proportional relation between the response signal and the hCG concentration. The competition behavior, the varying concentration of total hCG in the mixed solution, the appropriate selecting of the labeled hCG concentration, and the dye labeling efficiency all have a strong influence on the calibration curve. A full evaluation of this complicated system needs further investigations. Nevertheless, this competitive assay still can be employed as a primary screening method of hCG examination for its strict inversely proportional characteristic in the high concentration range of the dose-response curve, as well as for the comparatively less time consumed.

5.7 Conclusion

This chapter presented examples for hCG detection, confirming the potential of SPFS as a new strategy for clinical immunoassays.

The biophysical and immunological features of hCG were presented first, followed by a short introduction of biosensors and immunosensors. After the investigation of the effect of the biotin thiol dilution on the efficient coupling, the interfacial binding model including the appropriate binary SAM structure and the versatile streptavidin-biotin interaction was chosen as the basic supramolecular architecture for the fabrication of a SPFS-based immunoassay. Next, the affinity characteristics between different antibodies and hCG were measured via an equilibrium binding analysis, which is the first example for the titration of such a high affinity interaction by SPFS. The results agree very well with the constants from literature. Finally, a sandwich assay and a competitive assay were selected as templates for SPFS-based hCG detection, and an excellent LOD of 0.15 mIU/ml was attained via the "one step" sandwich method. Such high sensitivity not only fulfills clinical requirements (cf. Table 5.1), but also triumph over almost all other biosensor rivals[98-104].

6 SURFACE IMMOBILIZATION STRATEGIES OF LHCIIS AND ENERGY TRANSFER BETWEEN NEIGHBORING LHCIIS

6.1 Introduction

Photosystems are arrangements of chlorophylls and other pigments bound to proteins and packed into thylakoids. Many prokaryotes have only one photosystem, while all oxygenic photosynthetic organisms, including cyanobacteria, algae, and higher plants, contain two different reaction center complexes, designated as Photosystem I (PSI) and Photosystem II (PSII), which catalyze the conversion of the light energy captured in excited chlorophyll molecules into useful forms. All photosystems contain a reaction center with its full complement of electron transfer components as well as an array of light-harvesting, or antenna, complexes. These antenna complexes function to absorb light energy, transferring it to the reaction center, where the energy is then converted into stable chemical products.

Complex	Chl *a/b* ratio	Gene	Mol. Mass (kDa)
LHCIIa (CP29)	4.0	*lhcb4*	29
LHCIIb (LHCII)	1.35	*lhcb1*	27-28
		lhcb2	25-27
		lhcb3	25
LHCIIc (CP26)	2.9	*lhcb5*	26.5
LHCIId (CP24)	1.51	*lhcb6*	24

Table 6.1: Properties of light-harvesting chlorophyll a/b protein complexes associated with PSII.

At least 20 protein subunits are associated with PSII *in vivo* in higher plants and green algae[105]. They have been named after the genes encoding them (*psbA-psbY, lhcb1-lhcb6*). Analysis of pigment-protein complexes by mildly denaturing gel electrophoresis methods results in the separation of individual chlorophyll-protein complexes in which each protein retains its native chlorophyll array. The peripheral antenna systems in the PSII complex of higher plants are quite diverse in terms of structure and relative position in the energy transfer sequence. There are two types of chlorophyll *a/b* containing antenna complexes, one comprises the minor peripheral antenna complexes *lhcb4*, *lhcb5* and *lhcb6* (or CP29, CP26 and CP24, respectively), the other comprises the major peripheral antenna complexes *lhcb1*, *lhcb2* and *lhcb3*, or in a general notation, LHCII (cf. Table 6.1). While there are good reasons to believe that most LHCII complexes are organized as trimers in the thylakoids[106], the minor antenna complexes probably occur in the photosystems in their monomeric form[107].

6.1.1 Structural Properties of LHCII

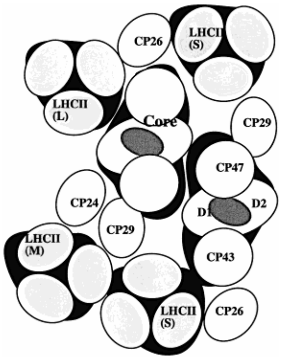

Figure 6.1: Schematic representation of parts of the C2S2ML PSII-LHCII supercomplex. Charge separation takes place in D1D2, which together with CP47 and CP43 forms the core. The minor Chl *a/b* proteins CP24, CP26 and CP29 are bound next to the core. LHCII can bind at different positions (S, indicating strong binding; M, moderately strong binding; L, loose binding)[108].

PSII is the only biological system known to be capable of oxidizing water to molecular oxygen, hence, it has been studied extensively, trying to understand how the natural system works, but also in the context of artificial systems for energy conversion. An essential precondition for understanding the reactions that are involved in the oxidation of water is a detailed model of the three-dimensional structure of the complex. Both electron microscopy and X-ray crystallography have contributed to the elucidation of the structure of the PSII complex[109-111]. While most of the crystallographic investigations have been performed with core complexes or subcomplexes, the detailed structure of a complete PSII-LHCII supercomplex was done by electron microscopy and image analysis. Based on these studies, such a supercomplex consists of a dimeric PSII core complex, abbreviated as “C” and a trimeric LHCII complex in three different types of binding positions. These positions were named S, M and L in the case of higher plants, in which “S” refers to a strongly, “M” to a moderately and “L” to a loosely bound trimeric LHCII complex[109]. The example of a supercomplex C_2S_2ML is depicted in Figure 6.1, where besides the trimeric LHCII complexes the three minor peripheral monomeric antenna complexes are shown on each side of the complex.

It's obvious that the minor antenna complexes are more closely associated with PSII than LHCIIs. Although these minor complexes bind about 20% of the chlorophyll[105], their major role is thought to facilitate and control the excitation energy transfer from LHCII to the reaction center other than to harvest light. On the contrary, LHCII, as the major peripheral antenna complex, represents about half of the total protein in the thylakoids membrane[16], accounting for 50-65% of the pigments in plant photosynthesis.

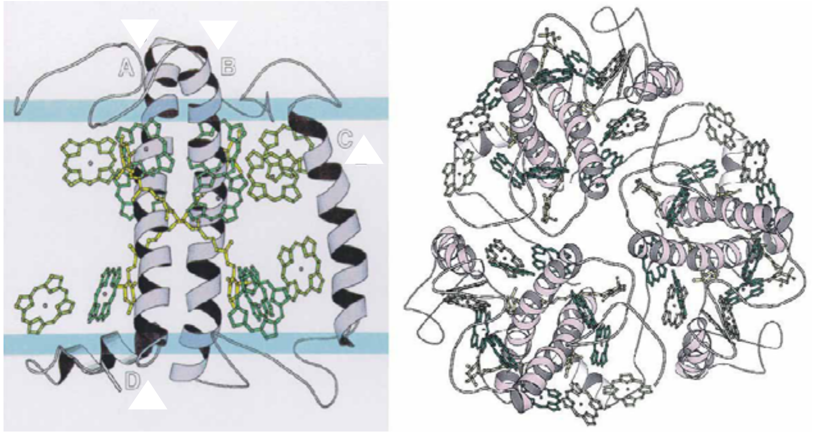

Figure 6.2: Views of LHCII. Left: Side view of LHCII monomer[110]. Blue bands indicate the approximate position of the thylakoids membrane. Helices are labeled A to D. Color code: dark green, Chl a; light green, Chlb; pink, Mg atoms; yellow, luteins; violet, membrane-spanning helices. Right: Top view of LHCII trimer.

A major step forward in the understanding of the process of light harvesting in PSII was the elucidation the near-atomic structure of LHCII by Kühlbrandt[110] and Liu[111] using electron crystallography. A model of the LHCII monomeric subunit that is based on the crystal structure is shown in Figure 6.2. The model shows a polypeptide backbone of 232 amino acids that binds and organizes a minimum of 12 chlorophylls and 2 carotenoids (luteins). The three transmembrane α-helices (A, B and C) and a short amphiphilic helix (D) are particularly well-resolved at the interface of the protein and the water surroundings. The maximum thickness of the complex, as defined by the highest residues on the stromal (outer membrane) side and the lowest one on the lumenal (inner membrane) side, was 48 Å. The longest and the shortest lateral dimensions of the monomer were 48 Å and 32 Å, respectively. The chlorophylls are attached to the polypeptide by coordination of the central magnesium atom to polar amino-acid side chains or to main-chain carbonyls in the hydrophobic interior of the complex. The LHCII structure is not only important for the study of LHCII itself, it also serves as a model for the structure of the minor Chl *a/b* proteins of PSII, the LHCI complexes of PSI, early-light induced proteins (ELIPs) and Chl *a/c* binding proteins of Chl *c* containing algae, which all share a large amount of sequence homology with LHCII.

6.1.2 Spectroscopic Properties of LHCII

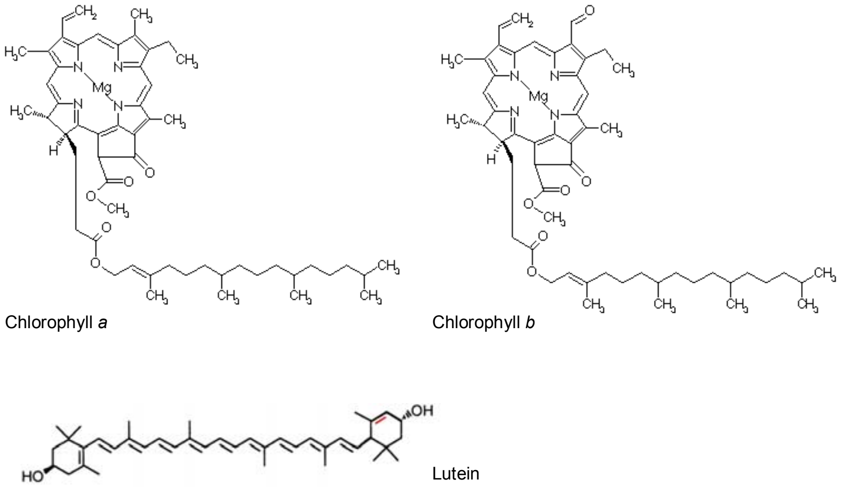

Chlorophyll *a*

Chlorophyll *b*

Lutein

Figure 6.3: Molecular structures of chlorophyll a, chlorophyll b and lutein (the most abundant carotenoids in the plant chloroplast).

The vast majority of photosynthetic organisms contain some forms of the light-absorbing pigment chlorophyll. Chlorophyll molecules (cf. Figure 6.3) contain a tetrapyrrole ring (porphyrin) structure like that found in the heme prosthetic group of hemoglobin and the cytochromes. However, chlorophylls bind magnesium atoms in the center of their tetra-pyrrole rings, whereas hemes bind iron atoms. In addition, a long (C_{20}) hydrophobic side chain, known as a phytol tail, is attached to the tetra-pyrrole ring structure of chlorophyll and renders the molecule extremely nonpolar. Various chlorophylls differ in their substituents around the ring structure. In the case of chlorophyll *a* and *b*, a methyl group is present in the former, whereas a formyl group is present at the same position in the latter. These small changes in chemical structure substantially alter the absorption properties of the different chlorophyll species. Figure 6.4 (A) shows the UV absorption spectra of chlorophyll *a* and *b*. Chlorophyll *a* absorbs light more efficiently at the wavelength of $\lambda = 410$ nm and $\lambda = 660$ nm, while chlorophyll b has two absorption peaks which are at $\lambda = 460$ nm and $\lambda = 640$ nm. The solvents used to dissolve these nonpolar chlorophylls will "tune" the absorption spectrum to slightly different positions. If chlorophyll associates with specific proteins found in the photosynthetic membrane, its peak absorption wavelength shifts toward the red spectral region (cf. Figure 6.4 (B)).

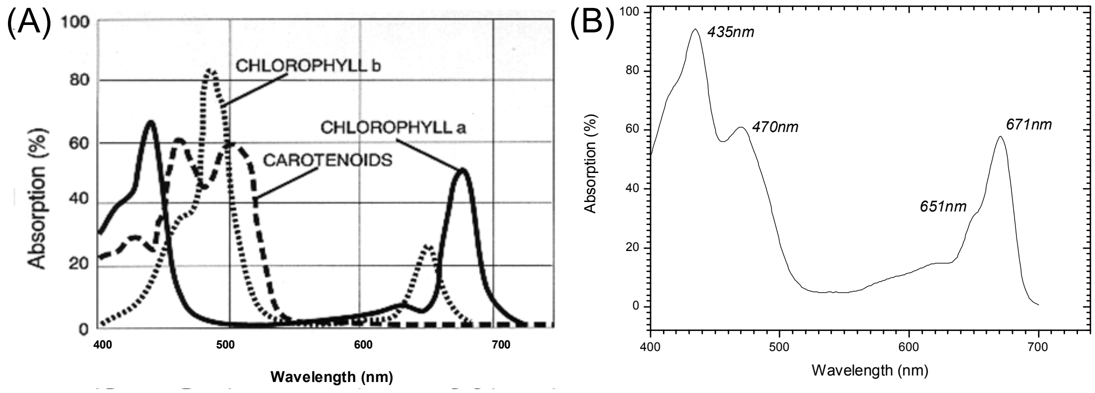

Figure 6.4: UV absorption spectra of Chl a, Chl b and carotenoid (A), as well as LHCII (B).

A second group of pigment molecules found in all photosynthetic organisms are the carotenoids (cf. Figure 6.3), which are responsible for the orange-yellow colors observed in the leaves of plants, because they absorb light in the 450-500 nm region (cf. Figure 6.4 (A)). As such, carotenoids play a minor role as accessary light-harvesting pigments, absorbing and transferring light energy to chlorophyll molecules. Carotenoids, however, play an important structural role in the assembly of light-harvesting complexes and have an indispensable function in protecting the photosynthetic apparatus from photo-oxidative damage.

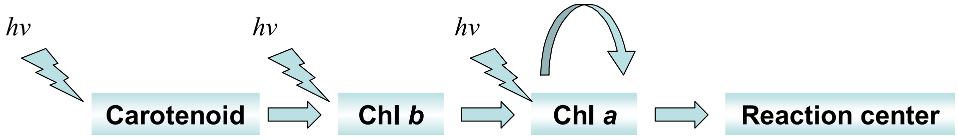

Figure 6.5: The energy transfer direction in Photosystem II.

Because the reaction center complex absorbs longer wavelengths than the antenna, the reaction center chlorophyll acts as an energy trap, promoting transfer of energy from the antenna toward the reaction center complex. The energy transfer sequence before charge separation in PSII is shown in Figure 6.5.

Take a chlorophyll molecule as an example, the process of energy conversion begins once it is excited by a quantum of light (a photon) and an electron is moved from one molecular orbital to another of higher energy. Such an excited molecule is unstable and will tend to return to its original, unexcited state in one of three ways (cf. Figure 6.6)[112]: (A) by converting the extra energy into heat or to some combination of heat and light of a longer wavelength (fluorescence); (B) by transferring the energy – but not the electron – directly to a neighboring chlorophyll molecule by Förster energy transfer (cf. Section 2.2.2); (C) by transferring the high-energy electron to another nearby molecule (an electron acceptor) and returning to its original state by taking up a low-energy electron from some other molecule (an electron donor).

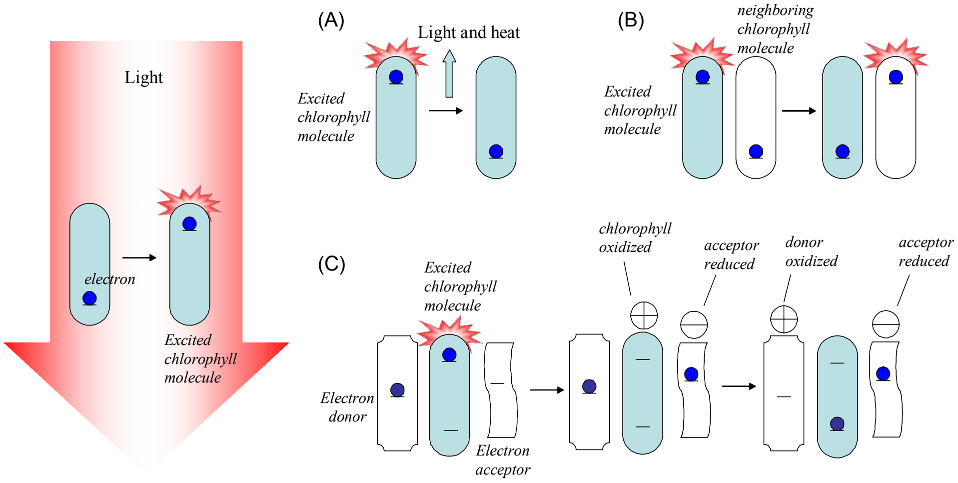

Figure 6.6: Three possible ways for an excited chlorophyll molecule return to its original, unexcited state. The light energy absorbed by an isolated chlorophyll molecule is completely released as light and heat by process (A). In photosynthesis, chlorophylls undergo process (B) in the antenna complex and process (C) in the reaction center.

All light-harvesting chlorophyll *a/b* proteins (LHCP) in eukaryotes are coded for in the nucleus, synthesized by cytoplasmic ribosomes and posttranslationally imported into the plastid. However, the mechanism of how LHCP enters the thylakoids membrane remains largely unknown[17]. Although the biogenesis of LHCII is still in the focus of photosynthetic investigations, reconstitution of LHCII *in vitro* has successfully revealed that pigments trigger refolding of detergent denatured LHCP[55]. The reconstitution products exhibited very similar biochemical and spectroscopic properties as their native counterparts[113]. The reconstituted complex is at least in part functional, as the energy transfer from Chl *b* to Chl *a* is virtually 100% efficient[53], which means the excitation of this complex with the absorption peak of Chl *b*, λ = 460 nm for instance, only produces the emission peak of Chl *a* (cf. Figure 6.7). This energy transfer is called “intra-complex energy transfer” in our study.

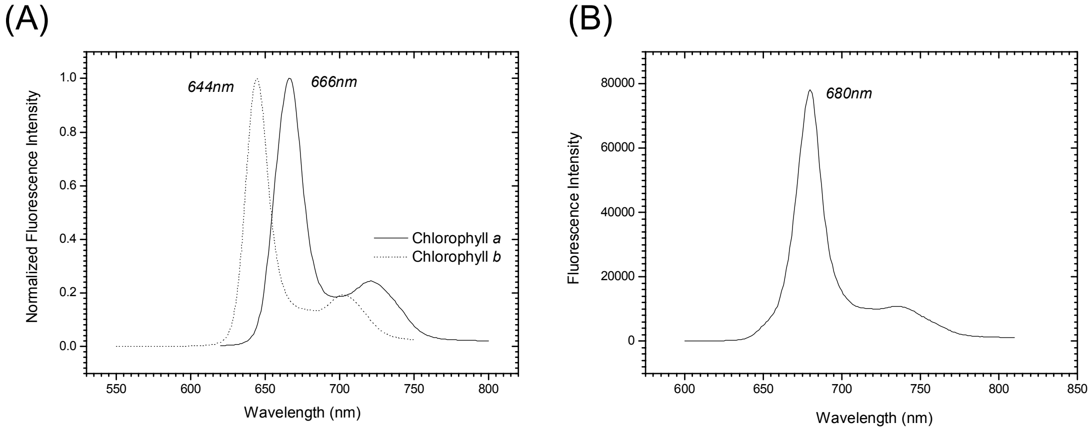

Figure 6.7: Fluorescence emission spectra of chlorophylls and LHCII. (A) Fluorescence emission spectrum of Chlorophyll a (solid line) and Chlorophyll b (dot line) dissolved in diethyl ether. (B) Fluorescence emission spectrum of LHCII in detergent contained buffer using an excitation wavelength of λ = 460 nm.

6.1.3 Methods and Purpose of This Study

Studies of photosynthesis, particularly those processes related to the light reactions, have benefited greatly from a vast array of experimental techniques relied on characteristic “signatures” that distinguish the oxidized from the reduced species of a given molecule, *e.g.* absorbance difference spectroscopy and electron paramagnetic resonance (EPR)[16]. Since there’s no electron transfer reaction happening in the light-harvesting complex, approaches of various spectroscopic techniques including optical absorbance spectroscopy, fluorescence emission spectroscopy, circular dichroism spectroscopy and linear dichroism spectroscopy are the most general ways to investigate the relations between the LHCII’s structures and functions. Apart from these, time-resolved fluorescence spectroscopy has also been used to study the assembly kinetics of such pigment-binding membrane proteins for distinct discrimination from the background fluorescence[114].

On the other hand, most of these studies on chlorophyll binding proteins have been done in detergent containing homogeneous aqueous solution, whereas almost no investigations on the surface are reported. Lee *et al.* tried to immobilized Photosystem I from spinach thylakoids on a gold substrate, using STM tunneling conductance (I-V) measurements[115] and Kelvin force probe microscopy (KFM)[116] to characterize the electrostatic current and potential changes of individual reaction centers. The coupling ways they used were either to platinize of PSI then to anchor it onto a metal surface by PSI-platinum-gold bonding, or to self-assemble PSI reaction center on organosulful-modified gold substrates for prospective orientation[117], neither of which were both specific and reversible. Nakamura *et al.* designed a herbicides assay using a self-assembled photosynthetic reaction center from the purple bacterium on a Biacore's Sensor Chip NTA[118]. Although this specific binding method was carried out on Biacore's three-dimensional dextran matrix, the density of immobilized HHisRCs was only 10 fmol/mm^2. LHCII is one of the most stable and abundant pigment-protein complexes of the thylakoids membrane and thus could easily be isolated. Moreover, techniques to reconstitute LHCII *in vitro* are also well developed. However, little has been done with LHCII in order to explore its characteristics on the surface except some single molecular spectroscopic studies recently[119] based on spin coating of the complexes onto a glass substrate, which was purely non specific adsorption. Moreover, almost all the works mentioned above dealed with individual single protein complexes. None of the studies considered the lateral interaction among complexes, which we call "inter-complex energy transfer", truly existing in the thylakoids membrane[108].

In this chapter, we will apply different strategies to attach LHCII to gold substrates and to use SPFS to study its surface binding behavior, as well as the resonance energy transfer between neighboring complexes. The advantage of SPFS to monitor refractive index changes and fluorescence variations simultaneously matched to the LHCII's distinct feature as a self-fluorescent membrane protein. Although SPFS is usually used to explore interactions perpendicular to adjacent interfaces, a new analytical method to prove communication between laterally adjoining complexes will be proposed.

6.2 Materials

Clone	Amino acids sequence description	Source-clone	Working name
C79S	D7f.3 with Ser replacing Cys in position 79	D7f.3	Hu1
S3Ch	C79S with Cys replacing Ser in position 3, 6His-motif at C-terminus	C79S C2.4h	Hu4
V229C	C79S with Cys replacing Val at C-terminus	C79S, 37i.1	Hu8
S160Ch	C79S with Cys replacing Ser in position 160, 6His-motif at C-terminus	C79S, pS160Ch	Hu10
C3.2h	D7f.3 with 6His-motif at C-terminus	D7f.3	C3
D7f.3S1	D7f.3 with Strep-tag at N-terminus, sequence: WSHPQFEKG…	D7f.3	S1
D7f.3S2	D7f.3 with Strep-tag at N-terminus, sequence: WSHPQFEKA…	D7f.3	S2

Table 6.2: Different LHCP clones used in the experiments.

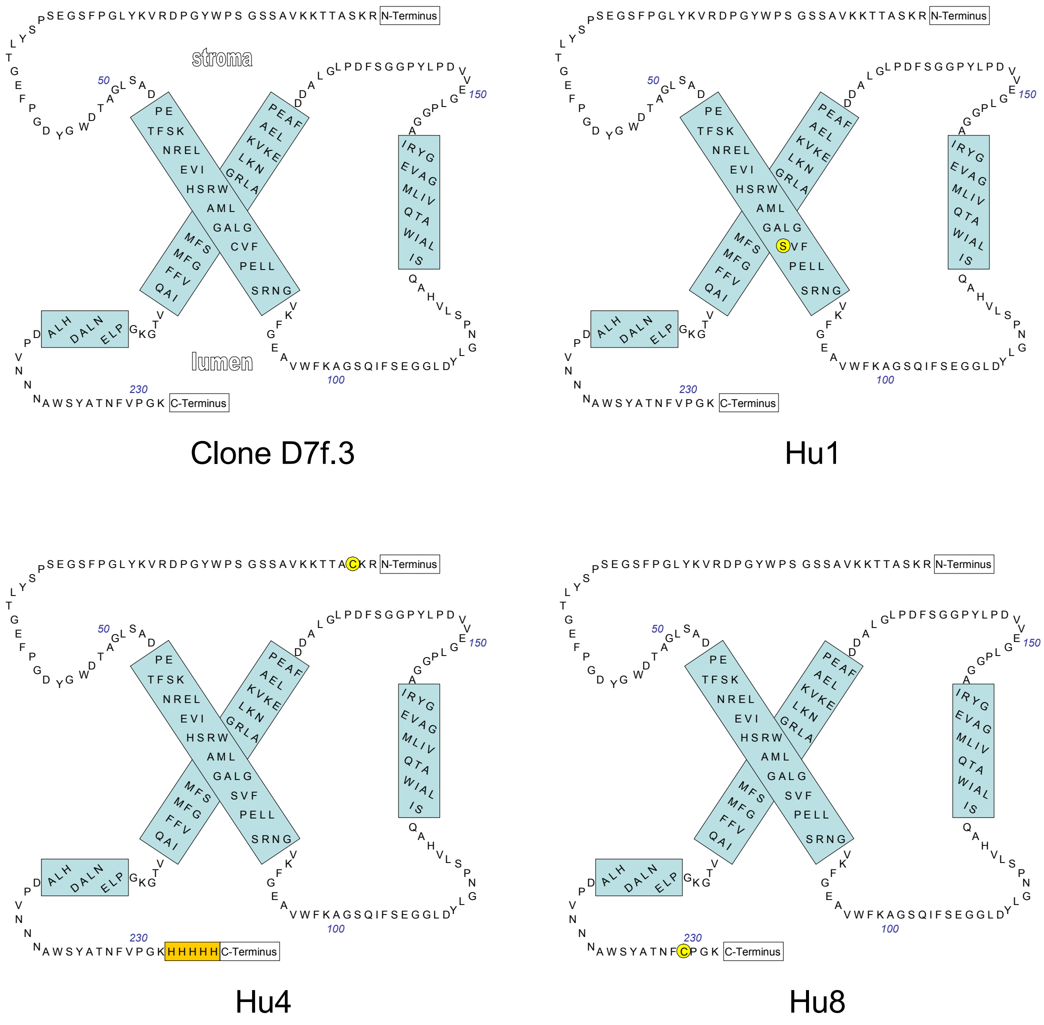

Clone D7f.3

Hu1

Hu4

Hu8

Figure 6.8: Amino acids sequences of different clones.

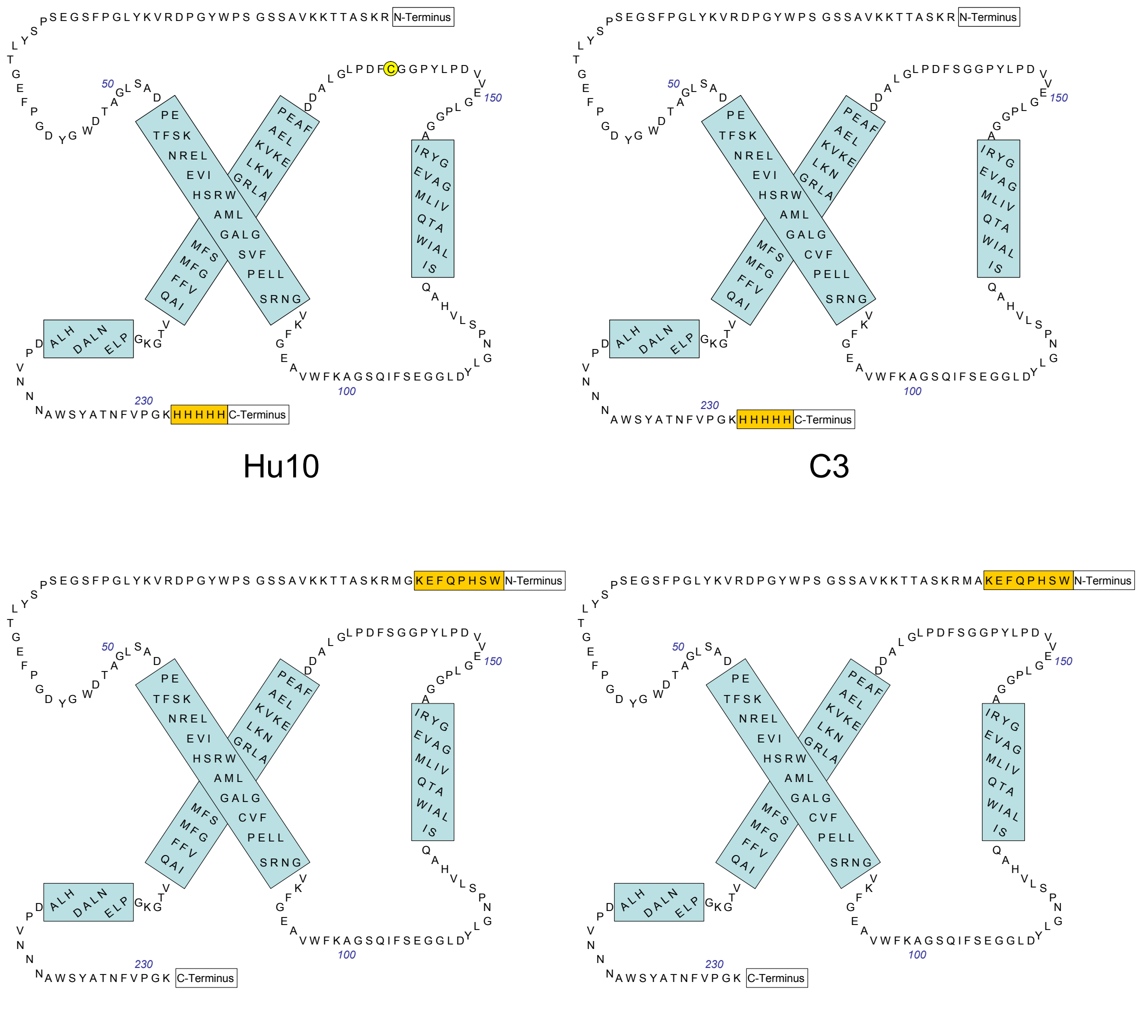

Hu10 C3

S1 S2

Figure 6.8 (continued)

The apoprotein used in all experiments is *lhcb1* over-expressed in *Escherichia coli*. All LHCP clones are derived from clone D7f.3, which carries the constructs of the AB80gene from pea[120], except some point-specifically mutations. Table 6.2 gives simple descriptions of all clones and their abbreviated names used in this chapter. The amino acids sequence of clone D7f.3 and its mutations are plotted in Figure 6.8.

Total exact including chlorophylls and xanthophylls was isolated from pea thylakoids by acetone extraction, and subsequent dioxane-water precipitation[121].

The reconstitution of LHCII is described in Section 3.3. The molecular weight of one LHCII monomer is 35 kDa, including the components of the apoprotein (~25 kDa) and the pigments (~10 kDa). The concentrations of the complexes were calculated on the basis of the extinction coefficient of $\varepsilon = 546000\ M^{-1}cm^{-1}$ at $\lambda = 670$ nm as determinated by Butler and Kühlbrandt[56]. All concentrations of LHCII refer to monomeric concentrations in this chapter, even when the complexes are organized in a trimeric form. Biological functions of all complexes (intra-complex energy transfer) have been checked by using fluorescence emission spectroscopy prior to the surface coupling.

The biotinylation and fluorescence labeling of LHCP were kindly completed by Rolf Lauterbach, PhD student in Prof. Harald Paulsen' group, using Biotinamidocaproate N-hydroxysuccinimide ester from Sigma-Aldrich and DY-730 maleimide from Dyomics GmbH, respectively.

Ethanolamine hydrochloride (EA), N-(3-dimethylaminopropyl)-N'-ethylcarbodiimide hydrochloride (EDC), N-Hydroxysuccinimide (NHS), 3-(2-Pyridyldithio)propionic acid N-hydroxysuccinimide ester (SPDP), 11-mercaptoundecanoic acid and 11-mercapto-1-undecanol were purchased from Sigma-Aldrich. NTA terminated OEG (oligo ethylene glycol) thiol ($C_{33}H_{61}N_2O_{12}S$) (cf. Figure 6.9 (1)) and OEG spacer thiol ($C_{22}H_{44}O_5S$) (cf. Figure 6.9 (2)) were kindly provided by Prof. Robert Tampé's group.

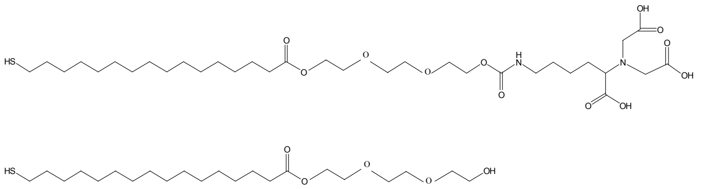

(1) Molecular Weight= 709.92

(2) Molecular Weight= 420.66

Figure 6.9: Chemical structures of NTA terminated OEG thiol (1) and OEG spacer thiol (2).

N-(5-Amino-1-carboxyentyl)iminodiacetic acid, disodium salt, monohydrate (AB-NTA, ANTA or NTA ligand) was purchased from Dojindo Molecular Technologies, Inc.. Ni-NTA AP conjugate was purchased from Qiagen GmbH. Biotin conjugated affinity purified anti-6×His TAG (Rabbit) (biotinylated anti-6His IgG) was from Rockland Immunochemicals, Inc.. Biotin-X-NTA and Alexa Fluor 700 streptavidin conjugate were purchased from Molecular Probes.

Monoclonal anti-avidin-biotin conjugate (biotinylated anti-avidin IgG) and avidin were from Sigma.

1,2-Dipalmitoyl-*sn*-Glycero-3-[Phospho-*rac*-(1-glycerol)] (Sodium Salt) (PG), 1, 2-Distearoyl-*sn*-Glycero-3-Phosphoethanolamine-N-[Biotinyl(Polyethylene Glycol)2000] (Ammonium Salt) (Biotin -PEG-DSPE), L-α-phosphatidylcholine (Egg, Chicken) (PC) were obtained from Avanti Polar Lipids, Inc.. PEG 8000 was purchased from Promega GmbH. Bio-Beads SM-2 was from Bio-Rad Laboratories.

CHAPS, Triton®X-100, n-Dodecyl-β-D-maltoside (DM), ethylenediaminetetraacetic acid disodium salt dehydrate (EDTA), MOPS, HEPES, Trizma®Base, Trizma®hydrochloride, sodium phosphate monobasic (NaH_2PO4) and sodium phosphate dibasic (Na_2HPO4) were purchased from Sigma-Aldrich.

HBS-P buffer (degassed 10 mM HEPES buffered saline, pH 7.4, 150 mM NaCl, 0.005% (v/v) surfactant P-20 (equivalent to Tween®20)) was kindly provided by Biacore (Uppsala, Sweden). Eluent buffer refers to HBS-P buffer adding 50 μM EDTA and 0.1% (v/w) DM. EDTA regeneration buffer refers to 0.01 M phosphate buffer, 0.15 M NaCl, 0.35 M EDTA, 0.05% (v/v) Tween®20, pH 8.3.

6.3 Different Tags and Different Coupling Ways

Coupling mechanisms	Supramolecular structure	Angular shift after coupling
His-tag	1.Au/Carboxyl SAM/NTA ligand/Ni^{2+}/His-tagged LHCII	0.5°
	2.Au/Biotin SAM/Streptavidin/Biotin-X-NTA/Ni^{2+}/His-tagged LHCII	0.76°
	3.Au/NTA SAM/Ni^{2+}/His-tagged LHCII	0.5°
	4.Au/Biotin SAM/Streptavidin/Biotinylated anti-6his IgG/His-tagged LHCII	0.3°
	5.Au/SiO_2/Ni-NTA AP conjugate/His-tagged LHCII	≤0.1°
	6.Au/Polystyrene/ Ni-NTA AP conjugate/His-tagged LHCII	≤0.1°
Strep-tag	7.Au/Biotin SAM/Streptavidin/Strep-tagged LHCII	0.1°
	8.Au/SCWP/rSbsB-HT/Strep-tagged LHCII	0.1°
Biotinylation	9.Au/Biotin SAM/Streptavidin/Biotinylated LHCII	0.5°
	10.Au/SCWP/rSbsB-HT/Biotinylated LHCII	0.9°
Covalent binding	11.Au/Carboxyl SAM/NH_2-LHCII	N/A
	12.Au/ Biotin SAM/Streptavidin/SH-LHCII	N/A
Lipid and membrane	13.Au/Biotin SAM/SA/LHCII included Biotinylated PEG proteo-liposome	N/A
	14.Au/Biotin SAM/SA/LHCII incorporated lipid bilayer membrane	N/A

Table 6.3: Different coupling ways to immobilize LHCII on the gold surface

All the coupling ways telled are listed in table 6.3, according to the different binding mechanisms. Several issues need to be pointed out before discussion.

O'Shannessey[122] tested three buffers (Tris, HEPES, phosphate) and concluded that HEPES buffer gave the best reproducible and sensitive results for the binding on Biacore's NTA sensor chip. In our study, different buffers including HEPES, Tris, MOPS, phosphate have been adopted for the investigation of the LHCII binding on the surface. No clear evidence was found that one special buffer gave better performance than the others. In general, necessary requirements for the buffer to be used are a neutral pH value (6-8) to simulate native environment for LHCII, some amount of a non-ionic detergent to maintain the proper folding of this membrane protein, and excluding high concentrations of Mg^{2+} to avoid aggregation of chlorophylls[123]. Moreover, when dealing with silver chips special for blue laser excitation, a low ionic strength buffer was utilized in order to prevent from etching the silver.

All "Biotin SAMs" mentioned in table 6.3 refer to a biotinylated SAM surface ($\chi = 0.1$) which has been optimized by Spinke *et al.*[49] for maximum streptavidin binding density. Just as "Biotin SAM", "Carboxyl SAM" and "NTA SAM" are surface self-assembled monolayers of a thiol with carboxyl-end headgroup or nitrilo-triacetic-end headgroup respectively, co-assembled with a hydroxyl-terminated spacer thiol. The ratio of the functional thiol, χ, in the binary mixed thiol solution was always 0.1 except for the "NTA SAM" situation, which will be fully explained in Section 6.7. The concentration of the binary mixed thiol solution was 1 mM unless otherwise mentioned, and the self-assembly process usually lasted for 24 hours, referring to the summary of Ulman[42].

6.3.1 His-tag

The use of short affinity tails for the recombinant production and purification of proteins has gained widespread application in biotechnology. At present, the 6×His-tag, which can bind to immobilized metal chelates, is predominantly used for the purification of recombinant proteins. Yet, the specificity of the binding interactions mediated by transition metal ions is limited so that the chromatography conditions must be optimized and delicate proteins are not routinely isolated in their native state[124]. The supramolecular structures 1-6 in Table 6.3 are based on this technique. A full description about the immobilization of his-tagged LHCII will be presented in Section 6.4.

Among them, the structures 5 and 6 are constructed by the physical adsorption of Ni-NTA conjugates on SiO_2 surface or polystyrene surface. Ni-NTA conjugates consist of Ni-NTA coupled to calf intestinal alkaline phosphatase (Ni-NTA AP conjugate) or horseradish peroxidase (Ni-NTA HRP conjugate). They can be used for direct, straightforward detection of any recombinant protein with an accessible 6×His-tag in a simplified procedure. Noji and co-workers[125] used Ni-NTA HRP conjugate covered glass surface to couple a biotinylated, polyhistidine-tagged F_1-ATPase $\alpha_3\beta_3\gamma$ subcomplex, observing the rotation of γ-subunit by fluorescent microscopy. Here we adopted a novel sol-gel technique (cf. Section 3.2.4) to synthesize stable silicon dioxide (silica, SiO_2) films on noble metals layers. Hydrophobic polystyrene is the most common material for solid phase immunoassay. It can be treated as a substitute for SiO_2 due to the passive adsorption mechanism, A 10 nm thick polystyrene layer was formed onto the gold surface via spin coating (cf. Section 3.2.3). The polystyrene surface was usually pretreated with glutaraldehyde in order to increase the adsorption efficiency[126].

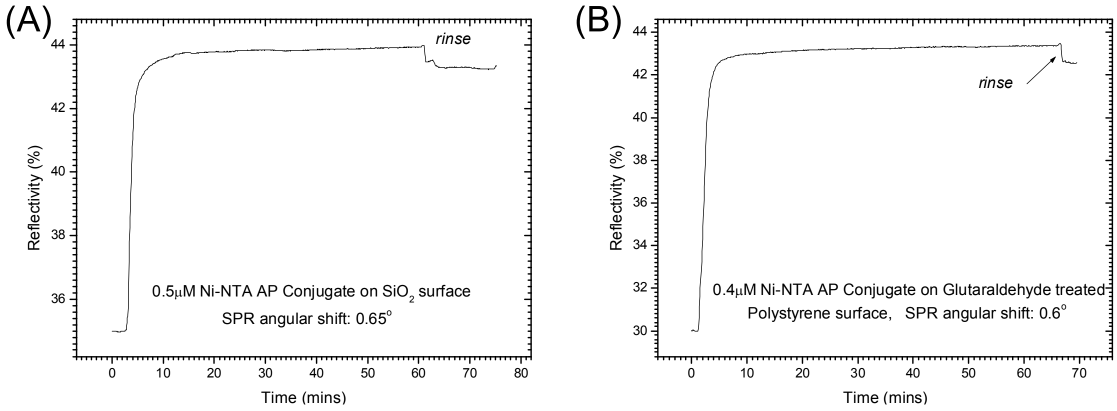

Figure 6.10: The passive adsorption of Ni-NTA Conjugate on SiO_2 surface (A) and glutaraldehyde treated polystyrene surface (B).

Although the adsorption of Ni-NTA AP conjugates was quite high both on SiO_2 and on polystyrene (cf. Figure 6.10), the further binding of monomeric Hu4 was weak (cf. Table 6.3), which was attributed to steric hindrance caused by the random orientation of physically adsorbed Ni-NTA AP conjugates. This was not a big issue for Noji's single molecular motor study as the rotation requires some degree of separation between neighboring subcomplexes, whereas in the energy transfer study, a high protein density is demanded. Moreover, the blocking reagents, *e.g.* BSA, routinely used in passive immobilization, will increase the complexity of the whole system.

6.3.2 Strep-tag

The Strep-tag technique, the basis of the supramolecular structures 7 and 8 in Table 6.3, showing more direct and robust performance compared with the his-tag method, was created by Schmidt and co-workers[127]. The Strep-tag, a nine-amino acid peptide (AWRHPQFGG), was selected from a genetic fusion peptide library for its ability to bind to streptavidin in a specific and reversible manner. Employing a synthetic peptide spot assay, the variant Strep-tag II was screened, which did not have the limitation of being only fused to the C-terminus of recombinant proteins[128]. The compromise that the affinity of the Strep-tag II for streptavidin is slightly weaker than that of the original Strep-tag can be overcome by using Strep-Tactin, a substitute for streptavidin with slight sequence differences[129]. The principle of the Strep-tag purification technique is quite simple. Tetrameric streptavidin is attached to a solid support first. A cell extract with the Strep-tag or Strep-tag II fusion protein is passed over the column with the fusion protein being complexed at the ligand pocket of streptavidin while other constitutes will be quickly washed out. The recombinant protein is competitively displaced by desthiobiotin, an inexpensive and chemically stable derivative of biotin, at physiological buffer conditions afterwards. Finally, the purification is completed after the streptavidin column is regenerated by HABA (2-(4'-hydroxyphenylazo)benzoic acid) rinse followed by a fast kinetics eluent rinse process[130].

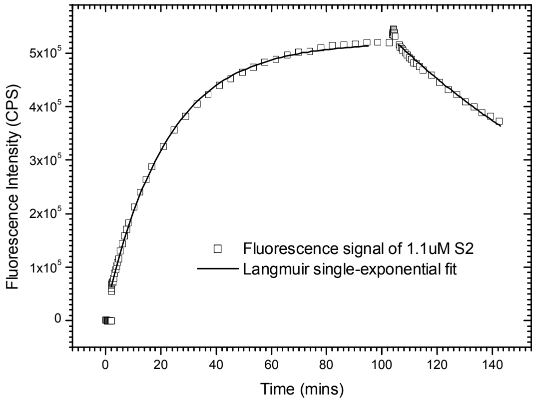

Figure 6.11: Fluorescence binding curve S2 on streptavidin surface and its Langmuir kinetics fit.

The main disadvantage of employing this affinity chromatographic technique to LHCII binding is the comparatively weak affinity. The affinities for Strep-tag and Strep-tag II were measured by isothemal titration calorimetry with the synthetic peptides and recombinant core streptavidin, revealing K_D values of 37 µM and 72 µM, respectively[128]. SPFS as a sensitive biosensor was used to determine the binding kinetics between monomeric S2 and surface coupled streptavidin (cf. supramolecular structure 7 in Table 6.3). Only the fluorescence signal channel was used for the kinetics analysis (cf. Section 2.3) due to the small change in reflectivity. The final result of K_D = 0.29 µM (cf. Figure 6.11) was comparable to the equilibrium dissociation constant (0.58 µM) of alkaline phosphatase-strep tag fusion protein and immobilized streptavidin on an IAsys optical biosensor[131]. The significant contrast between the biosensor results and the calorimetric results might come from the difference between a "surface" and a "solution" affinity reaction.

6.3.3 Biotinylation

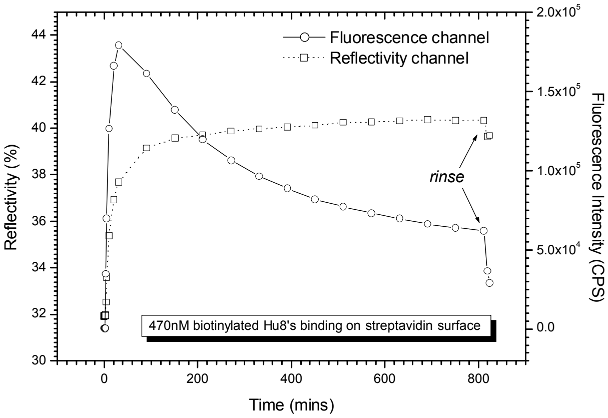

Figure 6.12: Kinetic working curve of H8B on streptavidin surface.

The supramolecular structures 9 and 10 in Table 6.3 are based on biotinylation. As mentioned in Section 6.2, biotinylation was done at the N-terminus of LHCP via biotin-NHS ester. Although the mass change caused by the biotinylated LHCII (usually biotinylated Hu8, abbreviated as H8B) binding was pronounced compared with other methods, the record of the fluorescence channel gave unsatisfactory results. Take H8B's immobilization on streptavidin as an example (cf. Figure 6.12), the incubation in eluent buffer (0.01 M Hepes, pH 7.4, 0.15 M NaCl, 50 μM EDTA, 0.005% P-20, 0.1% (w/v) DM) for about 800 minutes resulted in an angular shift as high as 0.5^{o} (cf. Table 6.3), but the fluorescence signal quickly trailed off following the short peak after 30 minutes of sample injection. Generally, the reflectivity response and the fluorescence response of bound LHCIIs are uncorrelated to some degree, which might be the signature of structure instability of membrane proteins outside their natural thylakoid membrane. However, the strong slope of the fluorescent signal's decrease here may be attributed to conformational changes of the protein structure itself induced by biotinylation. This hypothesis was explained by Von Grunigen[132] and Peter[133] in their studies of biotinylated peptide-antibody interactions. In fact, this could be confirmed by the occurrence of an emergent shoulder at λ = 650 nm in biotinylated LHCII's fluorescence emission spectrum in solution (data not shown), implying the loss of biological activities.

6.3.4 Other Methods

The supramolecular structures 11 and 12 in Table 6.3 are based on covalent bonds. Structure 11 is associated with activating surface carboxyl groups by EDC/NHS chemistry to form NHS-esters, and further immobilization of ligands rich in amino- or hydrazine groups. Structure 12 follows IAsys's "Thiol coupling to avidin" protocol[134], which describes a method for immobilization of proteins through available surface thiol groups to a dense avidin layer (streptavidin in our case) by a thiol exchange reaction via SPDP (N-Succinimidyl 3-[2-pyridylditho] propionate). Although these two methods are typical ways to immobilize proteins with amino groups or thiol groups, they are not suitable for the coupling of this delicate LHCII. Its conformation will be influenced by direct fixation (as the biotinylation mentioned above) and its biological characteristics will be highly impaired by the electrostatic modification induced by using an acidic buffer with a pH value lower than the protein's isoelectronic point, a necessary step for the proteins' surface enrichment to facilitate the subsequent immobilization.

The supramolecular structures 13 and 14 in Table 6.3 are related to membrane architecture, which will be fully discussed in Section 6.7.

6.3.5 Summary

In general, the first step in the interaction analysis is the immobilization of one of the interactants on the sensor chip surface. This immobilization can be permanent in the form of a covalent bond or transient by means of capturing. The immobilization technique used depends on the ligand type, the analyte to be used and the purpose of the study.

For investigations of the interactions between neighboring LHCIIs, the focus of interest is the lateral communication. As pointed out in 2.2.2, the proximity of the donor and the acceptor molecules is crucial because the efficiency of the energy transfer is inversely proportional to the sixth power of the distance separating the two molecules. Therefore the primary requirement for LHCII immobilization should be the highest complexes surface density, which guarantees an effective resonance energy transfer. As seen in Table 6.3, only the His-tag method and biotinylation method meet this requirement. Another indispensable prerequisite is that the biological activity of the immobilized antenna complexes should be retained to the highest possible degree. This rules out the biotinylation method, leaving the His-tag method as the only appropriate way for energy transfer studies.

6.4 IMAC and Home-Made His-tag Chelating Chips

6.4.1 IMAC Introduction

In the mid 1970s, Porath et al.[135] introduced a new type of chromatography which was first designated “metal chelate chromatography”, but was later termed “immobilized metal (ion) affinity chromatography” (IMAC). The technique is based on differences in the affinity of proteins for metal ions bound to metal-chelating groups which are immobilized on a chromatographic support (resin). The best known improvement is the application of histidine tags for the separation of recombinant polypeptides[136]. This approach consists of the insertion of a short tail of histidine residues on either the N- or C-terminus of a protein or peptide. The use of such histidine and other metal affinity tags proved to be a powerful tool for protein recovery, as a result, IMAC emerged as one of the major preparative methodologies used for protein purification.

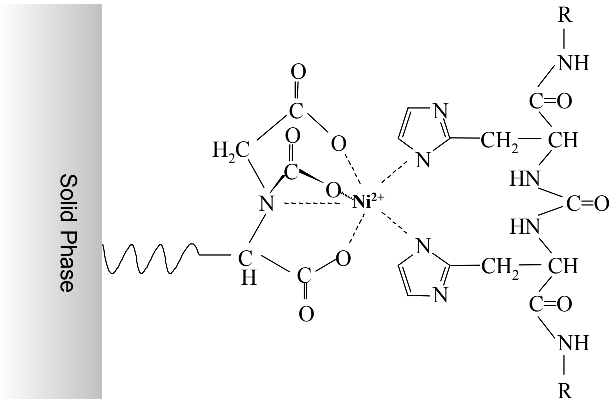

Figure 6.13: Schematic diagram of interaction between neighboring residues in 6×His tag-Ni-NTA IMAC.

Binding of proteins (or peptides) to metal ions is based on the interaction between an electron-donating group present on a protein surface and a metal ion, presenting one or more accessible coordination sites, strongly held by multidentate chelators on the solid phase column matrix. Proteins, transition metal ions and chelating compounds, as three indispensable components, construct a stable supramolecular hierarchy in IMAC (cf. Figure 6.13). Among Co^{2+}, Zn^{2+}, Ni^{2+} and Cu^{2+}, which are considered as “borderline acids” in Pearson’s HSAB (hard and soft acids and bases) theory[137], following the ascending sequence in protein retention strength as chelated by iminodiacetic acid (IDA)[138], Ni^{2+} has been found to be a good choice of metal ion since it has six coordination sites for bonding[136] and comparatively high protein retention ability. However, too high a retention could also lead to an increased adsorption of impurities[139]. Among the choices for a chelator, IDA, binding to Ni^{2+} with two carboxylate oxygens and one nitrogen atom, allowing three free coordination sites for the protein coupling on metal ion, and the tetradentate nitrilotriacetic acid (NTA), which binds to Ni^{2+} with three carboxyl groups and one nitrogen, leaven two coordination sites free for the proteins, are standard and most commonly used. On the protein side, it is widely accepted that histidine and cysteine residues display a strong metal affinity, largely attributed to their functional groups of imidazole and thiol, respectively, but the retention ability of the latter is somewhat lower than that of the former. Generally, a string of six histidines is found to produce a strong and specific binding to Ni^{2+} when it is held by NTA, replacing the two water molecules on the Ni with histidines[140]. Although the dissociation constant of 6×His-tagged proteins to Ni-NTA has been measured to be 10^{-13} M at pH 8[141], other factors including amino acid sequences, their foldings, and surface properties also contribute profoundly toward the real value[139].

The protein immobilization on Ni-NTA is highly specific and fully reversible upon the addition of competing compounds (like imidazoles or histidines) in neutral pH buffer[142]. Reprotonation of the nitrogens in the histidine residues under elution conditions at low pH value below the pK_a of histidine is another way to reverse binding[141], however, these harsh conditions often denature the proteins. Alternatively, the protein can be eluted by a chelating compound such as EDTA (ethylenediamine tetraacetic acid), but the elution will strip off all proteins retained along with the metal ion used[143,144].

Another interesting property of the interaction of 6×His with Ni-NTA is the fact that it is virtually unaffected by high salt (up to 1M), nonionic detergents (Triton X-100 or Tween 20 up to 1%), organic solvents, ethanol or glycerol up to 30%, reducing agents (β-mercaptoethanol up to 10 mM) or highly denaturing conditions such as 8 M urea or 6 M guanidine hydrochloride, guaranteeing the robustness of the supramolecular structure[145].

This supramolecular structure can recognize specifically only a His-tagged protein through the nickel ion chelated with NTA in the solid phase. Thus, this technique is useful for the immobilization of His-tag proteins for studies using SPR. The crucial procedure is the immobilization of NTA containing compounds on the gold surface. In most studies with His-tagged proteins, the Biacore's Sensor Chip NTA was the preferred choice. For example, Nakamura *et al.* designed a herbicides assay using a self-assembled photosynthetic reaction center from the purple bacterium on a Biacore's Sensor Chip NTA[118]. In fact, the Biacore's Sensor Chip NTA uses a covalent attachment a Ni-NTA group in the solid phase, as it was fully clarified by Gershon and Khilko[146] in their studies of the interaction between surface-coupled 6His-VP55 and VP39 on the Biacore CM5 chip via a NTA ligand. In their studies of surface-oriented ferredoxin:NADP+ reductase, Madoz-Gúrpide *et al.* covalently coupled a mixture of ANTA together with ethanolamine through amidation of a NHS-esters of a dithioactic acid SAM[147]. Wegner *et al.* reported the way using the heterobifuncional linker N-succinimidyl S-acetylthiopropionate (SATP) to generate reactive sulfhydryl-terminated surfaces on amine-terminated SAMs, then creating a capture monolayer for His-tagged protein arrays' fabrication by reacting maleimide-NTA molecules with sulfhydryl surface[148]. On the other hand, Sigal *et al.*[48] gave a more direct way for NTA functionalization on the gold surface by means of a home-synthesized NTA-thiol. The SAM mixture was prepared with a alkanethiols couple: one has a NTA group which forms a tetravalent chelate with a nickel ion, the other has a tri(ethyleneglycol) group which is capable of avoiding non specific adsorption of protein. They proved that His-tagged proteins adsorbed on the NTA-SAM retained a greater ability to participate in binding interactions with proteins in solution than proteins immobilized in a thin dextran gel layer by covalent coupling. Apart from the above strategies, chelator lipids were also developed to achieve surface NTA functionalization[149-151].

In this work, four different architectures have been exploited for the fabrication of home-made His-tag chelating chips. A schematic description of the detailed supramolecular structures of these chips is presented in Figure 6.14.

6.4.2 His-tag chelating chip A

The His-tag chelating chip A goes back to Biacore's Sensor Chip NTA except that the latter is constructed as a three dimensional dextran matrix while the former is built up on a planar carboxyl SAM surface with the thiol couple 11-mercaptoundecanoic acid and 11-mercapto-1-undecanol. A typical surface activation and binding diagram is shown in Figure 6.15. The SAM surface was activated with a fresh mixture of 0.4 M EDC and 0.1 M NHS in a 1:1 (v/v) ratio for 10 minutes, forming the terminal NHS ester moieties ((1) in Figure 6.15). 5 mM AB-NTA solution prepared in HEPES-NaOH buffer (100 mM HEPES, pH 8.5) was injected into the flow cell and incubated with the surface for 30 minutes ((2) in Figure 6.15). Unreacted active groups were passivated by an injection of 1M ethanolamine solution (pH 8.5) for 20 minutes ((3) in Figure 6.15). The surface was further activated with 500 μM $NiCl_2$ prepared in HBS-P buffer for 10 minutes ((4) in Figure 6.15). Finally, LHCII immobilization was performed with a injection of 0.22 μM monomeric C3 (abbreviated as Mon-C3) in eluent buffer for 20 minutes, followed by a fresh buffer rinse, characterized by the reflectivity and the fluorescence channels simultaneously ((5) in Figure 6.15).

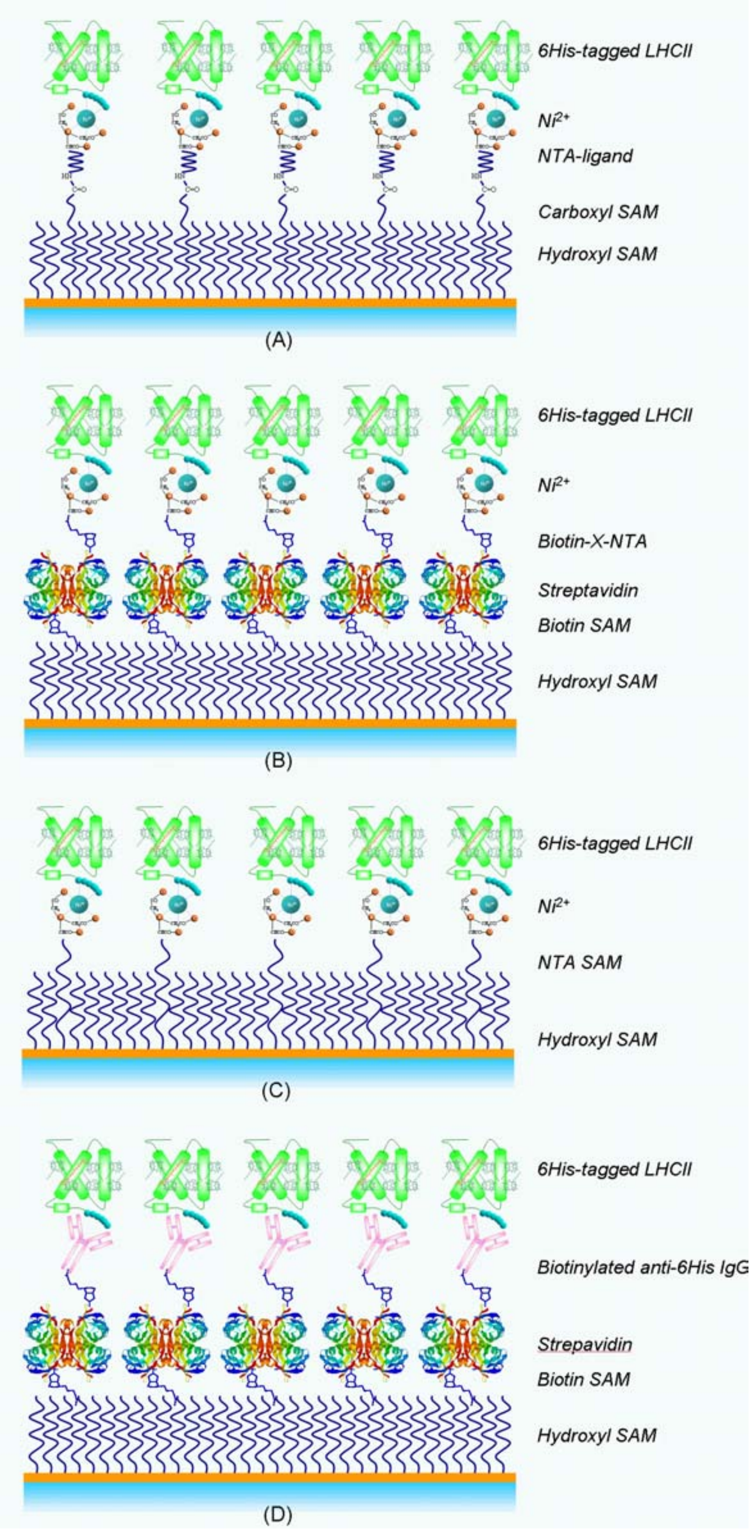

Figure 6.14: Supramolecular structures of four kinds of home-made His-tag chelating chips.

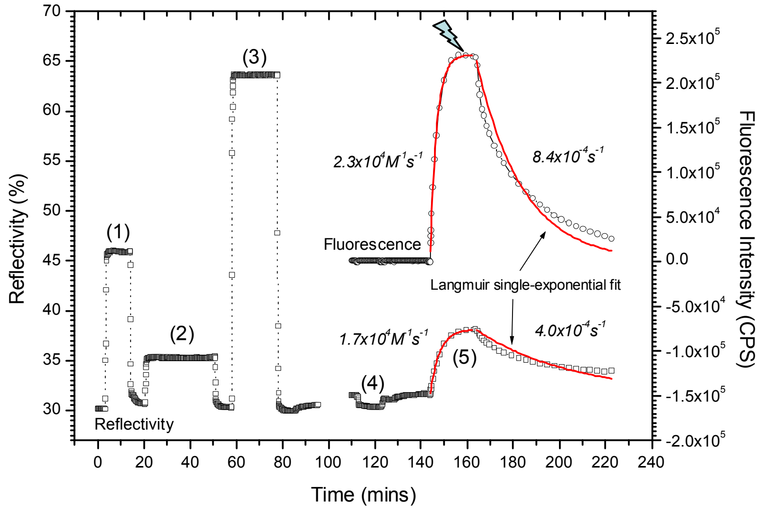

Figure 6.15: Surface activation and Mon-C3's coupling on His-tag chelating chip A.

Three features are noteworthy. Firstly, since AB-NTA has a molecular weight of only 324.25 Da, the direct reflectivity analysis was virtually impossible, making it hard to judge the degree of surface chelator functionalization quantitatively. Secondly, both the dissociation process of the reflectivity signal and that of the fluorescence signal could not be well resolved by a Langmuir single-exponential kinetic model, suggesting the complexity of the His-tagged proteins binding to the Ni-NTA surface. Roughly, the dissociation constant could be estimated to be K_D = 2.4~3.7×10^{-8} M. Thirdly, k_{off} values obtained from the reflectivity signal was only half of the value obtained from the fluorescence signal (cf. Figure 6.15), indicating a faster decrease of LHCII fluorescence upon rinse than the pure mass dissociation. This correlated with the fluorescence decrease after the equilibrium (indicated as a lightning bolt label in Figure 6.15) mentioned in Section 6.3.3.

6.4.3 His-tag chelating chip B

McMahan and Burgess[152] invented a one-step method to synthesize biotinylated NTA, using it for the detection of His-tagged proteins immobilized on nitrocellulose. Such a compound named Biotin-X-NTA is commercially available from Molecular Probes and was use for the His-tag chelating chip B.

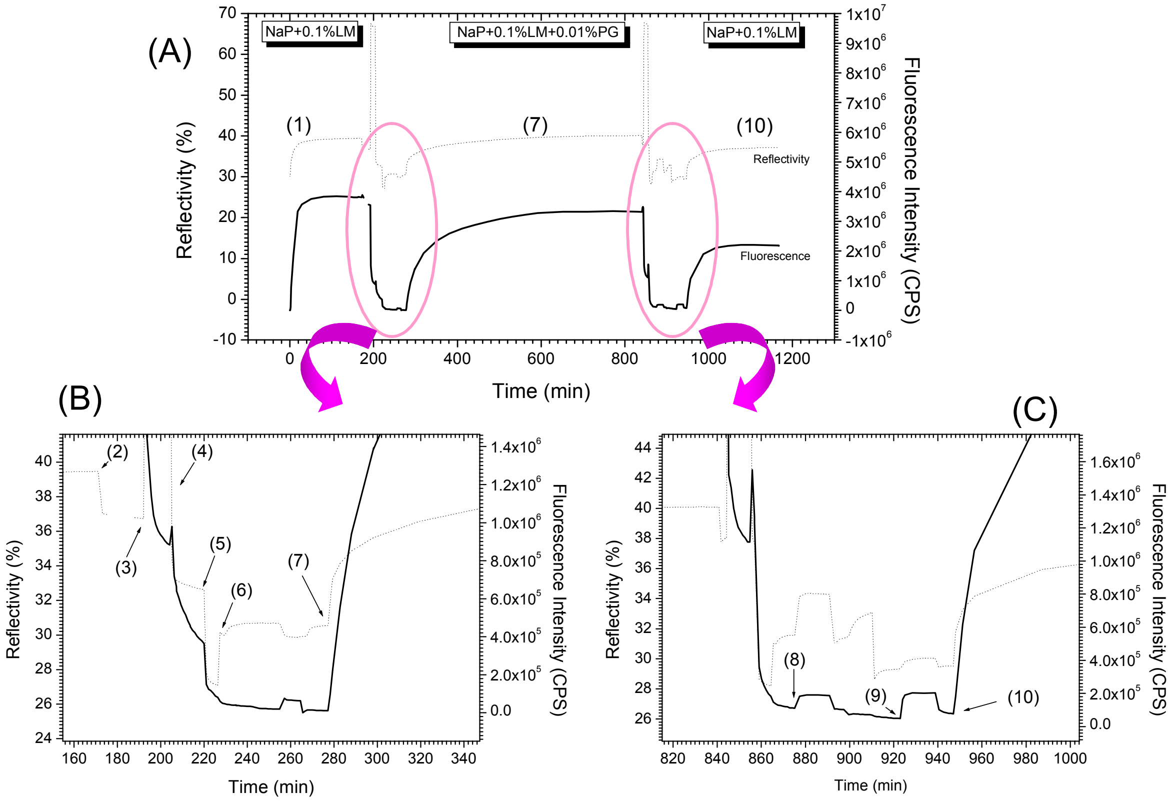

Figure 6.16: Tri-C3's coupling on His-tag chelating chip B. (A) Kinetic working curve. (B) Amplification of the regeneration part in (A). (C) Amplification of the control proteins' adsorption part in (A).

In this method, the surface NTA functionalization was achieved by the circulation of a 1 μM Biotin-X-NTA solution for 30 minutes on a biotin SAM (χ = 0.1) supported streptavidin surface. Following 10 minutes of metal ion activation with 500 μM $NiCl_2$, the flow cell was rinsed with NaP+DM buffer (50 mM sodium phosphate, pH 7.4, 0.1% (w/v) DM), ready for protein immobilization. 0.2 μM C3 trimers (abbreviated as Tri-C3) prepared in NaP+DM buffer was injected into the flow cell and incubated stilly for ca. 170 minutes until the fluorescence decrease occurred ((1) in Figure 6.16 (A), all numbers in bracket in this section match with the corresponding steps in Figure 6.16). After rinse with NaP+DM buffer (2), EDTA regeneration buffer was injected and circulated for 10 minutes (3), followed by fresh buffer rinse (4). Both the fluorescence signal and the reflectivity signal decreased substantially, however, they still remained at the level far from their original baseline. This is understandable since stripping off nickel ions via EDTA also removed part of the Mg^{2+} from the LHCII, denaturing the complex and resulting in the aggregation of unfolded proteins as well as pigments on the surface by non specific adsorption. That's why Ferguson *et al.*[153] in their study of the interaction of σ^{70} with E. coli RNA polymerase core enzyme suggested a four-step regeneration procedure including 0.3 M imidazole, EDTA regeneration buffer from Biacore, 0.5% SDS and 1 M NaOH. In our study, 10 minutes of rinse with 0.5% SDS (5) was enough for the complete regeneration. The baseline after exchanging with NaP+DM buffer (6) resulted in a clean surface without unfolded species or fluorescent impurities.

The surface was nickel activated again and rinsed with NaP+DM+PG buffer (NaP+DM buffer adding 0.01% (w/v) phosphatidyl glycerol) for the second turn of protein immobilization. The flow cell was filled with 0.2 μM Tri-C3 again but prepared in NaP+DM+PG buffer (7). 9 hours of incubation produced almost the same mass change while about 85% of the fluorescence intensity of the first coupling was reached. One should mentioned that there was some difference in the association kinetics due to the existence of PG lipid in the second time, which will be further discussed in Section 6.5.

After regeneration with EDTA and SDS, 0.2 μM Tri-C3 in NaP+DM+PG buffer was directly injected in the flow cell for 10 minutes (8) without metal ion activation. As expected, there was only a refractive index change in the SPR channel and the fluorescence background jump caused by chromophores in the bulk solution excited by the evanescent field tail. Afterwards, nickel ions were introduced in the loop again, followed by an injection of 0.4 μM monomeric H8B as the control protein in NaP+DM buffer (9). Waiting for 10 minutes produced the same background jump as in (8) This was the anticipated result with H8B which lacks the 6×His-tag. Finally, the loop was rinsed with NaP+DM and filled with 0.2 μM Tri-C3 in NaP+DM buffer (10), which resulted in strong LHCII immobilization comparing with the above two control experiments, although the fluorescence equilibrium peak had decreased to 60% of the original value because this was already the third binding reaction after two regeneration cycles.

This study demonstrated the excellent performance of our home-made His-tag chelating chip B, proving the specificity of the His-tag/Ni-NTA interaction realized on SPFS biosensors.

6.4.4 His-tag chelating chip C

The His-tag chelating chip C follows the principle of direct chelator functionalization on the gold surface via a binary SAM, composed of NTA terminated OEG thiol and OEG spacer thiol. It is the simplest way for NTA functionalization, minimizing unwanted interactions between the LHCII and other additional surface components that would increase the complexity of the supramolecular structure. Further His-tagged protein immobilization can be easily controlled by the mixing ratio of the thiol couple. At the same time, the OEG-terminated SAM is known for its protein resistance due to a tightly bound layer of interphase water[154], which greatly minimizes non specific adsorption. In our case, the only drawback of this surface modification strategy is the proximity of the LHCII bound pigments to the metal surface, the main reason for surface fluorescence quenching. Due to the fact that the focus of this study is not on the sensitivity investigation, this is still one of the best candidates for energy transfer research for its handling convenience.

A full demonstration of the LHCII immobilization is shown in Figure 6.17 (A), which is also a special example for an energy transfer study fully discussed in Section 6.9. In this experiment, the NTA SAM ($\chi = 0.4$) was built up on a gold protected silver chip. After the nickel ion activation, a series of complexes including different ratios of Tri-Hu10 and Tri-Hu10-DY-730 with the fixed concentration of 1μM prepared in NaP+DM buffer (20 mM sodium phosphate, pH 7.4, 0.1% (w/v) DM) were introduced into the flow cell in separate cycles. For each cycle, the reconstituted complex solution was incubated in the loop for 30 minutes, followed by buffer rinse as well as routine EDTA and SDS regeneration. An ideal regeneration should completely remove any bound analyte from the surface, while maintaining the activity of the ligand. In our case, on the one hand, the baseline after every cycle stabilized at a response close to the starting level, indicating the absence of any protein accumulation. Moreover, the mass change on the surface at each cycle, expressed as the corresponding SPR angular shift, was almost the same, implying little loss of surface functionality. This argument was also contributed by the surface fluorescence emission spectrum recorded in the optical spectrometer at every cycle's reflectivity peak. Even after three regenerations, the overall area integration of the fluorescence spectrum was still 80% of the original value (cf. Figure 6.17 (B)), better than the performance of His-tag chelating chip B. In fact, one can imagine that the simpler the supramolecular configuration, the more stable is its function. The pure SAM structure should be better than some additional protein scaffold built upon it.

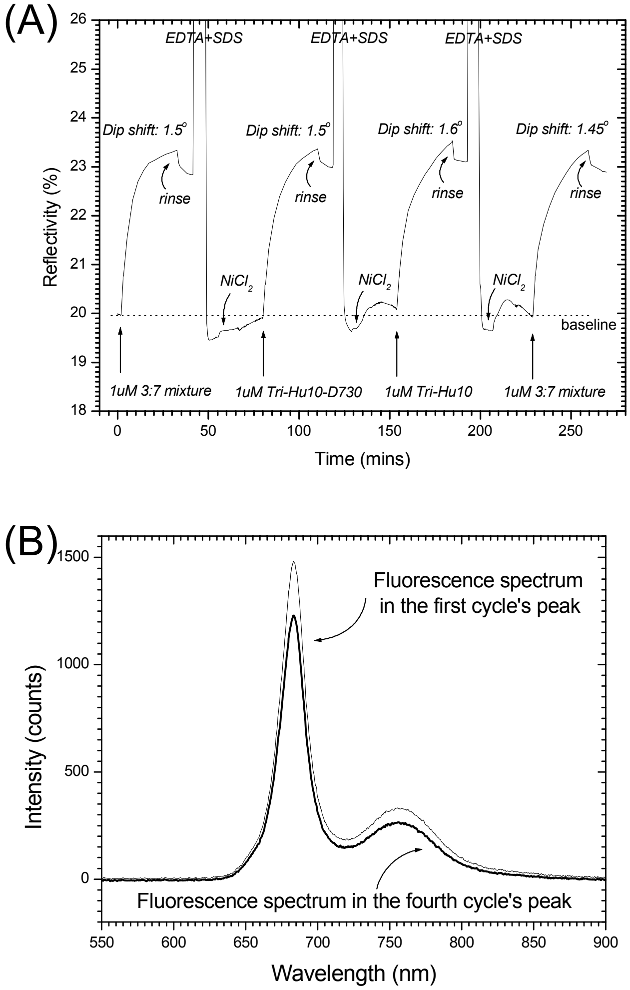

Figure 6.17: The performance of His-tag chelating chip C under the excitation of Nd:YAG DPSS laser. (A) Kinetic reflectivity working curve. (B) Surface fluorescence emission spectra comparison in the first cycle and in the fourth cycle.

6.4.5 His-tag chelating chip D

Although the IMAC is prevalent in His-tagged protein purification, in certain cases for which the protein of interest is present only as a small fraction or for which a very high purity is needed, there is a clear demand for a second purification step, for example, the anti-His-tag immunoaffinity chromatography[155] that provides another strategy for LHCII immobilization. In the His-tag chelating chip D, biotinylated anti-6His-tag IgG molecules are immobilized instead of the Ni^{2+}-NTA components in the His-tag chelating chip B. The surface activation course is plotted in Figure 6.18 (A) except that the streptavidin was replaced by avidin/biotinylated anti-avidin/avidin, which will be explained in Section 6.6. Anyway, 10 μg/ml biotinylated anti-6His-tag IgG was introduced and circulated in the flow cell for 30 minutes, resulting in a surface IgG density of 2.9 ng/mm^2. The following coupling process of 0.3 μM Tri-Hu10 in NaP+DM buffer (20 mM sodium phosphate, pH 7.4, 0.1% (w/v) DM) is shown in Figure 6.18 (B). Glycine buffer (10 mM Glycine-HCl, pH 1.75) was chosen as the regeneration buffer to break the hydrogen bonds between the antibodies and the antigens. After three pulses of Glycine buffer injection for 3 minutes each, the flow cell was rinsed with fresh buffer and the second cycle of protein coupling began. Scrutinizing details of this plot, one can find the remaining fluorescence signal, indicating that the regeneration was not thorough enough. In general, the exhaustive regeneration of LHCII coupling is time-consuming and needs to be carefully optimized. Although chelating agents such as EDTA will not interfere with the binding this time due to different mechanisms, imidazole can still act as a competitor of the analyte, which is another strategy for regeneration.

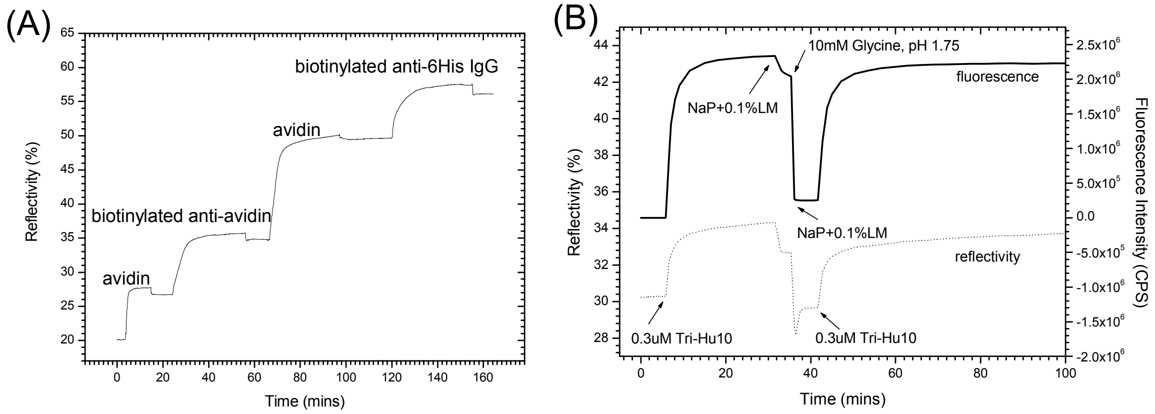

Figure 6.18: The performance of His-tag chelating chip D. (A) Surface activation by avidin, biotinylated anti-avidin, avidin and biotinylated anti-6His-tag IgG. (B) Kinetic working curve of Tri-Hu10's coupling.

6.5 Stability of Surface Anchored LHCII

A prerequisite for utilizing LHCII for device application is the requirement to immobilize the protein on the surface while retaining its natural function. A biologically active reconstituted LHCII complex should have the properties of intra-complex energy transfer from Chl *b* to Chl *a*, which will be presented in the steady-state fluorescence as a Chl *a* emission spectrum with virtually no contribution from Chl *b* with excitation of Chl *b* at $\lambda = 460$ nm[114]. On the contrary, a gradual complex denaturation will be reflected in the fluorescence emission spectrum as the emergence of a Chl *b* emission shoulder at $\lambda = 650$ nm and the concomitant decrease in Chl *a* emission at $\lambda = 680$ nm. While on the surface, this denaturation will be displayed as a continuous fluorescence decrease recorded by SPFS.

There are many factors that influence the stability of the antenna complex in its surface coupling process. Among them, the most important ones are ingredients of the preparing cocktail buffer, including sucrose, detergent as well as lipids from thylakoids, the oligomeric state of the complex, temperature, the circulation rate *etc.*.

6.5.1 Sucrose

Osmolytes such as sugars, methylamines, and amino acids have long been reported[156,157] to increase the thermodynamic conformational stability of proteins, shifting the equilibrium between native and denatured states to favor the native state. That's why in the reconstitution protocol (cf. Section 3.3), 0.4 M sucrose is added before isopycnic centrifugation. While sucrose has a positive influence upon LHCII in solution, it causes severe detuning effect for the SPFS detection due to its refractive index effect. It is even impossible to prepare similar concentration of sucrose in the immobilization buffer because one can not predict the sucrose concentrations of the proper LHCII bands in the density gradient column (cf. Section 3.3). In order to get correct SPFS signals, a compromise with the complexes stability has to be made in order to eliminate sucrose components from the reconstituted solution via ultracentrifugation.

6.5.2 Detergent

It is common sense that membrane proteins need detergents wrapped around their hydrophobic domains in order to maintain the correct folding in the reconstitution buffer, different from their natural lipid bilayer matrix *in vitro*. For LHCII, detergents most frequently used are 0.5% (w/v) CHAPS, 0.1% (w/v) Triton X-100 or 0.1% (w/v) DM. While these detergents have been generally reported to be compatible with LHCII in homogeneous situation, their performance on the surface together with the immobilization buffer remains almost unknown. Figure 6.19 (A) plots the baseline changes of HBS-P buffer together with different detergents at a circulation rate of 3.6 ml/min after surface functionalization. The gradual increase of the reflectivity signal for most detergents containing buffer apart from DM hints to non specific adsorption. In all immobilization experiments unless otherwise mentioned, 0.1% DM was used to solubilize the reconstituted antenna complex. Meanwhile, DM plays a role in preventing aggregated complexes from accumulating on the surface (cf. Figure 6.19 (B)), which even could not be stripped by using harsh regents like SDS or NaOH (data not shown).

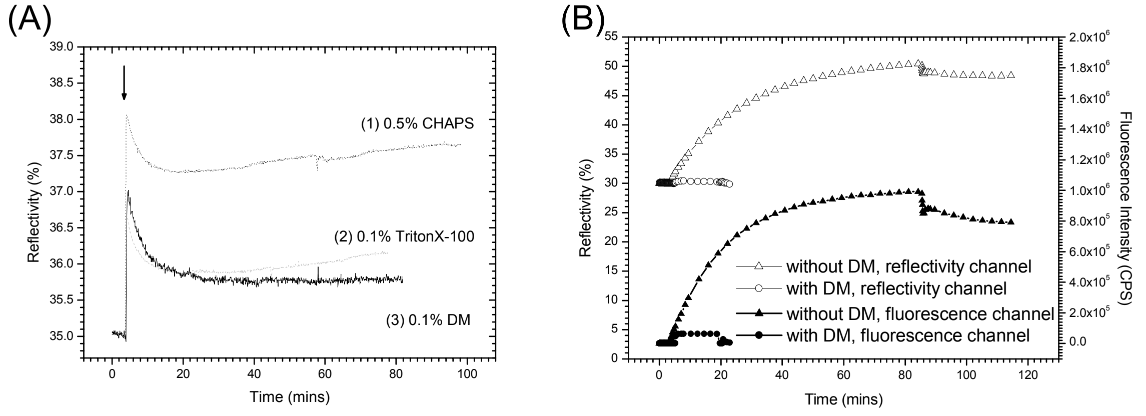

Figure 6.19: Choosing DM as the detergent to stabilize reconstituted LHCII. (A) Reflectivity changes using different detergents containing HBS-P buffer. Note the first spike (indicated by an arrow) after the buffer exchange came from the bulk refractive index change and temperature disturbance. (B) Comparisons of S1's non specific binding on carboxyl SAM in Eluent buffer (with DM) and HBS-P buffer (without DM).

6.5.3 Temperature

Besides the components of the preparation buffer, some extrinsic parameters, the temperature for example, also influence the stability of LHCII. Yang *et al.*[158] measured the thermal stability of LHCII by observing the decay kinetics of Chl *b*-sensitized Chl *a* fluorescence in a fluorimeter thermostated to 37°C, obtaining a lifetime of only 70.3±8.6 s for a wild-type complex, longer than all reconstituted complexes from mutant proteins. In a single molecule spectroscopic study on LHCII, Tietz *et al.*[119] proved that samples were stable for more than an hour at room temperature, but the stability increased dramatically to >1 day at temperature <77 K. These investigations demonstrated the importance of low temperature on stabilizing the complexes. SPFS fluorescence determination of surface bound LHCII at different temperatures (cf. Figure 6.20) gave similar conclusion, suggesting a strategy for prolonging of the fluorescence equilibrium via temperature controlling during the immobilization. However, for experimental convenience, other strategies were employed to improve the stability of LHCII on the surface instead of thermostating below room temperature.

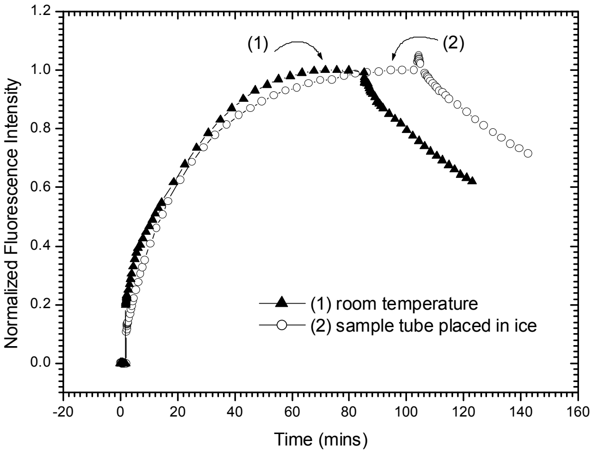

Figure 6.20: The influence of temperature upon the fluorescence stability of surface bound S2. (1) At room temperature. (2) Placed the sample tube in ice. The fluorescence intensity has been normalized for comparison. Peak point before fluorescence decrease is indicated by an arrow in both experiments.

6.5.4 Oligomerization

Trimers are thought to be the native form of LHCII in the photosynthetic membrane and, also, in mild detergent solution the trimeric form is preserved. Wentworth *et al.*[159] reported a detailed comparison between carefully prepared intact monomeric LHCII and LHCII trimers and confirmed that: first, trimers are more resistant to heat-induced denaturation than monomers, which makes the photosynthetic membrane more stable at high physiological temperatures; second, trimerization is necessary to optimize light harvesting. Thus, the trimeric complex is the general form of LHCII used in the coupling experiments except for some particular examples where trimerization is not possible with some special labels which interfere with the first 49 or 51 amino-acid residues of the polypeptide[111].

6.5.5 Lipid

In chloroplast thylakoid membranes of green plants, monogalactosyldiacylglycerol (MGDG) accounts for about 50% of the total lipid content. The membrane also contain digalactosyldiacylglycerol (DGDG) (≈ 30%), sulfoquinovosyldiacylglycerol (SQDG) (≈ 5-12%), and phosphatidylglycerol (PG) (≈ 5-12%)[160]. It was demonstrated[161] that lipids (in particular PG) are essential for the trimer formation of LHCII and treatment of trimeric LHCII with phospholipase A2 leads to a complete dissociation of the trimer into monomers. In addition, two lipids (PG), one detergent molecule and about 70 water molecules per monomer have been positioned by a recent work on the crystal structure of spinach LHCII trimer at 2.72 Å resoluion[111]. All of that suggests the function of PG as a stabilizing agent for LHCII, especially the trimers. Similarly, surface binding experiments by SPFS also detected a slower association kinetics ((7) in Figure 6.16) in a buffer with PG than that in buffer without PG ((1) and (10) in Figure 6.16), which delayed the onset of fluorescence decrease. The price of using PG in immobilization buffer is the long waiting time for surface saturation. Since there is no great difference between the equilibrium reached with lipid or without lipid (cf. Figure 6.16 (A)), the preparation buffer in this study normally lacks PG.

6.5.6 Circulation Rate

If membrane proteins exist in artificial conditions different from their natural environment (*e.g.* LHCII in reconstitution buffer), the whole system stays in a delicate balance. Because the interactions between the chlorophylls and the apoprotein are noncovalent, long time stirring, even slight, could destabilize the subtle equilibrium. Steady-state fluorescence emission measurements in solution (cf. Figure 6.21) revealed that the biological activity of most LHCII still preserved in the Eluent+PG buffer (Eluent buffer adding 0.01% (w/v) PG) after 14 hours' still incubation even at room temperature. However, the one measurement for which the sample was circulated in the flow cell for 14 hours totally lost its intra-energy transfer behavior, expressing an additional peak at ca. $\lambda =$ 650 nm. Accordingly, only still incubation was applied in all the immobilization experiments.

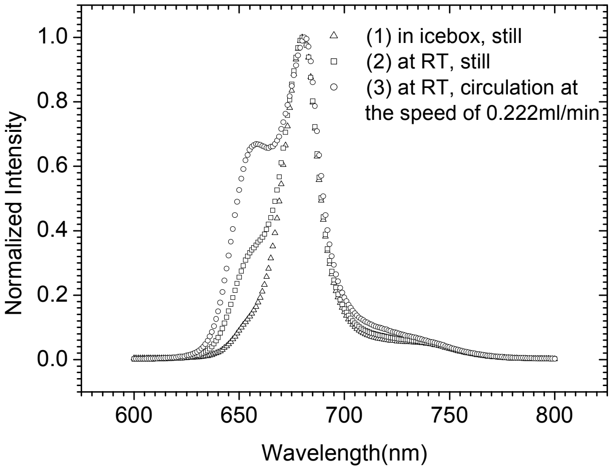

Figure 6.21: The influence of circulation on Tri-C3's fluorescence emission measurements under the Chl *b* -excitation at $\lambda =$ 460 nm in Eluent+PG buffer after 14 hours. (1) Still in icebox. (2) Still at room temperature (RT). (3) Circulated at the rate of 0.222 ml/min at RT.

6.5.7 Summary

Figure 6.22 (A) summaries the impact of factors like oligomerization, PG lipid and circulation rate on the stability of surface coupled reconstituted LHCII from the same clone. The stable equilibrium curves for nearly 14 hours on both the reflectivity channel and the fluorescence channel, as well as the maintained intra-energy transfer feature showed in the fluorescence emission spectrum on the chip (cf. Figure 6.22 (B)), suggest a perfect LHCII trimers' immobilization under the optimized conditions.

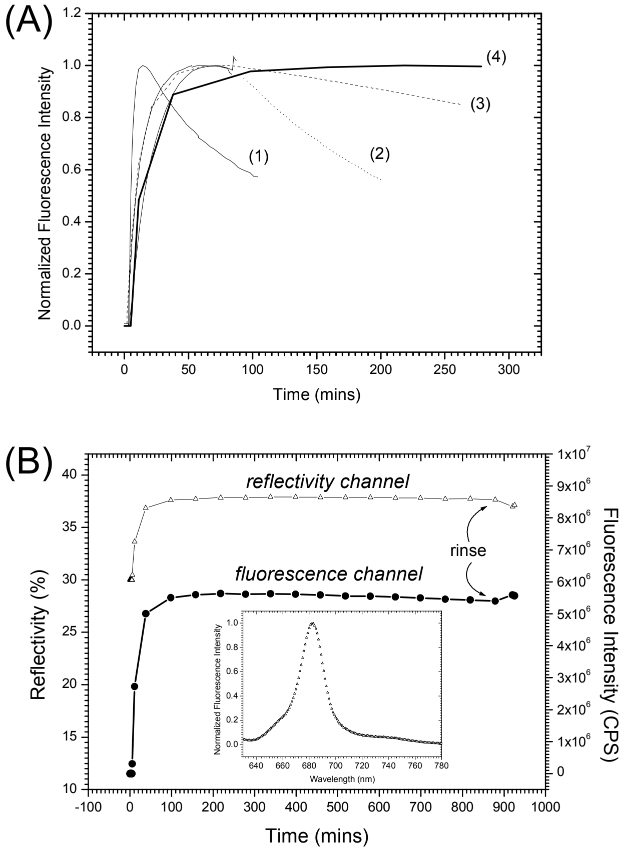

Figure 6.22: (A) The influence of oligomerization, PG and circulation rate on C3's coupling on Ni-NTA surface. (1) Mon-C3 in Eluent buffer at the circulation rate of 3.6 ml/min, (2) Tri-C3 in Eluent buffer at the circulation rate of 0.222 ml/min, (3) Tri-C3 in Eluent+PG buffer at the circulation rate of 0.222 ml/min, (4) Tri-C3 in Eluent+PG stilly incubated in the flow cell. (B) The whole kinetic working curve of (4) on home-made His-tag chelating chip B. The inset is the steady-state fluorescence measurement of the Chl *b*-stimulated fluorescence emission on the chip after 14 hours.

6.6 Layer-by-layer Structure – Interesting Episode

Although the disadvantage that LHCII bound pigments are strongly quenched can be ignored as mentioned in Section 6.4, a more advisable way is to overcome it. The typical method should be increasing the separating distance between LHCII and the metal layer via the development of multilayer films. There are mainly two kinds of principle for the construction[162], one is based on the electrostatic attraction between opposite charges which will induce a strong non specific adsorption during the process. The other is to employ biologically specific interactions, for example, the biotin/avidin or the biotin/streptavidin interaction. Yu and Christensen in our group exploited a technique to build up a layer-by-layer model based on the alternate deposition of streptavidin and biotinylated goat anti-mouse IgG[26,163]. The 3-mercaptoproponic-acid SAM and the following covalent attachment of streptavidin by means of active ester chemistry was important for the consistent build up of protein layers without any receding up to 10 layers. On the contrary, if a biotin SAM (χ = 0.1) replaced the carboxyl SAM, the thickness of each layer decreased significantly, and the scaffold construction lasted for only 4-5 layers (data not shown). One possible explanation for this is the random orientation and the steric hindrance mentioned in Section 5.3.1. While the biotin SAM anchored streptavidin molecules are packed as a planar monolayer on the surface[47] and, hence, the following LEGO depends on the exact locations of each biotin of the IgG, the covalent binding of streptavidin may results in a branched structure which is easily accessed by the biotinylated IgG .

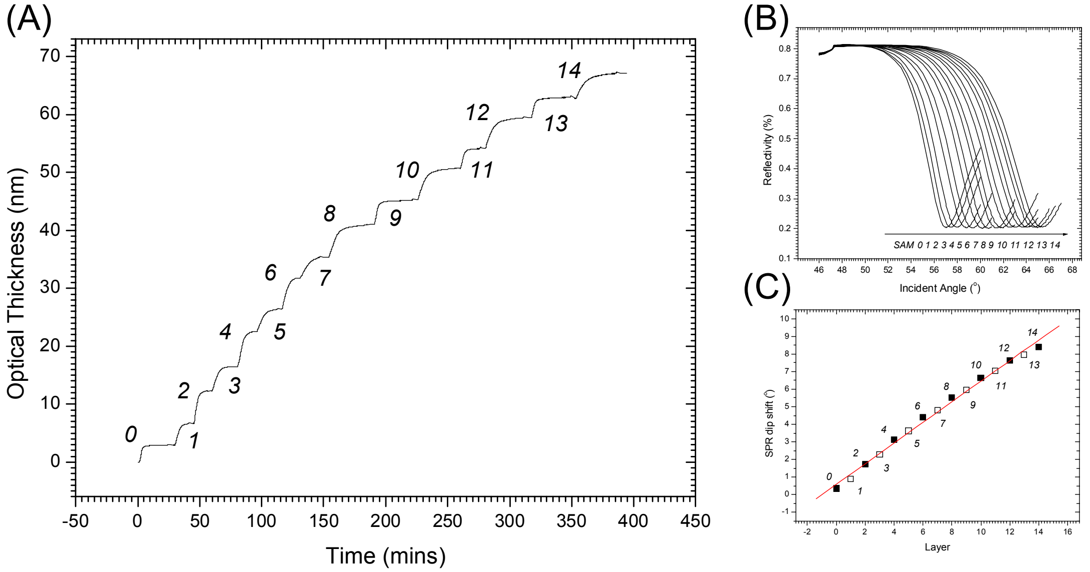

Figure 6.23: A layer-by-layer structure based on avidin/biotinylated anti-avidin IgG interactions. (A) The immobilization kinetics converted to optical thickness based on the refractive index of 1.45 for both proteins. (B) Corresponding SPR angular scans of each layer's binding. (C) The rough linear relation between SPR angular shift and the numbers of layer.

Considering this, one possible path to solve the problem is to utilize biotinylated anti-streptavidin or biotinylated anti-avidin to enhance the probability of the antibody's approach and binding to the antigen. A gold surface coated with biotin SAM (χ = 0.1) was still utilized in this study. A 200 nM avidin solution prepared in PBS buffer was injected into the flow cell and circulated for 15 minutes to activate the foundation of the layer-by-layer LEGO. This reaction yielded a SPR angular shift of 0.35^o, equivalent to a 53% coverage of a densely packed avidin monolayer according to the avidin molecular dimension of $4.0 \times 5.5 \times 6.0$ nm^3 and a molecular weight of 68 kDa[164]. Afterward, the alternate circulations in the loop of an 11.5 μg/mL solution of biotinylated anti-avidin IgG (odd numbers in Figure 6.23) for 15 minutes (30 minutes from layer 9 on) and a 200 nM solution of avidin (even numbers in Figure 6.23) for 10 minutes (30 minutes from layer 10 on) were performed. Both proteins were prepared in PBST buffer, and an angular scan was made at the end of fresh buffer rinse followed every binding. The results (cf. Figure 6.23) showed at least 14 layers can be achieved based on this newly-designed key-to-lock model, although there was a slight tendency decreasing consecutive layers' thickness and a reduction of the association speed. Assuming a refractive index of $n = 1.45$ for both proteins, an optical thickness of more than 20 nm has been achieved after two alternate cycles (four layers). Such a distance is beyond 3~4 Föster radii, sufficient to lower the fluorescence quenching effect.

6.7 LHCII included Proteo-liposome Fusion

As stated in Section 6.1, the thylakoid membrane is the natural environment for antenna complexes. Therefore, the most appropriate way to immobilize LHCII on the surface while maintaining its biological activity should be a functional tethered lipid bilayers *in vitro* mimicing the thylakoid's native composition with an inserted complex. Although many attempts have been tried to characterize LHCII by spectral means, few studies have been reported upon the behavior of the complex in reconstituted lipid bilayers. Here we present some preliminary experiments on LHCII included proteo-liposome fusion on the surface.

Stamouli *et al.*[165] presented a combination of freeze-thaw and dialysis steps for the reconstitution of the Light Harvesting 2 complex (LH2) from a purple bacterium into preformed egg phophatidylcholine (PC) liposomes, without the need for extra chemical agents other than the detergent, and confirmed by AFM the protein incorporation into a flat bilayer formed on a mica surface. In the process of the lipid supported or tethered bilayer construction, a crucial step is the achievement of spontaneous vesicle (or proteo-liposome) fusion on the template. To overcome the constraints imposed by the uncontrolled kinetics of spontaneous vesicle fusion, Berquand *et al.*[166] recently proposed a two-step strategy for the assembly of a supported bilayer on a streptavidin sublayer. We adopted this protocol for the incorporation of LHCII into the liposome and the following vesicle fusion on streptavidin surface (cf. Figure 6.24).

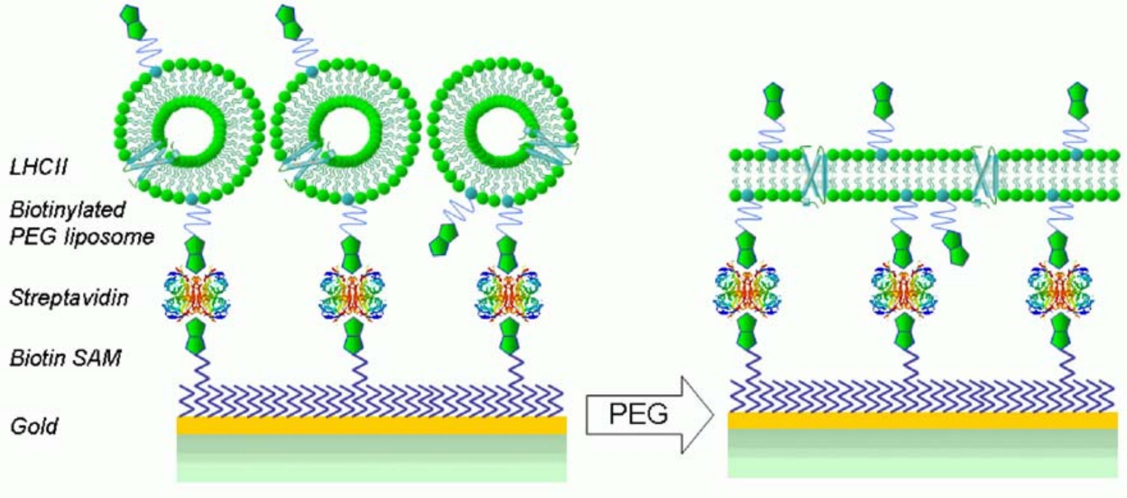

Figure 6.24: Schematic view of LHCII included biotinylated proteo-liposome fusion on streptavidin surface induced by a PEG solution.

Egg PC (1.88 mg) and biotin-PEG-DSPE (0.12 mg) were dissolved in 1 ml chloroform. The solvent was evaporated under a flow of dry nitrogen gas for several hours. After adding 1 ml NaP buffer (20 mM sodium phosphate, pH 7.4), the hydrated films were sonicated in a bath sonicator (Merck Eurolab GmbH) for at least 15 minutes, then frozen in liquid nitrogen and slowly thawed at room temperature. The solution was sonicated and freeze-thawed at least four times until it was almost transparent. Next, the solution was centrifuged (4000×g for 5 minutes) and the supernatant was removed, resulting in a lipid concentration of ca. 2 mg/ml. 1 ml 810 nM Tri-Hu10 solution after ultrafiltration prepared in immobilization buffer (20 mM sodium phosphate, pH 7.4, 0.1% DM) was added to the liposome solution. The sample was mixed with Bio Beads (100 mg/ml) and gently shaken, then incubated overnight at 4°C. The final supernatant proteo-liposome solution for immobilization had a concentration of about 405 nM Tri-Hu10, 0.94 mg/ml Egg PC, 0.06 mg/ml biotin-PEG-DSPE.

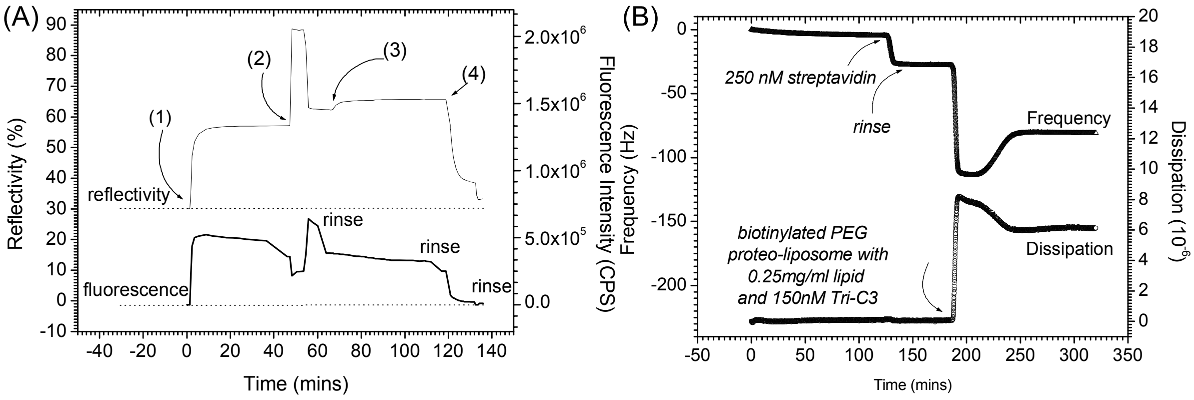

Figure 6.25: The immobilization and fusion of LHCII included biotinylated proteo-liposome on streptavidin layer. (A) Kinetic working curve characterized by SPFS. (B) Kinetic working curve recorded by QCM.

A streptavidin layer on a biotin SAM (χ = 0.1) coated gold surface was used for the immobilization of LHCII doped biotinylated proteo-liposome. As depicted in Figure 6.25 (A), 500 μl of the above liposome solution was injected into the flow cell (1), and incubated for 40 minutes, producing an SPR angular shift of 1.1°. The loop was then filled with 25% PEG solution prepared in MillQ water (2) in order to trigger the fast formation of a bilayer. After 5 minutes, the flow cell was rinsed with fresh NaP buffer (20 mM sodium phosphate, pH7.4), then with a 250 nM streptavidin solution prepared in NaP buffer (3). The incubation lasted for 40 minutes, resulting in a SPR angular shift of 0.25°. This is equivalent to a 31% coverage of a densely packed streptavidin monolayer, implying the formation of a layer-by-layer structure fabricated via the free biotin moieties protruding from the surface of the liposomes or in the outer part of the surface anchored lipid bilayer membrane. Next, 5 μl 10% (w/v) DM was added into the sample tube and quickly diluted by the solution in the loop system (4) to a final concentration of about 0.1%. The introducing of detergent destroyed the lipid bilayer structure of the liposome or the membrane, which was seen as a dramatic reflectivity change. After a final rinse with fresh buffer, the baseline did not return to its original value, but represents the contribution of the streptavidin anchored biotin-PEG-DSPE on the surface. The signal recorded by the fluorescence channel followed almost completely synchronized with the reflectivity signal except for a tiny difference (cf. (2) in Figure 6.25 (A)) that might originate from the detuning effect.

The results clearly indicated the accumulation of proteo-liposomes of the surface. The accumulation was affinity specific because in a control experiment with proteo-liposome lacking biotin-PEG-DSPE on the same surface, only a minor background jump which could be totally reversed after rinse was found (data not shown). However, the formation of a surface tethered membrane could not be exactly resolved by SPFS.

In a recent investigation by Keller and Kasemo[167], the QCM (quartz crystal microbalance) technique was utilized to measure the kinetics of the adsorption of small unilamellar vesicles onto SiO_2, oxidized gold, and a SAM of methyl-terminated thiols. A two-phase behavior on SiO_2 suggested that the formation of a lipid bilayer was preceded by the adsorption of intact vesicles. While the characterization of the membrane construction by electrochemical tools generally requires a complete and compact lipid bilayer, QCM, on the other hand, can record the partial formation of the lipid bilayer structure. In another experiment with Tri-C3 loaded biotinylated proteo-liposomes on a streptavidin layer, Q-sense D300 instrument (Q-sense AB, Sweden) was employed to measure the kinetic process of binding and fusion. After the surface activation with 250 nM streptavidin on a biotin SAM ($\chi = 0.1$) surface, biotinylated proteo-liposome solution with a lipid concentration of 0.25 mg/ml and a protein concentration of 150 nM was introduced into the measurement chamber (cf. Figure 6.25(B)). Even without PEG triggering, a strong decrease of the resonance frequency (increase in adsorbed mass) and the concomitant increase in the dissipation was observed followed by a reduced mass coverage and a return of the dissipation, which was the evidence for a partially formed protein loaded lipid bilayer. An intact LHCII doped membrane may be obtained by altering the components of the liposomes according to the natural thylakoids membrane (cf. Section 6.5.5) or by optimizing the liposome concentration.

6.8 Surface Density Optimization

The data on the His-tag coupling method presented in Table 6.3 were obtained with structures that had been functionally optimized for maximum binding of His-tagged LHCII. The surface density optimization process is presented in this section.

6.8.1 Optimization Principle

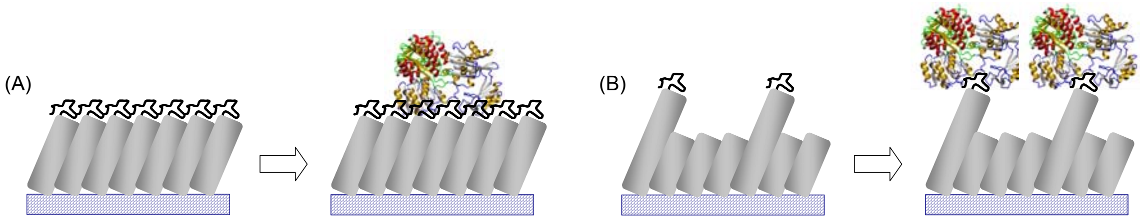

Figure 6.26: Schematic representation of the strategy for surface density optimization. (A) The dense packing of ligate recognition motifs resulting in a mutual blocking of the ligate binding. (B) The lateral dilution of the ligate recognition motifs by some short spacers allows binding of ligates.

The reason for the need of a surface density optimization is given schematically in Figure 6.26. If each ligand coupled on the surface carries a ligate recognition motif, the binding of the ligate to an individual ligand is not possible any more because in a densely packed monolayer or semi-monolayer, all the motifs form a tight "carpet" and hence mutually block each other, resulting in a comparatively low immobilization of ligates. This can be greatly improved if the individual ligate recognition motifs are laterally diluted from their neighbors by inserting some short spacers. The ratio between ligands and spacers must be carefully tuned in order to get a maximum ligate coupling density. This theory has been successfully proved by streptavidin immobilization on the top of biotin SAM[47] and NADP+ reductase immobilization onto dithioctic acid SAM supported ANTA surface[147].

As the home-made His-tag chelating chip D does not show a strong surface coupling of His-tagged LHCII compared with the other chips, and the surface activation process of the chelating chip A involved the troublesome NHS ester chemistry whose efficiency can not be monitored by reflectivity alteration, we will discuss here only the surface density optimization of the chelating chip B and C, respectively.

6.8.2 Optimization of the His-tag Chelating Chip B

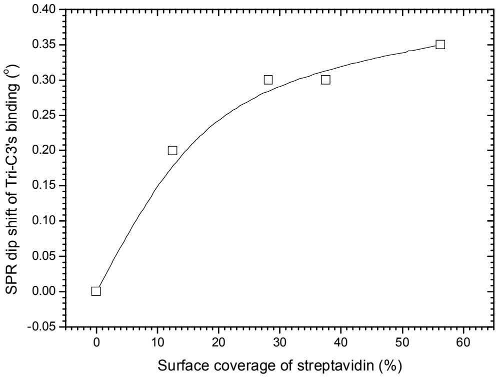

Figure 6.27: SPR angular shift of Tri-C3 as a function of streptavidin surface density.

Because the Biotin-X-NTA is much smaller than the streptavidin molecule, lateral dilution of NTA groups for the His-tag chelating chip B can be reached by controlling the streptavidin binding density. As for of the streptavidin immobilization, there are two ways to get different surface coverage: one is to vary the ratio of biotin thiol in the mixed solution based on Spinke's study[49], the other is to realize this by adjusting the streptavidin reaction time. Since there is no difference between the final effects, the latter was used in this study because it could be easily controlled by inspecting the reflectivity changes. Five gold chips covered with biotin SAM (χ = 0.1) were used for the optimization. A 100 nM streptavidin solution prepared in PBS was injected to four chips and incubated without circulation in order to ensure mass-transport dominated kinetics as reflected as a linear increase of the signal in the reflectivity channel. The other chip was used as a negative control. By stopping the binding at different times, 5 chips with different streptavidin surface coverage from 0% (negative one) to 56.25% (saturated SAM) of a densely packed monolayer were obtained. All of them were surface activated with Biotin-X-NTA and $NiCl_2$ following the protocol described in Section 6.4.3. 500 nM Tri-C3 solutions prepared in PBS+DM buffer (PBS buffer with 0.1% (w/v) DM) were introduced in the flow cell subsequently and incubated for one hour, followed by a fresh buffer rinse. The SPR minimum angle was checked by angular scans. The dip shift versus the corresponding streptavidin coverage is plotted in Figure 6.27. It is obvious that the degree of His-tagged LHCII's coupling is proportional to the level of streptavidin's coverage. No indication of an influence similar to the biotin SAM optimization was seen[49]. This is reasonable because the size of the LHCII (even trimers) does not differ too much from the dimensions of one streptavidin molecule, and maximum streptavidin coverage is only 56.25%, far from a densely packed monolayer which would result in a mutual blocking effect.

6.8.3 Optimization of the His-tag Chelating Chip C

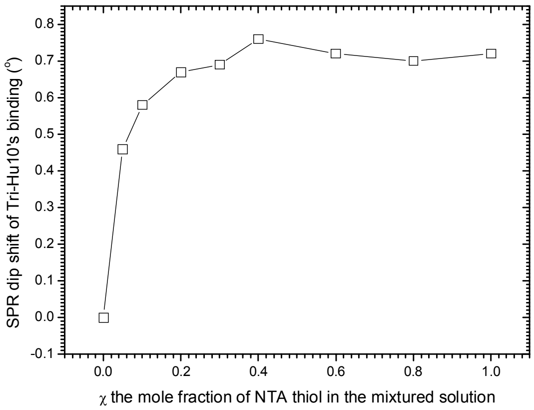

Figure 6.28: SPR angular shift of Tri-Hu10 as a function of NTA thiol content χ.

For the His-tag chelating chip C, the surface density optimization process is similar to the procedure applied in the biotin SAM case. Nine chips with different NTA-terminated thiols in the mixed solution were self assembled for 24 hours. After a surface activation with the $NiCl_2$ solution, the flow cell was filled with a 1 µM Tri-Hu10 solution prepared in NaP+LM buffer (20 mM sodium phosphate, pH 7.4, 0.1% (v/w) DM) for 60 minutes. The SPR angular scan was taken after rinse. The dip shifts versus the mole fraction of the NTA thiol in the mixed SAM solution is plotted in Figure 6.28. About 40 mol% of the NTA thiol is needed to obtain a maximum His-tagged LHCII binding. If more NTA thiols were incorporated into the mixed SAM, only a tiny loss of binding capacity was found different to the case of biotin SAMs optimization[49]. Possible reasons for this phenomenon are: firstly, unlike for the biotin/streptavidin interaction which involves the insertion of biotin-group into the inner domain of the streptavidin structure, the 6×His-tag is at the end of the polypeptide beyond the hydrophobic domain of the LHCII, easily accessible for Ni-NTA; secondly, this special tag is composed of six histidines, with only two of them being chelated by nickel ions. The rest can be coupled by neighboring Ni-NTA if the adjoining functional thiols are close enough, which is expressed as the avidity of 6×His-tagged LHCII on the Ni-NTA surface. Both scenarios would explain the greatly diminished steric hindrance effect.

6.8.4 Distance between Neighboring LHCIIs

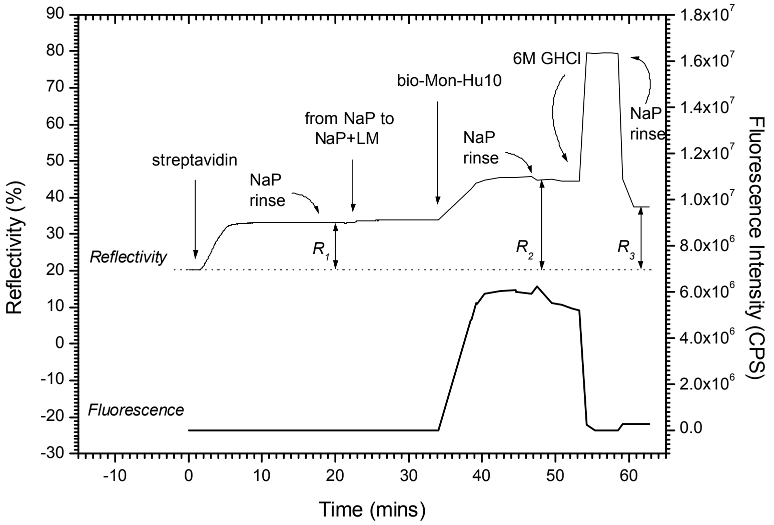

Figure 6.29: The experiment to estimate the molecular weight of detergent bound complex on the surface.

Taking the coupling of Tri-Hu10 on a NTA SAM ($\chi = 0.4$) surface as the example, we can clearly reestablish the profile on the surface if the molecular weight of LHCII is known exactly. Crystal structure of LHCII confirmed by electrophoresis indicates a molecular weight of 35 kDa, including 25 kDa of apoprotein part and 10 kDa of pigments part. If the complex is solubilized in detergent containing buffer and coupled to the surface, the situation is totally different owning to the tightly bound amphiphilic detergent molecules assembled around the complex. Such detergent components also influence the mass change of the surface, represented by the reflectivity variation. A small experiment (cf. Figure 6.29) was designed to understand the contribution of bound detergents. 500 nM biotinylated monomeric Hu10 in NaP+DM buffer (20 mM sodium phosphate, pH 7.4, 0.1% (v/w) DM) was injected to a streptavidin surface assembled on a biotin SAM ($\chi = 0.1$), reacting for 10 minutes to reach the equilibrium, followed by a NaP buffer rinse. A SPR angular scan monitored the surface coupling (R_2-R_1 = 0.5°).

Then 6 M guanidine hydrochloride (GHCl) was introduced into the flow cell and circulated for 5 minutes in order to eliminate both detergents and pigments thoroughly. A SPR scan followed another NaP buffer rinse in order to get the remaining, *i.e.* surviving apoproteins firmly attached by the biotin/streptavidin on the surface (R_3-R_1 = 0.19^o). The difference between these two measurements should be equivalent to the amount of the apoprotein occupied in the whole detergent bound complex. Knowing the molecular weight of the apoprotein (25 kDa), it is then easy to get the detergent bound complex as ca. 66 kDa.

Therefore, we can calculate the protein mass density with 100% coverage of a LHCII monolayer on the surface, knowing the dimensions of LHCII monomer to be 4.8 × 4.8 × 3.2 nm^3 and the complex is located on the 4.8 × 3.2 face[47].

$$\frac{1mm^2}{4.8nm \times 3.2nm \times 6.02 \times 10^{23} mol^{-1}} \times 66kg/mol = 7.1ng/mm^2 \qquad \text{--- 6.1}$$

This equals to ca. 1.35^o SPR minimum angle shift in our home-made SPFS setup (cf. Section 2.1.3). Tri-Hu10's coupling on a NTA SAM (χ = 0.4) surface produced an angular shift of 0.76^o, corresponding to 56% surface coverage, equivalent to a center-to-center distance between adjacent complexes of 5~6 nm. Such a distance is in the efficient FRET range, allowing for an efficient energy transfer between chlorophyll *a* molecules in neighboring LHCII complexes. As the distance increases, *e.g.* LHCII coupled on His-tag chelating chip B, the FRET efficiency will drop significantly.

6.9 Energy Transfer between Neighboring LHCIIs

As was mentioned in Section 6.1, there are two kinds of energy transfer for LHCII, the "intra-complex energy transfer" and "inter-complex energy transfer" respectively. While many studies have addressed the intra-complex energy transfer[108], including the Chl *a* to Chl *a* excitation energy transfer, and the Chl *b* to Chl *a* excitation energy transfer that can be judged by the Chl *b*-sensitized Chl *a* fluorescence, there are few investigations that focus on the inter-complex energy transfer, especially in constructing biomimetic models to simulate such energy migration process. It was demonstrated by Kleima *et al.* that all

Chl *b* to Chl *a* transfer processes can be assigned to events within a monomeric subunit[168]. Thus, subsequent excited-state equilibration between monomers within a trimer is obtained via Chl *a* to Chl *a* transfer only. Because most of "normal" spectroscopic tools, the main facilities for the investigation of LHCII, are usually dealing with steady-state conditions, it is almost impossible to test the inter-complex energy transfer except those inside an individual trimer.

Wolf-Klein *et al.*[169] constructed the first biomimetic model (LHCIIb-BCI) of a plant photosystem that contains a self-assembling recombinant light-harvesting complex of the photosynthetic apparatus in higher plants. This model mimiced successfully the efficient transfer of absorbed light energy to an acceptor but differed from a photosystem in that the light energy was not converted into potential energy by charge separation. Although the energy transfer efficiency was proved to be very high (70±4% at 297 K and 85±4% at 77 K), this transfer was still confined to be of the intra-molecular character.

6.9.1 Intra-Complex Energy Transfer Observed by SPFS

Having the ability of inspecting biomolecular interactions on the surface in real time, SPFS can be further developed to investigate the energy communication among surface-anchored LHCIIs in order to successfully mimic the biochemical process, an artificial energy trap has to be chosen as a substitute to the missing reaction center.

In a preliminary experiment performed in order to monitor the energy transfer in the normal direction of the metal-dielectric surface, an Alexa Fluor 700 streptavidin conjugate (AF-700 streptavidin) was utilized as the final energy acceptor. His-tag chelating chip C was selected as the supramolecular structure to immobilize biotinylated Tri-Hu10, upon which AF-700 streptavidin could be further coupled (cf. Figure 6.30 (A)). The immobilization kinetics was recorded via the reflectivity channel by excitation with a HeNe laser, while the surface plasmon excited fluorescence spectra were detected with a Nd:YAG DPSS blue laser. As shown in Figure 6.30 (B), after incubation of 1 μM biotinylated Tri-Hu10 in DM containing buffer for one hour, 20 μl of a 1 mg/ml AF-700 streptavidin stock solution was injected in the incubation tube and quickly diluted by the loop system to a final concentration of ca. 40 μg/ml. The reaction was running for 10 minutes before a fresh buffer rinse. Equilibrium procedures were performed on the OEG-terminated spacer thiol assembled surface in order to to prove the specificity of the binding. The fluorescence emission spectra after one hour of LHCII's incubation (1), immediately after AF-700 streptavidin's injection (2) and after 10 minutes of the conjugate's injection (3) are plotted in Figure 6.26 (C). The sudden decrease of the donor (Chl *a*) emission due to the introduction of AF-700 streptavidin, and the gradual increase of the acceptor emission correlated with the association of the conjugate are clearly seen. However, the possibility of some inter-complex energy transfer still needs to be evaluated by other strategies.

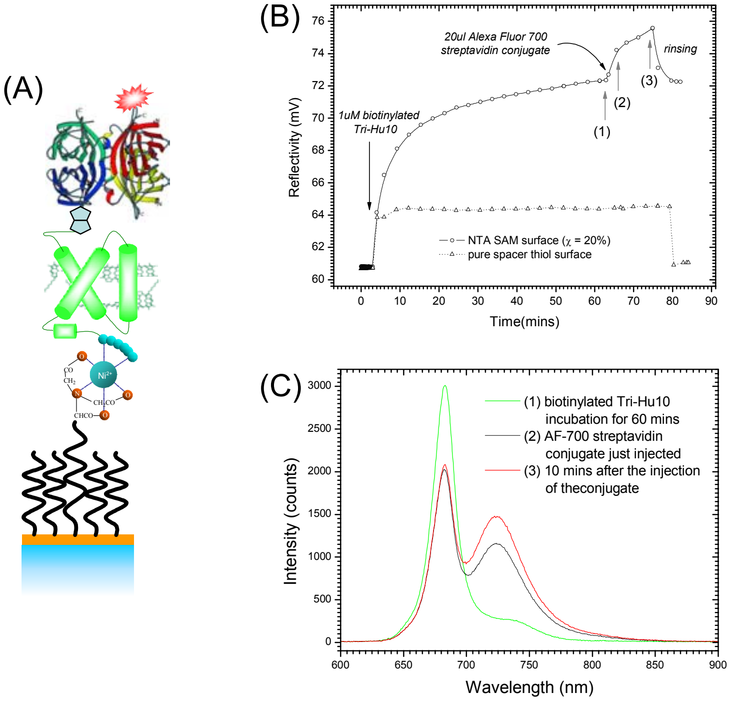

Figure 6.30: (A) His-tag chelating chip C was used to construct the supramolecular structure for energy transfer study; (B) The binding kinetics of biotinylated Tri-Hu10, followed by Alexa Fluor 700 streptavidin conjugate on NTA SAM surface and OEG spacer thiol surface; (C) Fluorescence emission spectrum recorded during the binding.

6.9.2 Inter-Complex Energy Transfer Observed by SPFS

6.9.2.1 Materials and Methods

In the next study, another DY-730 dye commercially available for thiol-reactive labeling from Dyomics was chosen as the substitute for Alexa Fluor 700. The emission maximum of DY-730 (cf. Figure 6.31 (A)) is $\lambda =$ 758 nm, sufficiently separate from the Chl *b*'s emission peak, allowing for a better observation of the emission spectrum at low resolution conditions. DY-730 maleimide (cf. Figure 6.31 (B)) was attached to a single cysteine residue in position 79 near the N terminus of the *lchb1* mutant Hu10. After purification by preparative electrophoresis, Hu10-DY-730 was reconstituted with pigments following the protocol presented in Section 3.3. Only trimers were studied in these experiments.

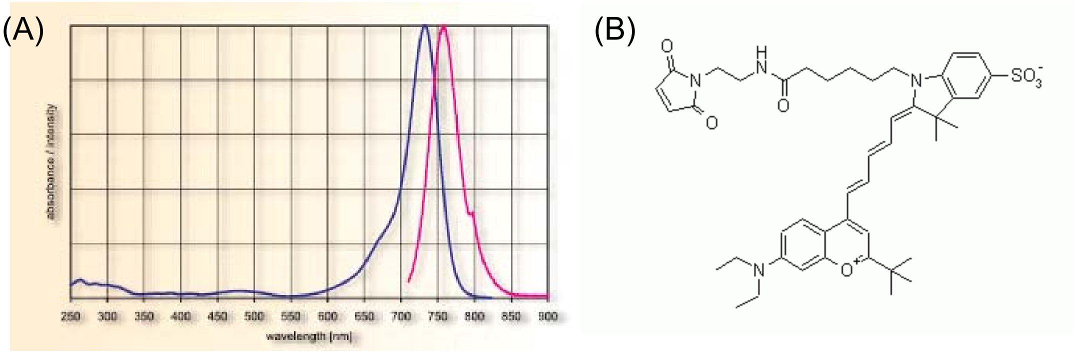

Figure 6.31: (A) Fluorescence excitation and emission spectra of DY-730 in ethanol. (B) The chemical structure of DY-730 maleimide.

A His-tag chelating chip C was selected for the energy transfer experiments in this section because of its strong His-tagged LHCII binding capacity mentioned in Section 6.8. The detailed binding kinetics was presented in Figure 6.17 (A), with the excitation by a blue laser which was also used to monitor the biological spectral emission activity of surface anchored LHCII. Before the samples injection, a background spectrum was recorded ((1) in Figure 6.32 (A)). During the first cycle, a mixed solution of 30% Tri-Hu10-DY-730 and 70% Tri-Hu10 (mimicing the natural situation in the thylakoid membrane with a large amount of antenna complexes and a small amount of reaction centers) with a net LHCII concentration of 1 μM was introduced into the flow cell and a spectrum collected after a fresh buffer rinse following 30 minutes of incubation ((5) in Figure 6.32 (A)). The fluorescence emission spectra of 1 μM pure Tri-Hu10-DY-730 ((3) in Figure 6.32 (A)) and 1 μM pure Tri-Hu10 ((2) in Figure 6.32 (A)) were recorded in the next two cycles. Finally, after three regenerations, the loop was filled with the mixture again and the fluorescence emission spectrum was recorded.

6.9.2.2 Results and Qualitative Analysis

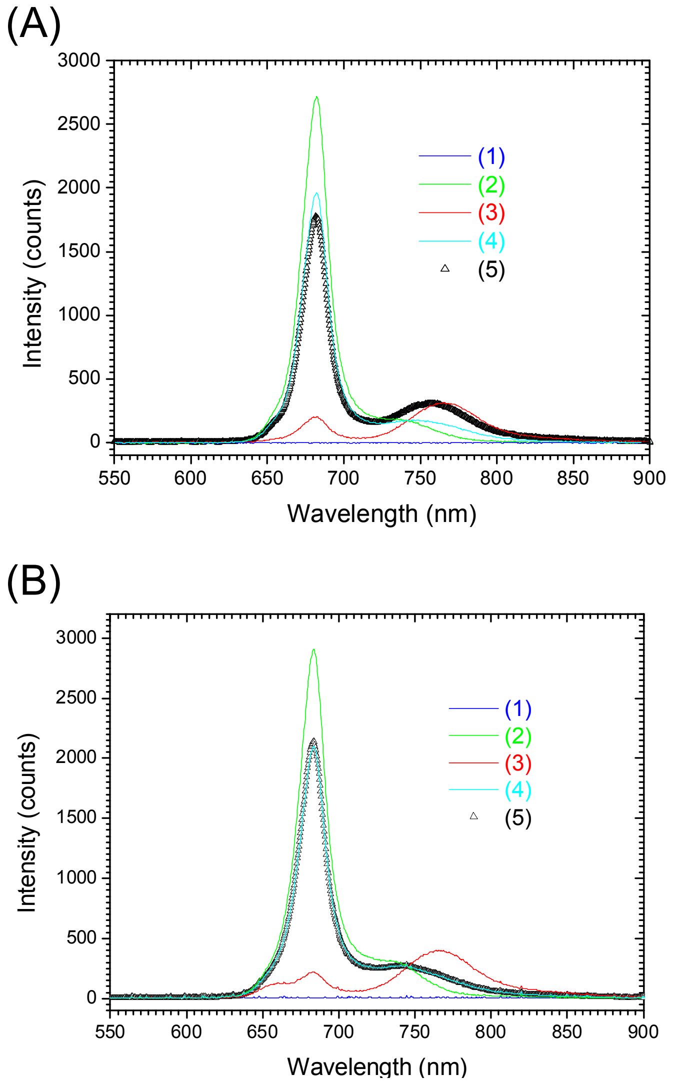

Figure 6.32: The fluorescence spectra captured on the surface (A) and in solution (B) in the LHCII coupling experiment showed in Figure 6.17 (A). Detailed descriptions about (1), (2), (3), (4) and (5) are in the text.

The emission spectrum of Tri-Hu10 ((2) in Figure 6.32 (A)) exhibits a maximum at λ = 682.3 nm, near the emission maximum of Chl *a*, and a latent shoulder at ca. λ = 730 nm, which has long been thought to be a contribution from chlorophyll aggregation[123]. On the other hand, the emission spectrum of Tri-Hu10-DY-730 ((3) in Figure 6.32 (A)) exhibits a small peak at λ = 682.6 nm, while a strong peak at λ = 764.5 nm, near the emission maximum of DY-730, suggests an efficient intra-energy transfer from the chlorophylls to the acceptor dyes.

Since DY-730 labeling was made on the single cysteine residue in the LHCP polypeptide via maleimide, the degree of labeling should not be larger than 1. Furthermore, the molecular weight of DY-730 maleimide is only 783 Da. Such a small part should not have a strong influence on the binding properties of LHCII, as it was shown in Figure 6.17 (A) by the same SPR angular shift in each cycle. Thus, although the composition of two species might not be the same as in the preparation solution, the surface formation of a mixed SAM structure, should be normally valid and acceptable.

Therefore, if there is only intra molecular energy transfer existing, the fluorescence emission spectrum of the mixture should be the sum of the components' individual spectra with relative contributions corresponding to their molar ratios, which is called "theoretical spectrum" here. Take Figure 6.32 (A) as an example, the theoretical spectrum of the mixture on the surface is the overlap of 30% of (3) and 70% of (2), expressed as (4). It is apparent that there is huge difference between (4) (theoretical spectrum) and (5) (experimental spectrum). The decrease of the donor peak and the increase of the acceptor peak in the experimental spectrum compared with the theoretical spectrum imply the occurrence of not only an intra-complex energy transfer, but also an inter-complex energy transfer between neighboring LHCIIs.

On the contrary, in aqueous solutions, the experimental spectrum should be exactly coincide with the theoretical spectrum, because individual complexes are separated from each other beyond the Föster distance of such homogeneous conditions, and no inter-complex energy transfer will occur. Below a certain critical angle given by Snellius law, there is no surface-plasmon field enhancement happening, only a small part of the light is transmitted into the water medium, exciting the fluorophores in the bulk solution and at the metal-aqueous interface simultaneously. Since the complexes coupled on the surface account for only a small fraction of the total protein, the fluorescence spectrum captured should reflect the situation in solution. Without exception, the spectra in solution in this section refer to the fluorescence emission spectra monitored by the optical spectrometer if the incident angle is at $\theta = 45^{\circ}$. Like Figure 6.32 (A), Figure 6.32 (B) illustrates the spectra in solution including the background spectrum (1), the Tri-Hu10 spectrum (2), the Tri-Hu10-DY-730 spectrum (3), the theoretical spectrum of the mixture (4) and the experimental spectrum (5). Different from the situation on the surface, the theoretical data almost perfectly describe the experimental data.

6.9.2.3 Quantitative Analysis via PFM

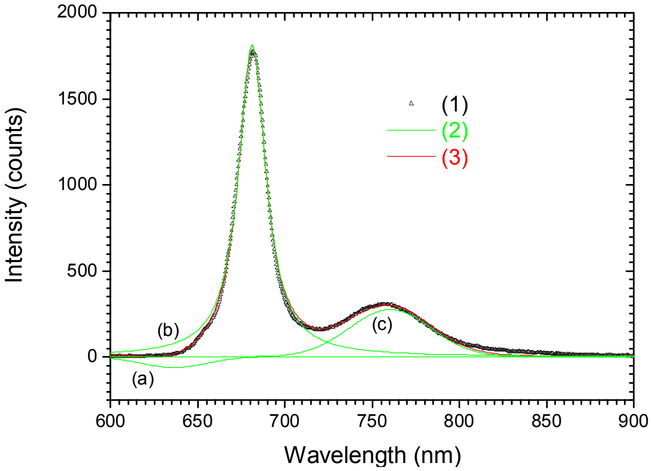

Figure 6.33: Using Peak Fitting Module to analyze a fluorescence emission spectrum. (1) Original data; (2) Theoretical curves for individual peaks; (3) Theoretical curve for the entire dataset.

Even though we have successfully prove the inter-complex energy transfer between neighboring LHCIIs, quantitatively resolving the efficiency of such transfer requires the deconvolution of the final spectrum into its original donor part and acceptor part. Here we propose a simple strategy to judge the energy transfer based on Origin 7.0's Peak Fitting Module (PFM) semi-quantitatively. This tool offers a wizard interface to step the user through the steps of advanced peak analysis suitable for chromatography, spectroscopy, engineering, pharmacology, and other fields of investigation. As shown in Figure 6.33, taking the spectrum (5) in Figure 6.32 (A) as an example, the analysis via PFM results in a theoretical curve for the entire dataset ((3) in Figure 6.33) and three theoretical curves for the resolved individual peaks ((2) in Figure 6.33). At the same time, corresponding information for each peak, including fitting peak area, FWHM (full width at a half maximum), the spectral location of each peak, maximum peak intensity and so on, are also obtained. Normally, a Lorentzian function was used to fit the peak corresponding to the Chl *a* emission maximum and a Gaussian function was applicable for the other peaks. In Figure 6.33, the sum of peak (a) and (b) was considered to be the donor area, whereas peak (c) was thought to be the acceptor area. The ratio expressed as the donor area dived by the acceptor area was identified as an important factor to scale the energy transfer efficiency. For every experimental spectrum, one can calculate such a factor according to the algorithm stated above, while a theoretical factor can be obtained by resolving the theoretical spectrum similarly. The difference between these two factors is proportional to the inter-complex energy transfer efficiency depending on our hypothesis. The larger the difference, the more energy has been captured by the acceptor dye.

6.9.2.4 Influence of the Mixture Ratio on the Energy Transfer Efficiency

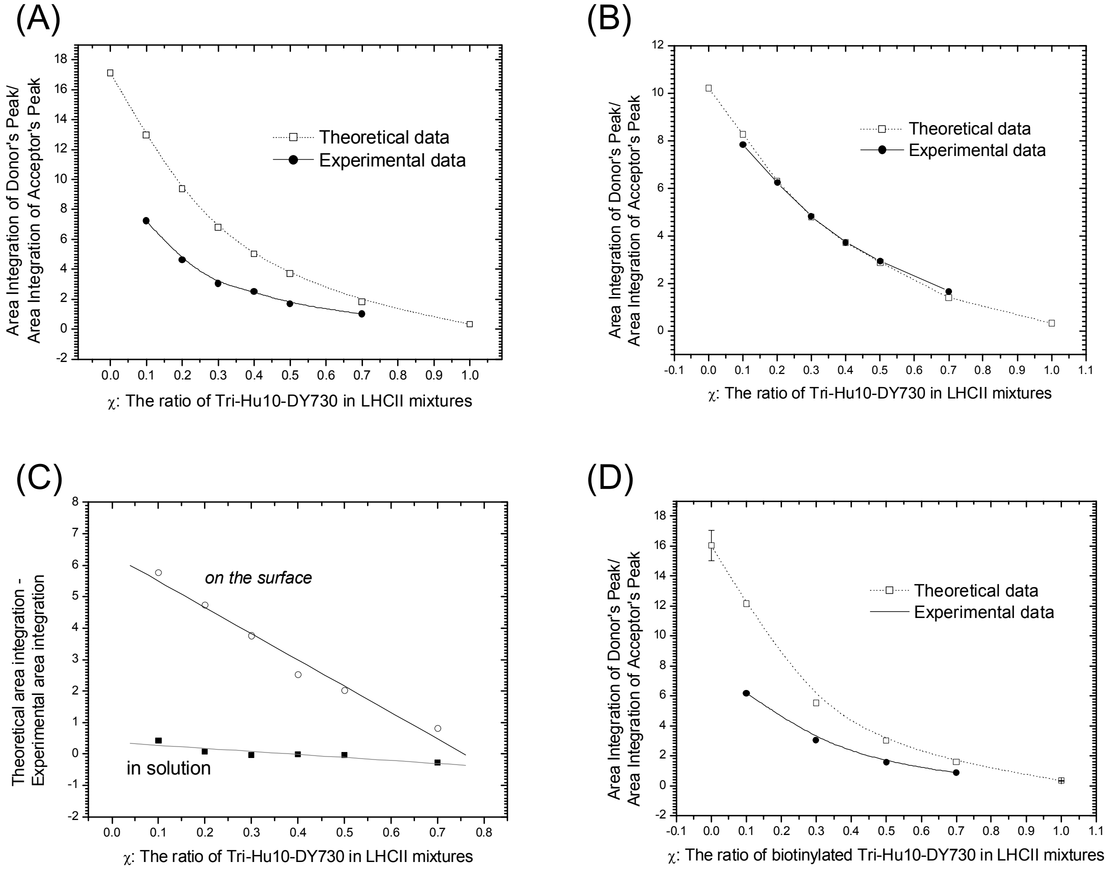

Figure 6.34: The inter-complex energy transfer shown as the difference between the experiment data and the theoretical data. (A) The surface plasmon field-enhanced fluorescence emission spectra based calculation results about the mixture of Tri-Hu10 and Tri-Hu10-DY-730. (B) The aqueous fluorescence emission spectra based calculation results about same mixture as (A). (C) The difference between the theoretical data and the experimental data as the function of χ, the molar ratio of Tri-Hu10-DY-730, both on the surface and in solution. (D) Repeated (A) with different batches of samples on chips prepared at different time.

A series of experiments with different molar ratios of Tri-Hu10-DY-730 in the mixed solution were performed on the His-tag chelating chip C. All the spectra were analyzed via the method mentioned above. The factors calculated versus the molar ratio of Tri-Hu10-DY-730 are plotted in Figure 6.34. Both the spectra recorded from the complex on the surface and in solution are presented in (A) and (B) in Figure 6.34 respectively. For each graph, both the experimental data and the theoretical data are depicted. Two interesting features are worthwhile to point out.

It is obvious that for the situation on the surface, there is significant difference between the theoretical data and the experimental data (cf. Figure 6.34 (A)), which is attributed to the inter-complex energy transfer between surface coupled neighboring LHCIIs. Such a difference is inversely proportional to χ, the molar ratio of Tri-Hu10-DY-730 in the mixed solution, indicating that for a fixed surface mixture of LHCIIs, the smaller the portion of the energy traps is, the higher is the energy transfer efficiency. In fact, this finding is easily understood. For the energy migration along surface coupled LHCIIs, the acceptor dyes are the final target of the light energy harvested by those complexes. If there is only one acceptor dye existing, all the light will be transferred to this final reservoir, expressed as the highest energy transfer efficiency in an ideal and perfect situation. On the other hand, as mentioned above, in solution the experimental data always agree with the theoretical data (cf. Figure 6.34 (B)), irrespective of the molar ratio of the dye-coupled LHCIIs. A more straightforward way to clarity this difference is shown in Figure 6.34 (C), where the difference versus χ, both for the results on the surface and in solution, is plotted directly, indicating a horizontal line at zero level for the latter while a straight line with a slope suggesting the inter-complex energy transfer is found for the former.

This inter-complexenergy transfer phenomenon was not by accident, but could be duplicated on the same chip after several regenerations. As shown in Figure 6.17 (B), not only was the area integrated of the spectrum in the fourth cycle still 80% of the original value, but the variation of the factor calculated according from their fluorescence spectra was less than 3%. In addition, this energy transfer could be repeated with different batches of samples on chips prepared at different time, *e.g.* the surface immobilization of biotinylated Tri-Hu10 and biotinylated Tri-Hu10-DY-730 mixture on a His-tag chelating chip C, shown in Figure 6.34 (D). Moreover, the validity of this simple strategy has been proves by much stricter deconvolution methods only in view of donor quenching or taking the fluorescence quantum yield of the protein-bound DY-730, which is 12%, into consideration. The strategy for this deconvolution method was proposed by Wolf-Klein[170] and the results about our His-tag chelating chip C system are plotted in Figure 6.35. Like the simple PFM strategy, the deconvolution method exhibits the existence of the inter-complex energy transfer, and similarly, the energy transfer efficiency is higher for the low acceptor dye concentration.

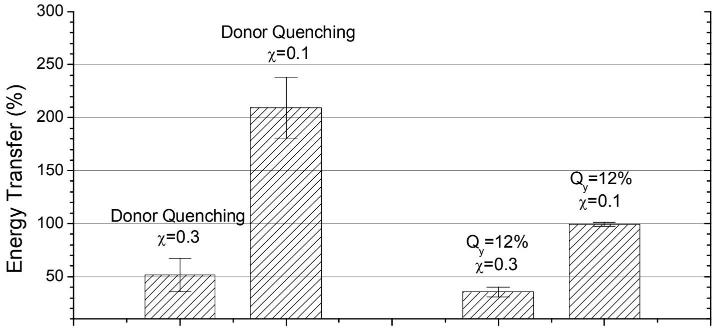

Figure 6.35: Schematics about the inter-complex energy transfer resolved by the deconvolution method.

6.9.2.5 Influence of the Surface LHCII Density on the Energy Transfer Efficiency

Inter-complex energy transfer processes are strongly involved in the optial coupling of antenna complexes. As mentioned in Section 2.2.2, the efficiency of FRET falls off with the sixth power of the separation distance between the donor and the acceptor (cf. Equation (2.21)). If the donor and the acceptor are separated by distances of $>2R_0$, no FRET occurs. Thus, if the surface immobilization density of LHCIIs changes, the distance between adjacent complexes will alter correspondingly, further influencing the communications between neighboring LHCIIs.

There are three ways to modify the degree of LHCII surface coupling. The first method controls the reaction time for the incubation of LHCII solution. As shown in Figure 6.36 (A), for the surface chelation of a 1 μM Tri-Hu10 mixture (χ = 40%), the fluorescence emission spectra on the surface were recorded 3 minutes (red), 6 minutes (green) and 30 minutes (blue) after injection, respectively. The longer the reaction time, the smaller the inter-energy transfer factor (indicated in Figure 6.36 (A)) This implies that more and more light has been delivered to the energy trap as the complexes get closer to each other. These changes can also be directly seen in Figure 6.36 (B) where the normalized spectra are overlaid. In another experiment with a surface chelated 1 μM biotinylated Tri-Hu10 mixture (χ = 50%), similar conclusions were drawn (cf. Figure 6.36 (C)). Besides, control experiments performed by surface coupling of pure biotinylated Tri-Hu10-DY 730 (cf. Figure 6.36 (D)), by surface coupling of pure biotinylated Tri-Hu10 (cf. Figure 6.36 (E)), as well as the spectra of the mixture collected in solution at 45^{o} (cf. Figure 6.36 (F)) all gave the opposite effect – the spectra shapes were independent of the reaction time. These results further solidify the above conclusion.

The second method is to control the surface density of the complexes by changing the ratio of the two thiol components for the SAM formation. As shown in Figure 6.28, the SPR angular scan of Tri-Hu10's binding on the NTA SAM (χ = 0.05) surface was only 60% of that on the optimal surface (χ = 0.4), therefore the energy transfer efficiency of the former should be smaller than the latter. The results about the surface chelation of 1μM Tri-Hu10 mixture with 70% of dye coupled species confirmed this prediction (cf. Figure 6.36 (G)).

And finally, the third way adopts a different supramolecular structure for surface functionalization, for example, using the His-tag chelating chip B, which has been shown to have a lower LHCII holding capacity than the His-tag chelating chip C (cf. Section 6.8). The final spectra after surface chelation of 1μM Tri-Hu10 mixture with 30% of dye coupled species on both chips are plotted in Figure 6.36 (H). According to our expectation, the His-tag chelating chip C has a larger inter-complex energy transfer efficiency than the chelating chip B.

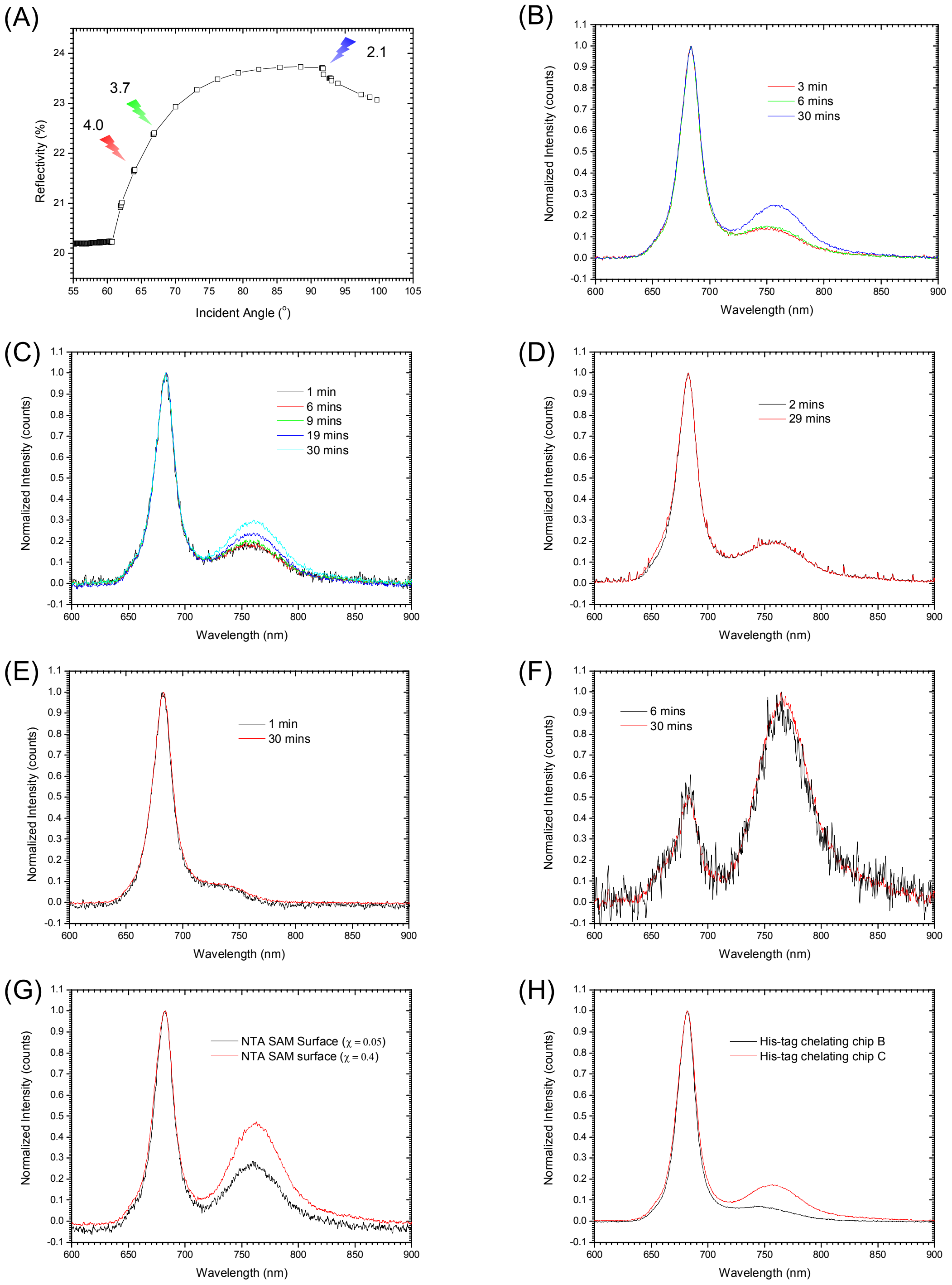

Figure 6.36: The relation between the surface coupling density of LHCIIs and the inter-energy transfer efficiency. (A) Kinetic reflectivity working curve of Tri-Hu10 mixture binding on His-tag chelating chip C. (B) Normalized comparison of fluorescence emission spectra at different reaction time for (A). (C) (D) (E) (F) Repeat experiment (A) and compare the results about pure species binding on the surface and the same mixture binding in solution. (G) Normalized comparison between fluorescence emission spectra about the same mixture coupling on different NTA SAM chips. (H) Normalized comparison between fluorescence emission spectra about the same mixture coupling on His-tag chelating chip B and His-tag chelating chip C. Detailed descriptions are in the text.

6.10 Conclusion

The light-harvesting chlorophyll *a*/*b* protein complex associated with PSII (LHCII), or the peripheral antenna complex, is the most abundant chlorophyll containing complex in higher plants. Its intrinsic fluorescence feature makes the complex an ideal candidate for surface plasmon field-enhanced fluorescence spectroscopy investigations.

The structural and the spectroscopic properties of LHCII were introduced first, especially the energy transfer characteristics including an intra-complex energy transfer part and an inter-complex energy transfer part. Different surface immobilization strategies of LHCII were summarized next. Among them the strategy based on the His-tag and the "immobilized metal affinity chromatography" (IMAC) technique were of great interest and evolved into four kinds of home-fabricated His-tag chelating chips. After optimization, His-tag chelating chip B and D were the most promising candidates for His-tagged LHCII immobilization in this study because of their high protein coupling capacity, maintenance of good biological activity and a remarkably repeatable protein binding ability on the same chip after regeneration. Moreover, different parameters related to the stability of surface coupled reconstituted complex, including sucrose, detergent, lipid, oligomerization, temperature and circulation rate, were evaluated in order to standardize the most effective immobilization conditions. In addition, partial lipid bilayers obtained from LHCII contained proteo-liposomes fusion on the surface were observed by the QCM technique. Finally, the inter-complex energy transfer between neighboring LHCIIs was recorded for the first time, and the factors influencing the energy transfer efficiency were discussed.

7 SUMMARY

Despite different objects in this study, the essence of the research can be summarized as a systematic study for functional protein immobilization by surface plasmon field-enhanced fluorescence spectroscopy. As mentioned, both tools and targets are the focus of our interest. The whole work can be divided into two main parts: the modification of our traditional SPFS instrument with some optical spectrometer components, enabling the new version of the instrument to use a blue laser as the excitation light source for some specific fluorescence studies and the investigation of the surface immobilization approaches for proteins and other biomolecules.

A DPSS blue laser corresponding to the chlorophyll *b* adsorption was exploited to prove the biological activity of surface bound LHCII complexes via their surface-enhanced full fluorescence spectra. The gold protected silver film maintains some of the electromagnetic field enhancement while avoiding oxidation. The field enhancement could be further increased by use of pure silver, whose stability can be improved by the assembly of other kinds of dielectric layer, *e.g.* the functionalized cellulose[171,172], which gives the possibility of investigating the ubiquitous green fluorescence protein (GFP) and its derivatives by the SPFS technology in the future.

The first step in the interaction analysis is the immobilization of one of the partners on the sensor chip surface without a major loss of activity of the attached biological molecules. The remarkable intrinsic features of S-layer proteins and the possibility for combining S-layer lattices with other functional molecules in a spatial predictable way make them a promising element in molecular nanotechnology and biomimetics. The recrystallization behavior of S-laye proteins on gold or on the secondary cell wall polymer (SCWP) was recorded by SPR. The optical thicknesses and surface densities for different protein layers were calculated. In DNA hybridization tests performed in order to discriminate different mismatches, recombinant S-layer-streptavidin fusion protein matrices showed their potential for new microarrays. Moreover, SCWPs coated gold chips, covered with a controlled and oriented assembly of S-layer fusion proteins, represent an even more sensitive fluorescence testing platform. Additionally, S-layer fusion proteins as the matrix for LHCII immobilization strongly demonstrate superiority over routine approaches, proving the possibility of utilizing them as a new strategy for biomolecular coupling.

The universal binding matrix streptavidin assembled at the solid/solution interface provides the specific sites for the attachment of any desired ligand system and guarantees a minimum separation distance between the chromophore labels and the metal quencher, as proved by a SPFS-based hCG immunoassay. In this study, the effect of the biotin thiol dilution on the coupling efficiently was investigated first. Next, the affinity characteristics between different antibodies and hCG were measured via an equilibrium binding analysis, which is the first example for the titration of such a high affinity interaction by SPFS. The results agree very well with the constants derived from the literature. Finally, a sandwich assay and a competitive assay were selected as templates for SPFS-based hCG detection, and an excellent LOD of 0.15 mIU/ml was attained via the “one step” sandwich method. Such high sensitivity not only fulfills clinical requirements, but is also better than most other biosensors.

Fully understanding how LHCII complexes transfer the sunlight energy directionally and efficiently to the reaction center is potentially useful for constructing biomimetic devices as solar cells. Different surface immobilization strategies of LHCII were summarized. Among them the strategy based on the His-tag and the immobilized metal (ion) affinity chromatography (IMAC) technique were of great interest and resulted in different kinds of home-fabricated His-tag chelating chips. Their substantial protein coupling capacity, maintenance of high biological activity and a remarkably repeatable binding ability on the same chip after regeneration was demonstrated. In addition, partial lipid bilayers obtained from LHCII contained proteo-liposomes fusion on the surface were observed by the QCM technique. Finally, the inter-complex energy transfer between neighboring LHCIIs on a gold protected silver surface by excitation with a blue laser ($\lambda = 473$nm) was recorded for the first time, and the factors influencing the energy transfer efficiency were evaluated.

8 SUPPLEMENT

8.1 List of Figures

8.2 List of Tables

8.3 Bibliography

Reference List

1. Collings, A. F. & Caruso, F. Biosensors: recent advances. *Reports on Progress in Physics* **60**, 1397-1445 (1997).

2. McFadden, P. BIOSENSORS: Broadband Biodetection: Holmes on a Chip. *Science* **297**, 2075-2076 (2002).

3. Pearson, J. E., Gill, A. & Vadgama, P. Analytical aspects of biosensors. *Annals of Clinical Biochemistry* **37**, 119-145 (2000).

4. Clark, L. C. & Lyons, C. Electrode Systems for Continuous Monitoring in Cardiovascular Surgery. *Annals of the New York Academy of Sciences* **102**, 29-& (1962).

5. Lander, E. S. *et al.* Initial sequencing and analysis of the human genome. *Nature* **409**, 860-921 (2001).

6. Venter, J. C. *et al.* The sequence of the human genome. *Science* **291**, 1304-+ (2001).

7. Neet, K. E. & Lee, J. C. Biophysical Characterization of Proteins in the Post-genomic Era of Proteomics. *Mol Cell Proteomics* **1**, 415-420 (2002).

8. Ramsden, J. J. Optical biosensors. *Journal of Molecular Recognition* **10**, 109-120 (1997).

9. Jonsson, U. *et al.* Real-Time Biospecific Interaction Analysis Using Surface-Plasmon Resonance and A Sensor Chip Technology. *Biotechniques* **11**, 620-& (1991).

10. Day, Y. S. N., Baird, C. L., Rich, R. L. & Myszka, D. G. Direct comparison of binding equilibrium, thermodynamic, and rate constants determined by surface- and solution-based biophysical methods. *Protein Science* **11**, 1017-1025 (2002).

11. Liebermann, T. & Knoll, W. Surface-plasmon field-enhanced fluorescence spectroscopy. *Colloids and Surfaces A-Physicochemical and Engineering Aspects* **171**, 115-130 (2000).

12. Neumann, T., Johansson, M. L., Kambhampati, D. & Knoll, W. Surface-plasmon fluorescence spectroscopy. *Advanced Functional Materials* **12**, 575-586 (2002).

13. Sleytr, U. B., Schuster, B. & Pum, D. Nanotechnology and biomimetics with 2-D protein crystals. *Ieee Engineering in Medicine and Biology Magazine* **22**, 140-150 (2003).

14. Sleytr, U. B., Sara, M., Pum, D. & Schuster, B. Characterization and use of crystalline bacterial cell surface layers. *Progress in Surface Science* **68**, 231-278 (2001).

15. Luppa, P. B., Sokoll, L. J. & Chan, D. W. Immunosensors--principles and applications to clinical chemistry. *Clinica Chimica Acta* **314**, 1-26 (2001).

16. Buchanan, B., Gruissem, W. & Jones, R. L. *Biochemistry & Molecular Biology of Plants*. John Wiley & Sons, (2002).

17. Paulsen, H. Chlorophyll A/B-Binding Proteins. *Photochemistry and Photobiology* **62**, 367-382 (1995).

18. Wood, R. W. On a Remarkable Case of Uneven Distribution of Light in a Diffraction Grating Spectrum. *Proceedings of the Physical Society of London* 269-275 (1902).

19. Otto, A. Excitation of Nonradiative Surface Plasma Waves in Silver by Method of Frustrated Total Reflection. *Zeitschrift fur Physik* **216**, 398-& (1968).

20. Kretschmann.E & Raether, H. Radiative Decay of Non Radiative Surface Plasmons Excited by Light. *Zeitschrift fur Naturforschung Part A-Astrophysik Physik und Physikalische Chemie* **A 23**, 2135-& (1968).

21. Agarwal, G. S. New Method in Theory of Surface Polaritons. *Physical Review B* **8**, 4768-4779 (1973).

22. Swalen, J. D. Optical properties of Langmuir-Blodgett films. *Journal of Molecular Electronics* **2**, 155-181 (1986).

23. Saleh, B. E. A. & Teich, M. C. *Fundamentals of Photonics*. Wiley-Interscience, (1991).

24. Knoll, W. Interfaces and thin films as seen by bound electromagnetic waves. *Annual Review of Physical Chemistry* **49**, 569-638 (1998).

25. Hickel, W., Rothenhausler, B. & Knoll, W. Surface-Plasmon Microscopic Characterization of External Surfaces. *Journal of Applied Physics* **66**, 4832-4836 (1989).

26. Yu, F. Surface Plasmon Fluorescence Spectroscopy and Surface Plasmon Diffraction in Biomolecular Interaction Studies. 2004. Max-Planck-Institut f 黯 Polymerforschung.
    Ref Type: Thesis/Dissertation
27. Rendell, D. F*luorescence and Phosphorescence.* John Wiley & Sons Inc, (1987).

28. http://www.probes.com/handbook/boxes/0422.html. 2005.
    Ref Type: Internet Communication

29. Selvin, P. R. The renaissance of fluorescence resonance energy transfer. N*ature Structural Biology* 7**,** 730-734 (2000).

30. Ha, T. Single-molecule fluorescence resonance energy transfer. M*ethods* 2**5,** 78-86 (2001).

31. Perez-Luna, V. H. *et al.* Molecular recognition between genetically engineered streptavidin and surface-bound biotin. J*ournal of the American Chemical Society* 1**21,** 6469-6478 (1999).

32. Jung, L. S. *et al.* Surface plasmon resonance measurement of binding and dissociation of wild-type and mutant streptavidin on mixed biotin-containing alkylthiolate monolayers. S*ensors and Actuators B-Chemical* 5**4,** 137-144 (1999).

33. Spinke, J., Liley, M., Guder, H. J., Angermaier, L. & Knoll, W. Molecular Recognition at Self-Assembled Monolayers - the Construction of Multicomponent Multilayers. L*angmuir* 9**,** 1821-1825 (1993).

34. Raether, H. S*urface Plasmons on Smooth and Rough Surfaces and on Gratings.* Springer-Verlag, (1988).

35. Nemetz, A. & Knoll, W. Raman spectroscopy and microscopy with plasmon surface polaritons. J*ournal of Raman Spectroscopy* 2**7,** 587-592 (1996).

36. Axelrod, D., Burghardt, T. P. & Thompson, N. L. Total Internal-Reflection Fluorescence. A*nnual Review of Biophysics and Bioengineering* 1**3,** 247-268 (1984).

37. Winzor, D. J. & Sawyer, W. H. Q*uantitative Characterisation of Ligand Binding.* Wiley-Liss, (1995).

38. Atkins, P. W. P*hysical Chemistry.* Oxford University Press, (1998).

39. Homola, J., Yee, S. S. & Gauglitz, G. Surface plasmon resonance sensors: review. S*ensors and Actuators B-Chemical* 5**4,** 3-15 (1999).

40. Ward, L. D. & Winzor, D. J. Relative merits of optical biosensors based on flow-cell and cuvette designs. A*nalytical Biochemistry* 2**85,** 179-193 (2000).

41. Palik, E. D. H*andbook of Optical Constants of Solids.* Academic Press, (1985).

42. Ulman, A. A*n Introduction to Ultrathin Organic Films : From Langmuir-Blodgett to Self-Assembly.* Academic Press, (1991).

43. Bain, C. D. *et al.* Formation of Monolayer Films by the Spontaneous Assembly of Organic Thiols from Solution Onto Gold. J*ournal of the American Chemical Society* 1**11,** 321-335 (1989).

44. Nuzzo, R. G., Dubois, L. H. & Allara, D. L. Fundamental-Studies of Microscopic Wetting on Organic-Surfaces .1. Formation and Structural Characterization of A Self-Consistent Series of Polyfunctional Organic Monolayers. J*ournal of the American Chemical Society* 1**12,** 558-569 (1990).

45. Stewart, K. R., Whitesides, G. M., Godfried, H. P. & Silvera, I. F. Improved Adhesion of Thin Conformal Organic Films to Metal-Surfaces. R*eview of Scientific Instruments* 5**7,** 1381-1383 (1986).

46. Troughton, E. B. *et al.* Monolayer Films Prepared by the Spontaneous Self-Assembly of Symmetrical and Unsymmetrical Dialkyl Sulfides from Solution Onto Gold Substrates - Structure, Properties, and Reactivity of Constituent Functional-Groups. L*angmuir* **4,** 365-385 (1988).

47. Knoll, W. *et al.* Streptavidin arrays as supramolecular architectures in surface-plasmon optical sensor formats. C*olloids and Surfaces A-Physicochemical and Engineering Aspects* 1**61,** 115-137 (2000).

48. Sigal, G. B., Bamdad, C., Barberis, A., Strominger, J. & Whitesides, G. M. A self-assembled monolayer for the binding and study of histidine tagged proteins by surface plasmon resonance. A*nalytical Chemistry* 6**8,** 490-497 (1996).

49. Spinke, J. *et al.* Molecular Recognition at Self-Assembled Monolayers - Optimization of Surface Functionalization. J*ournal of Chemical Physics* 9**9,** 7012-7019 (1993).

50. Kambhampati, D. K. *et al.* Novel silicon dioxide sol-gel films for potential sensor applications: A surface plasmon resonance study. L*angmuir* 1**7,** 1169-1175 (2001).

51. Ellman, G. L. Tissue sulfhydryl groups. A*rchives of Biochemistry and Biophysics* 8**2,** 70-77 (1959).

52. Rogl, H., Kosemund, K., Kuhlbrandt, W. & Collinson, I. Refolding of Escherichia coli produced membrane protein inclusion bodies immobilised by nickel chelating chromatography. F*EBS Letters* 4**32,** 21-26 (1998).

53. Paulsen, H., Rumler, U. & Rudiger, W. Reconstitution of Pigment-Containing Complexes from Light-Harvesting Chlorophyll-A/B-Binding Protein Overexpressed in Escherichia-Coli. P*lanta* 1**81,** 204-211 (1990).

54. Plumley, F. G. & Schmidt, G. W. Reconstitution of Chlorophyll A/B Light-Harvesting Complexes - Xanthophyll-Dependent Assembly and Energy-Transfer. P*roceedings of the National Academy of Sciences of the United States of America* 8**4,** 146-150 (1987).

55. Paulsen, H., Finkenzeller, B. & Kuhlein, N. Pigments Induce Folding of Light-Harvesting Chlorophyll Alpha/Beta-Binding Protein. E*uropean Journal of Biochemistry* 2**15,** 809-816 (1993).

56. Butler, P. J. G. & Kuhlbrandt, W. Determination of the Aggregate Size in Detergent Solution of the Light-Harvesting Chlorophyll a/b-Protein Complex from Chloroplast Membranes. P*NAS* 8**5,** 3797-3801 (1988).

57. Moll, D. *et al.* S-layer-streptavidin fusion proteins as template for nanopatterned molecular arrays. P*roceedings of the National Academy of Sciences of the United States of America* 9**9,** 14646-14651 (2002).

58. Jarosch, M., Egelseer, E. M., Mattanovich, D., Sleytr, U. B. & Sara, M. S-layer gene sbsC of Bacillus stearothermophilus ATCC 12980: molecular characterization and heterologous expression in Escherichia coli. M*icrobiology-Sgm* 1**46,** 273-281 (2000).

59. Sleytr, U. B., Messner, P., Pum, D. & Sara, M. Crystalline bacterial cell surface layers (S layers): From supramolecular cell structure to biomimetics and nanotechnology. A*ngewandte Chemie-International Edition* 3**8,** 1035-1054 (1999).

60. Vollenkle, C. *et al.* Construction of a functional S-layer fusion protein comprising an immunoglobulin G-binding domain for development of specific adsorbents for extracorporeal blood purification. A*pplied and Environmental Microbiology* 7**0,** 1514-1521 (2004).

61. Pleschberger, M. *et al.* An S-layer heavy chain camel antibody fusion protein for generation of a nanopatterned sensing layer to detect the prostate-specific antigen by surface plasmon resonance technology. B*ioconjugate Chemistry* 1**5,** 664-671 (2004).

62. Ilk, N. *et al.* A functional chimaeric S-layer-enhanced green fluorescent protein to follow the uptake of S-layer-coated liposomes into eukaryotic cells. B*iochemical Journal* 3**79,** 441-448 (2004).

63. Ilk, N. *et al.* Molecular characterization of the S-layer gene, sbpA, of Bacillus sphaericus CCM 2177 and production of a functional S-layer fusion protein with the ability to recrystallize in a defined orientation while presenting the fused allergen. A*pplied and Environmental Microbiology* 6**8,** 3251-3260 (2002).

64. Pum, D., Neubauer, A., Gyorvary, E., Sara, M. & Sleytr, U. B. S-layer proteins as basic building blocks in a biomolecular construction kit. N*anotechnology* 1**1,** 100-107 (2000).

65. Sara, M., Dekitsch, C., Mayer, H. F., Egelseer, E. M. & Sleytr, U. B. Influence of the secondary cell wall polymer on the reassembly, recrystallization, and stability properties of the S-layer protein from Bacillus stearothermophilus PV72/p2. J*ournal of Bacteriology* 1**80,** 4146-4153 (1998).

66. Mesnage, S. *et al.* Bacterial SLH domain proteins are non-covalently anchored to the cell surface via a conserved mechanism involving wall polysaccharide pyruvylation. E*mbo Journal* 1**9,** 4473-4484 (2000).

67. Huber, C. *et al.* S-layer-streptavidin fusion proteins based on rSbpA, the S-layer protein of Bacillus sphaericus CCM 2177, as a universal template for biochip development. i*n preparation* (2005).

68. Sleytr, U. B., Gyorvary, E. & Pum, D. Crystallization of S-layer protein lattices on surfaces and interfaces. P*rogress in Organic Coatings* 4**7,** 279-287 (2003).

69. Pum, D. & Sleytr, U. B. The application of bacterial S-layers in molecular nanotechnology. T*rends in Biotechnology* 1**7,** 8-12 (1999).

70. Sleytr, U. B. & Beveridge, T. J. Bacterial S-layers. T*rends in Microbiology* 7**,** 253-260 (1999).

71. Frisbie, C. D., Rozsnyai, L. F., Noy, A., Wrighton, M. S. & Lieber, C. M. Functional-Group Imaging by Chemical Force Microscopy. S*cience* 2**65,** 2071-2074 (1994).

72. Stranick, S. J. *et al.* Nanometer-scale phase separation in mixed composition self-assembled monolayers. N*anotechnology* 7**,** 438-442 (1996).

73. Kambhampati, D., Nielsen, P. E. & Knoll, W. Investigating the kinetics of DNA-DNA and PNA-DNA interactions using surface plasmon resonance-enhanced fluorescence spectroscopy. B*iosensors & Bioelectronics* 1**6,** 1109-1118 (2001).

74. Lewin, B. G*enes VI.* Oxford Univ Pr (Sd), (1997).

75. Chauvaux, S., Matuschek, M. & Beguin, P. Distinct affinity of binding sites for S-layer homologous domains in Clostridium thermocellum and Bacillus anthracis cell envelopes. J*ournal of Bacteriology* 1**81,** 2455-2458 (1999).

76. Egelseer, E., Schocher, I., Sara, M. & Sleytr, U. B. The S-Layer from Bacillus-Stearothermophilus Dsm-2358 Functions As An Adhesion Site for A High-Molecular-Weight Amylase. J*ournal of Bacteriology* 1**77,** 1444-1451 (1995).

77. Baumert, H. G. & Fasold, H. Cross-Linking Techniques. M*ethods in Enzymology* 1**72,** 584-609 (1989).

78. Yao, D. PCR Product Analysis by Surface Plasmon-Based Biosensors. 2004. Max-Planck-Institut f黵 Polymerforschung.
Ref Type: Thesis/Dissertation

79. Ding, D. Strategic Studies of DNA Hybridization with Chemically Modified PNA by Surface Plasmon Field-Enhanced Fluorescence Spectroscopy. 2004. Max-Planck-Institut f黵 Polymerforschung.
Ref Type: Thesis/Dissertation

80. MacNaught, A. D. & Wiolinson, A. IUP*AC Compendium of Chemical Terminology. B*lackwell Science, (1997).

81. Handrea, M., Sahre, M., Neubauer, A., Sleytr, U. B. & Kautek, W. Electrochemistry of nano-scale bacterial surface protein layers on gold. Bio*electrochemistry 61*, **1**-8 (2003).

82. Glaser, R. W. Antigen-Antibody Binding and Mass-Transport by Convection and Diffusion to A Surface - A 2-Dimensional Computer-Model of Binding and Dissociation Kinetics. Ana*lytical Biochemistry 21*3**,** **1**52-161 (1993).

83. Fotinou, C. et *al.* Structure of an Fab fragment against a C-terminal peptide of hCG at 2.0 angstrom resolution. *Journal of Biological Chemistry 273*, **22515-22518** (1998).

84. Berger, P. et *al.* The ISOBM TD-7 workshop on hCG and related molecules - Towards user-oriented standardization of pregnancy and tumor diagnosis: Assignment of epitopes to the three-dimensional structure of diagnostically and commercially relevant monoclonal antibodies directed against human chorionic gonadotropin and derivatives. *Tumor Biology 23*, **1-38** (2002).

85. www.idc-wick.com. 2005.
Ref Type: Internet Communication

86. Tegoni, M., Spinelli, S., Verhoeyen, M., Davis, P. & Cambillau, C. Crystal structure of a ternary complex between human chorionic gonadotropin (hCG) and two Fv fragments specific for the alpha and beta-subunits. *Journal of Molecular Biology 289*, **1375-1385** (1999).

87. www.rapidtest.com. 2005.
Ref Type: Internet Communication

88. Hage, D. S. Immunoassays. *Analytical Chemistry 71*, **294R-304R** (1999).

89. Yu, F., Persson, B., Lofas, S. & Knoll, W. Attomolar sensitivity in bioassays based on surface plasmon fluorescence spectroscopy. *Journal of the American Chemical Society 126*, **8902-8903** (2004).

90. Wilchek, M. & Bayer, E. A. Foreward and introduction to the book (strept)avidin-biotin system. *Biomolecular Engineering 16*, **1-4** (1999).

91. Amit, A. G., Mariuzza, R. A., Phillips, S. E. V. & Poljak, R. J. 3-Dimensional Structure of An Antigen-Antibody Complex at 2.8-A Resolution. *Science 233*, **747-753** (1986).

92. Grabbe, E. S. Total Internal-Reflection Fluorescence with Energy-Transfer - A Method for Analyzing Igg Adsorption on Nylon Thin-Films. *Langmuir 9,* **1574-1581** (1993).

93. Andersson, K., Areskoug, D. & Hardenborg, E. Exploring buffer space for molecular interactions. *Journal of Molecular Recognition 12*, **310-315** (1999).

94. www.biacore.com. 2005.
Ref Type: Internet Communication

95. Schuck, P. & Minton, A. P. Analysis of mass transport-limited binding kinetics in evanescent wave biosensors. *Analytical Biochemistry 240*, **262-272** (1996).

96. Engvall, E. & Perlmann, P. Enzyme-Linked Immunosorbent Assay (Elisa) Quantitative Assay of Immunoglobulin-G. *Immunochemistry 8,* **871-&** (1971).

97. Gosling, J. P. A Decade of Development in Immunoassay Methodology. *Clinical Chemistry 36*, **1408-1427** (1990).

98. Chetcuti, A. F., Wong, D. K. Y. & Stuart, M. C. An indirect perfluorosulfonated ionomer-coated electrochemical immunosensor for the detection of the protein human chorionic gonadotrophin. *Analytical Chemistry 71*, **4088-4094** (1999).

99. Lim, T. K. & Matsunaga, T. Construction of electrochemical flow immunoassay system using capillary columns and ferrocene conjugated immunoglobulin G for detection of human chorionic gonadotrophin. *Biosensors & Bioelectronics 16*, **1063-1069** (2001).

100. Schult, K. et *al. Di*sposable optical sensor chip for medical diagnostics: New ways in bioanalysis. Ana*lytical Chemistry 71*, **5**430-5435 (1999).

101. Schneider, B. H., Dickinson, E. L., Vach, M. D., Hoijer, J. V. & Howard, L. V. Highly sensitive optical chip immunoassays in human serum. Bio*sensors & Bioelectronics 15*, **1**3-22 (2000).

102. Schneider, B. H., Dickinson, E. L., Vach, M. D., Hoijer, J. V. & Howard, L. V. Optical chip immunoassay for hCG in human whole blood. Bio*sensors & Bioelectronics 15*, **5**97-604 (2000).

103. Boozer, C. et *al. Su*rface functionalization for self-referencing surface plasmon resonance (SPR) biosensors by multi-step self-assembly. Sen*sors and Actuators B-Chemical 90*, **2**2-30 (2003).

104. Dostalek, J. et *al. Su*rface plasmon resonance biosensor based on integrated optical waveguide. Sen*sors and Actuators B-Chemical 76*, **8-**12 (2001).

105. Hankamer, B., Barber, J. & Boekema, E. J. Structure and membrane organization of photosystem II in green plants. Ann*ual Review of Plant Physiology and Plant Molecular Biology 48*, **6**41-671 (1997).

106. Kuhlbrandt, W. Structure and Function of the Plant Light-Harvesting Complex, Lhc-Ii. Cur*rent Opinion in Structural Biology 4,* **5**19-528 (1994).

107. Thornber, J. P. et *al. An*tenna pigment-protein complexes of higher plants and purple bacteria. Adv*ances in Molecular and Cell Biology 10*, **5**5-118 (1994).

108. van Amerongen, H. & van Grondelle, R. Understanding the energy transfer function of LHCII, the major light-harvesting complex of green plants. Jou*rnal of Physical Chemistry B 10*5**, 6**04-617 (2001).

109. Boekema, E. J., van Roon, H., van Breemen, J. F. L. & Dekker, J. P. Supramolecular organization of photosystem II and its light-harvesting antenna in partially solubilized photosystem II membranes. Eur*opean Journal of Biochemistry 26*6**, 4**44-452 (1999).

110. Kuhlbrandt, W., Wang, D. N. & Fujiyoshi, Y. Atomic Model of Plant Light-Harvesting Complex by Electron Crystallography. Nat*ure 36*7**, 6**14-621 (1994).

111. Liu, Z. F. et *al. Cr*ystal structure of spinach major light-harvesting complex at 2.72 angstrom resolution. Nat*ure 42*8**, 2**87-292 (2004).

112. Alberts, B. et *al. Molecular Biology of the Cell. G*arland Science, (2002).

113. Hobe, S., Prytulla, S., Kuhlbrandt, W. & Paulsen, H. Trimerization and Crystallization of Reconstituted Light-Harvesting Chlorophyll A/B Complex. Emb*o Journal 13*, **3**423-3429 (1994).

114. Booth, P. J. & Paulsen, H. Assembly of light-harvesting chlorophyll a/b complex in vitro. Time-resolved fluorescence measurements. Bio*chemistry 35*, **5**103-5108 (1996).

115. Lee, J. W., Lee, I. & Greenbaum, E. Platinization: A novel technique to anchor photosystem I reaction centres onto a metal surface at biological temperature and pH. Bio*sensors & Bioelectronics 11*, **3**75-387 (1996).

116. Lee, I., Lee, J. W., Stubna, A. & Greenbaum, E. Measurement of electrostatic potentials above oriented single photosynthetic reaction centers. Jou*rnal of Physical Chemistry B 10*4**, 2**439-2443 (2000).

117. Lee, I., Lee, J. W. & Greenbaum, E. Biomolecular electronics: Vectorial arrays of photosynthetic reaction centers. Phy*sical Review Letters 79*, **3**294-3297 (1997).

118. Nakamura, C., Hasegawa, M., Nakamura, N. & Miyake, J. Rapid and specific detection of herbicides using a self-assembled photosynthetic reaction center from purple bacterium on an SPR chip. Bio*sensors & Bioelectronics 18*, **5**99-603 (2003).

119. Tietz, C. et *al. Si*ngle molecule spectroscopy on the light-harvesting complex II of higher plants. Bio*physical Journal 81*, **5**56-562 (2001).

120. Cashmore, A. R. Structure and Expression of A Pea Nuclear Gene Encoding A Chlorophyll A B-Binding Polypeptide. Pro*ceedings of the National Academy of Sciences of the United States of America-Biological Sciences 81*, **2**960-2964 (1984).

121. Iriyama, K. & Shiraki, M. Improved Method for Extraction, Partial-Purification, Separation and Isolation of Chlorophyll from Spinach Leaves. Jou*rnal of Liquid Chromatography 2,* **2**55-276 (1979).

122. Oshannessy, D. J., Odonnell, K. C., Martin, J. & Brighamburke, M. Detection and Quantitation of Hexa-Histidine-Tagged Recombinant Proteins on Western Blots and by A Surface-Plasmon Resonance Biosensor Technique. Ana*lytical Biochemistry 22*9**, 1**19-124 (1995).

123. Kirchhoff, H., Hinz, H. R. & Rosgen, J. Aggregation and fluorescence quenching of chlorophyll a of the light-harvesting complex II from spinach in vitro. Bio*chimica et Biophysica Acta-Bioenergetics 16*0**6, 1**05-116 (2003).

124. Essen, L. O. & Skerra, A. Single-step purification of a bacterially expressed antibody Fv fragment by immobilized metal affinity chromatography in the presence of betaine. Jou*rnal of Chromatography A 65*7**, 5**5-61 (1993).

125. Noji, H., Yasuda, R., Yoshida, M. & Kinosita, K. Direct observation of the rotation of F-1-ATPase. Nat*ure 38*6**, 2**99-302 (1997).

126. Deobagkar, D. N., Shankar, V. & Deobagkar, D. D. Separation of 5-Methylcytosine-Rich Dna Using Immobilized Antibody. Enz*yme and Microbial Technology 8,* **9**7-100 (1986).

127. Schmidt, T. G. M. & Skerra, A. The Random Peptide Library-Assisted Engineering of A C-Terminal Affinity Peptide, Useful for the Detection and Purification of A Functional Ig Fv Fragment. Pro*tein Engineering 6,* **1**09-122 (1993).

128. Schmidt, T. G. M., Koepke, J., Frank, R. & Skerra, A. Molecular interaction between the Strep-tag affinity peptide and its cognate target, streptavidin. Jou*rnal of Molecular Biology 25*5**, 7**53-766 (1996).

129. www.iba-go.de. 2005.
Ref Type: Internet Communication

130. Skerra, A. & Schmidt, T. G. M. Applications of a peptide ligand for streptavidin: the Strep-tag. Bio*molecular Engineering 16*, **7**9-86 (1999).

131. Hengsakul, M. & Cass, A. E. G. Alkaline phosphatase-strep tag fusion protein binding to streptavidin: Resonant mirror studies. Jou*rnal of Molecular Biology 26*6**, 6**21-632 (1997).

132. Von Grunigen, R. & Schneider, C. H. Epitope analysis: biotinylated short peptides as inhibitors of anti-peptide antibody. Jou*rnal of Immunological Methods 12*5**, 1**43-146 (1989).

133. Peter, J. C., Briand, J. P. & Hoebeke, J. How biotinylation can interfere with recognition: a surface plasmon resonance study of peptide-antibody interactions. Jou*rnal of Immunological Methods 27*4**, 1**49-158 (2003).

134. IAs*ys Technical Resources. T*hermoLabsystems, (2005).

135. Porath, J., Carlsson, J., Olsson, I. & Belfrage, G. Metal Chelate Affinity Chromatography, A New Approach to Protein Fractionation. Nat*ure 25*8**, 5**98-599 (1975).

136. Hochuli, E., Dobeli, H. & Schacher, A. New Metal Chelate Adsorbent Selective for Proteins and Peptides Containing Neighboring Histidine-Residues. Jou*rnal of Chromatography 41*1**, 1**77-184 (1987).

137. Pearson, R. G. Hard and Soft Acids and Bases Hsab .1. Fundamental Principles. Jou*rnal of Chemical Education 45*, **5**81-& (1968).

138. Ueda, E. K. M., Gout, P. W. & Morganti, L. Current and prospective applications of metal ion-protein binding. Jou*rnal of Chromatography A 98*8**, 1**-23 (2003).

139. Arnold, F. H. Metal-Affinity Separations - A New Dimension in Protein Processing. Bio-*Technology 9,* **1**51-156 (1991).

140. Hainfeld, J. F., Liu, W. Q., Halsey, C. M. R., Freimuth, P. & Powell, R. D. Ni-NTA-gold clusters target his-tagged proteins. Jou*rnal of Structural Biology 12*7**, 1**85-198 (1999).

141. Schmitt, J., Hess, H. & Stunnenberg, H. G. Affinity Purification of Histidine-Tagged Proteins. Mol*ecular Biology Reports 18*, **2**23-230 (1993).

142. Hoffmann, A. & Roeder, R. G. Purification of His-Tagged Proteins in Nondenaturing Conditions Suggests A Convenient Method for Protein-Interaction Studies. Nuc*leic Acids Research 19*, **6**337-6338 (1991).

143. Kubalek, E. W., Le Grice, S. F. J. & Brown, P. O. Two-Dimensional Crystallization of Histidine-Tagged, HIV-1 Reverse Transcriptase Promoted by a Novel Nickel-Chelating Lipid. Jou*rnal of Structural Biology 11*3**, 1**17-123 (1994).

144. Paborsky, L. R., Dunn, K. E., Gibbs, C. S. & Dougherty, J. P. A nickel chelate microtiter plate assay for six histidine-containing proteins. Ana*lytical Biochemistry 23*4**, 6**0-65 (1996).

145. Jin, L. et *al. Us*e of Alpha-N,N-Bis[Carboxymethyl] Lysine-Modified Peroxidase in Immunoassays. Ana*lytical Biochemistry 22*9**, 5**4-60 (1995).

146. Gershon, P. D. & Khilko, S. Stable Chelating Linkage for Reversible Immobilization of Oligohistidine Tagged Proteins in the Biacore Surface-Plasmon Resonance Detector. Jou*rnal of Immunological Methods 18*3**, 6**5-76 (1995).

147. Madoz-Gurpide, J. et *al. Mo*dulation of electroenzymatic NADPH oxidation through oriented immobilization of ferredoxin : NADP(+) reductase onto modified gold electrodes. Jou*rnal of the American Chemical Society 12*2**, 9**808-9817 (2000).

148. Wegner, G. J., Lee, N. J., Marriott, G. & Corn, R. M. Fabrication of histidine-tagged fusion protein arrays for surface plasmon resonance imaging studies of protein-protein and protein-DNA interactions. Ana*lytical Chemistry 75*, **4**740-4746 (2003).

149. Radler, U., Mack, J., Persike, N., Jung, G. & Tampe, R. Design of supported membranes tethered via metal-affinity ligand-receptor pairs. Bio*physical Journal 79*, **3**144-3152 (2000).

150. Schmitt, L., Dietrich, C. & Tampe, R. Synthesis and Characterization of Chelator-Lipids for Reversible Immobilization of Engineered Proteins at Self-Assembled Lipid Interfaces. Jou*rnal of the American Chemical Society 11*6**, 8**485-8491 (1994).

151. Shnek, D. R., Pack, D. W., Sasaki, D. Y. & Arnold, F. H. Specific Protein Attachment to Artificial Membranes Via Coordination to Lipid-Bound Copper(Ii). Lan*gmuir 10*, **2**382-2388 (1994).

152. McMahan, S. A. & Burgess, R. R. Single-step synthesis and characterization of biotinylated nitrilotriacetic acid, a unique reagent for the detection of histidine-tagged proteins immobilized on nitrocellulose. Ana*lytical Biochemistry 23*6**, 1**01-106 (1996).

153. Ferguson, A. L. et *al. In*teraction of sigma(70) with Escherichia coli RNA polymerase core enzyme studied by surface plasmon resonance. FEB*S Letters 48*1**, 2**81-284 (2000).

154. Wang, R. L. C., Kreuzer, H. J. & Grunze, M. The interaction of oligo(ethylene oxide) with water: a quantum mechanical study. Phy*sical Chemistry Chemical Physics 2,* **3**613-3622 (2000).

155. Muller, K. M., Arndt, K. M., Bauer, K. & Pluckthun, A. Tandem immobilized metal-ion affinity chromatography/immunoaffinity purification of His-tagged proteins - Evaluation of two anti-His-tag monoclonal antibodies. Ana*lytical Biochemistry 25*9**, 5**4-61 (1998).

156. vis-Searles, P. R., Saunders, A. J., Erie, D. A., Winzor, D. J. & Pielak, G. J. Interpreting the effects of small uncharged solutes on protein-folding equilibria. Ann*ual Review of Biophysics and Biomolecular Structure 30*, **2**71-306 (2001).

157. Kim, Y. S. et *al. Ef*fects of sucrose on conformational equilibria and fluctuations within the native-state ensemble of proteins. Pro*tein Science 12*, **1**252-1261 (2003).

158. Yang, C. H., Kosemund, K., Cornet, C. & Paulsen, H. Exchange of pigment-binding amino acids in light-harvesting chlorophyll a/b protein. Bio*chemistry 38*, **1**6205-16213 (1999).

159. Wentworth, M., Ruban, A. V. & Horton, P. The functional significance of the monomeric and trimeric states of the photosystem II light harvesting complexes. Bio*chemistry 43*, **5**01-509 (2004).

160. Siegenthaler, P. A. & Murata, N. Lip*ids in Photosynthesis: Structure, Function and Genetics. K*luwer Academic Publishers, Dordrecht (1998).

161. Nussberger, S., Dorr, K., Wang, D. N. & Kuhlbrandt, W. Lipid-Protein Interactions in Crystals of Plant Light-Harvesting Complex. Jou*rnal of Molecular Biology 23*4**, 3**47-356 (1993).

162. Cui, X. Q. et *al. La*yer-by-layer assembly of multilayer films composed of avidin and biotin-labeled antibody for immunosensing. Bio*sensors & Bioelectronics 18*, **5**9-67 (2003).

163. Christensen, D. Assembly and Characterization of Protein Multi-layer Systems. 2004.
Ref Type: Thesis/Dissertation

164. Pugliese, L., Coda, A., Malcovati, M. & Bolognesi, M. 3-Dimensional Structure of the Tetragonal Crystal Form of Egg-White Avidin in Its Functional Complex with Biotin at 2.7-Angstrom Resolution. Jou*rnal of Molecular Biology 23*1**, 6**98-710 (1993).

165. Stamouli, A. et *al. Th*e ring structure and organization of light harvesting 2 complexes in a reconstituted lipid bilayer, resolved by atomic force microscopy. Bio*physical Journal 84*, **2**483-2491 (2003).

166. Berquand, A. et *al. Tw*o-step formation of streptavidin-supported lipid bilayers by PEG-triggered vesicle fusion. Fluorescence and atomic force microscopy characterization. Lang*muir 19*, **1**700-1707 (2003).

167. Keller, C. A. & Kasemo, B. Surface specific kinetics of lipid vesicle adsorption measured with a quartz crystal microbalance. Bio*physical Journal 75*, **1**397-1402 (1998).

168. Kleima, F. J. et *al. En*ergy transfer in LHCII monomers at 77K studied by sub-picosecond transient absorption spectroscopy. Bio*chemistry 36*, **1**5262-15268 (1997).

169. Wolf-Klein, H., Kohl, C., Mullen, K. & Paulsen, H. Biomimetic model of a plant photosystem consisting of a recombinant light-harvesting complex and a terrylene dye. Ang*ewandte Chemie-International Edition 41*, **3**378-+ (2002).

170. Wolf-Klein, H. Biomimetisches Modell eines Photosystems aus dem pflanzlichen Photosyntheseapparat: Energietransfermessungen und Einzelmolek黮 spektroskopie an Fluoreszenzfarbstoff-markiertem rekombinantem Lichtsammlerkomplex. 2001. Fachbereich Biologie der Johannes Gutenber-Universit鋞 in Mainz.
Ref Type: Thesis/Dissertation

171. Choi, S., Lauer, H., Wenz, G., Bruns, M. & Petri, D. F. S. Formation of dense cellulose monolayers on silver surfaces. Journ*al of the Brazilian Chemical Society 11,* 1**1-**15 (2000).

172. Petri, D. F. S. et a*l. Synt*hesis of a cellulose thiosulfate and its immobilization on gold surfaces. Polym*er 40,* 1**59**3-1601 (1999).